2-D and 3-D Viscoelastic Finite Element Models for Subduction Earthquake Deformation

Yan Hu

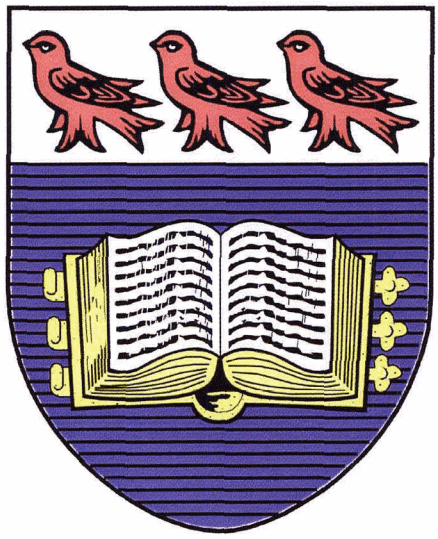

MSc Thesis

School of Earth and Ocean Sciences

University of Victoria

2004

2-D and 3-D Viscoelastic Finite Element Models for Subduction Earthquake Deformation

by

Yan Hu
B.A., Peking University, China, 1999

A Thesis Submitted in Partial Fulfillment of the
Requirements for the Degree of

MASTER OF SCIENCE

in the School of Earth and Ocean Sciences

Supervisor: Dr. Kelin Wang

ABSTRACT

GPS observations at the Chile and Alaska subduction zones decades after great subduction zone earthquakes have revealed that although coastal sites are moving landward as expected near a locked subduction fault, but some inland sites are moving in the opposite direction. The seaward motion of inland sites is interpreted to be a delayed response to the previous earthquake due to stress relaxation in the upper mantle. 2-D and 3-D linearly Maxwell viscoelastic finite element models are developed to study postseismic and interseismic crustal deformation associated with great subduction zone earthquakes. The application to the 1960 Chile Mw 9.5 earthquake at the Chile subduction zone helps to constrain the upper mantle viscosity to be about 3×10^{19} Pa s. The model results also help us understand the time dependent deformation and the hazard implications of the interseismic crustal deformation in other subduction zones.

Table of contents

Page

List of tables

Page

List of figures

Page

Acknowledgements

I would like to thank all the people making this thesis possible. I appreciate their help and support. I wish to thank the Pacific Geoscience Centre, Geological Survey of Canada, for providing work space, equipments and access to the facilities, and to PGC employees for sharing their knowledge. My special thanks are addressed to:

Kelin Wang, for being a great supervisor. He gave me tremendous help in my adjustment to English culture from Chinese culture. His guidance, inspiration and encouragements, and his patience in reviewing drafts were the major contribution to the realization of this work.

Jiangheng He, for writing the viscoelastic finite element source code and having discussions in programming.

George Spence, Roy Hyndman, and Stan Dosso, for their times, guidance and support as my UVic committee members.

Gia Khazaradze and Jürgen Klotz, the GeoForschungsZentrum (GFZ) Potsdam, Germany, for providing GPS data from the Chile subduction zone.

Stephane Mazzotti, for his time as my external examiner.

Yongen Cai, Peking University, China, and Brian Atwater, USGS, USA, for their helpful discussions.

My family, for all their encouragements and support in the pursuit of my dreams.

Finally, I would like to thank Dave Grewal, my roommate and good friend, for his cheerful spirit and unselfishness. This thesis is dedicated to Dave Grewal who did not live to finish his own nearly completed master degree because of a tragic traffic accident.

Chapter 1. Introduction

1.1. Opening Remarks

Great earthquakes that occur on subduction faults threaten many populated coastal areas along active continental margins. They cause damage not only through ground shaking but also by triggering tsunami waves. Understanding the strain accumulation and release processes of these earthquakes is important for hazard assessment and mitigation. Studying these deformation processes is also important for understanding plate boundary dynamics.

One primary method used to monitor the deformation process is geodetic observations. Over the past decade, the Global Positioning System (GPS) has been widely employed for this purpose with great success. Other methods, such as levelling surveys, tide gauge analyses, strain meter measurements, precise and/or absolute gravity measurements are also frequently used. The interpretation of all such data requires deformation modelling.

The most widely used deformation model is the elastic dislocation model (Savage, 1983). As a first-order model, it assumes that the subduction system is purely elastic, and therefore the deformation of the crust instantaneously responds to the motion of the fault. However, the real Earth approximates Maxwell viscoelastic behaviour; that is, any imposed stress will relax with time. In response to a subduction earthquake, the crust will first deform as an elastic body, but deformation will continue because of the stress relaxation. For this reason, the strain accumulation and release process throughout subduction earthquake cycles is complex time dependent behaviour.

Over the past three decades, the viscoelastic response of the upper mantle to large earthquakes has been studied by a number of people (Table 1.1). For example, Wahr and Wyss (1980) used a model of an elastic lithosphere overlying a viscoelastic volume to study the postseismic deformation of the Mw (moment magnitude) 9.1 1957 Adak and Unalaska earthquake and the Mw 8.7 1965 Attu earthquake. In their work, viscoelastic volumes with 80 km margin-normal width extending from 50 km to 200 m depth and 40 km width extending from 20 to 80 km depth were found to fit the postseismic tide gauge data after the 1957 and 1965 great earthquakes, respectively. Wahr and Wyss (1980) estimated the viscosity of the viscoelastic volumes to be $1.2 \sim 2.2 \times 10^{19}$ Pa s. The viscoelastic model has been applied to earthquakes in other tectonic settings. For example, a model of an upper elastic plate underlain by a viscoelastic asthenosphere was used to study the postseismic relaxation following the 1857 Southern California earthquake (Pollitz and Sacks, 1992). Pollitz and Sacks obtained a mantle viscosity of $0.4 \sim 0.8 \times 10^{19}$ Pa s by comparing the model results to triangulation measurements made in the late 1800s and mid-1920s on monuments within central and southern California. Ueda et al. (2003) used a three-layer model (a 40 km elastic first layer, a 50 km viscoelastic second layer and an elastic half-space) to study the postseismic crustal deformation following the 1993 Mw 7.8 Hokkaido Nanseioki earthquake. In their work, a viscosity of 4×10^{18} Pa s was obtained to fit GPS data, tide gauge records and levelling data in the western part of Hokkaido, the backarc region of the NE Japan subduction zone.

In this work, I employ viscoelastic finite element modelling to study crustal deformation associated with great subduction zone earthquakes. Geodetic data provide

Table 1.1. Viscosity of the upper mantle at subduction zones, inferred from postseismic deformation. Modified from James et al. (2000).

Subduction zone	Viscosity range (Pa s)	Reference
Aleutian and Alaska	$1.2 - 2.2 \times 10^{19}$	Wahr and Wyss (1980)
NE Japan	$\sim 10^{19}$	Thatcher et al. (1980)
NE Japan	$\sim 10^{19}$	Cohen (1984)
NE Japan	$\sim 10^{19}$	Suito and Hirahara (1999)
NE Japan	$7 \times 10^{18} - 1.3 \times 10^{19}$	Rydelek and Sacks (1990)
NE Japan	4×10^{18}	Ueda (2003)
Kanto (Japan)	10^{20}	Matsu'ura and Iwasaki (1983)
Nankai	$\sim 2 \times 10^{19}$	Miyashita (1987)
Nankai	$\sim 5 \times 10^{18}$	Thatcher and Rundle (1984)
Cascadia	$10^{18} - 10^{19}$	Wang et al. (1994)
Cascadia	10^{19}	Wang et al. (2001)
Chile	$8 \times 10^{19} - 10^{20}$	Piersanti (1999)
Chile	3×10^{19}	Khazaradze et al. (2002)

primary constraints for the mathematical models. In turn, model results help constrain the Earth rheology and help understand the transient nature of crustal deformation and its role in affecting earthquake hazard. Modelling results can also provide input for the design of future geodetic observations. The focus of this study is the great earthquakes that rupture very long segments of plate boundaries, such as the 1960 Chile earthquake of Mw 9.5, the 1964 Alaska earthquake of Mw 9.2, and the 1700 Cascadia earthquake of about magnitude 9. Those earthquakes are inferred to induce prolonged postseismic deformation.

1.2. Subduction Fault Seismogenic Behaviour

A typical active continental margin where an oceanic plate subducts beneath a continental plate is shown in Figure 1.1. Metamorphic reactions take place when the cold and fluid-abundant slab subducts into the mantle. Those reactions result in dehydration of the slab. The released fluids trigger partial melting of mantle-wedge rocks, and the ascending magma causes volcanism. Volcanoes usually form a chain (volcanic arc) parallel to the trench. The forearc refers to areas between the volcanic arc and the trench, and the back arc refers to areas landward of the volcanic arc.

Although not a focus of this thesis, an understanding of subduction fault seismogenic behaviour is necessary. In terms of seismogenic behaviour, the plate interface may be divided into three zones (e.g., Shimamoto et al., 1993; Hyndman and Wang, 1995): (1) a shallow updip zone that may be mechanically very weak, (2) a seismogenic zone that may rupture during an earthquake but may be locked between earthquakes, and (3) a lower downdip aseismic zone where the temperature is too high to allow seismic faulting. The updip and downdip limits of the seismogenic zone are proposed to be thermally controlled (Hyndman and Wang, 1993; Tichelaar and Ruff, 1993). Byrne et al. (1988) suggested that aseismic slip occurs in the unconsolidated and semi-consolidated sediments in the seaward updip zone. Hyndman and Wang (1993) and Hyndman et al. (1997) proposed that the updip temperature limit of the locked zone is about 100 – 150 $^{\circ}$C. The dehydration of stable sliding clay from smectite to illite in this temperature range was proposed to be responsible for the onset of seismogenic behaviour, but recent experiments do not support this hypothesis (Saffer et al., 2001). Explanations for the temperature limit are still being sought. Laboratory data for common crustal rocks and

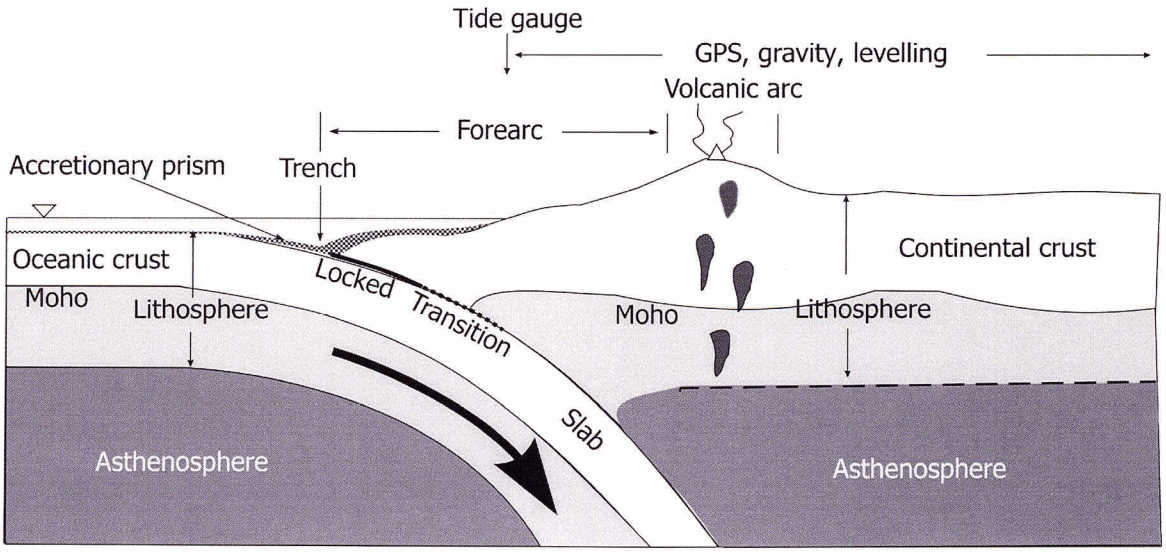

Figure 1.1. Schematic cross-section of an ocean-continent subduction zone.

field estimates for crustal earthquakes indicate that the downdip temperature limit of the locked zone is about 350°C (Chen and Molnar, 1983; Tse and Rice, 1986; Blanpied et al., 1991). This seems to be a critical temperature for the transition from velocity weakening (stick-slip) to velocity strengthening (stable sliding). Hyndman and Wang (1993) suggested that this temperature controls the downdip limit of the locked zone for warm subduction zones with young subducting plates. For cold subduction zones, this temperature is not reached until very large depths. Hyndman et al. (1997) proposed that the downdip limit in these cold subduction zones may be controlled by serpentinized forearc mantle wedge.

1.3. Time Scales of Crustal Deformation

Time scales of crustal deformation are shown in Table 1.2. For seismology, "coseismic" refers to a time scale of tens of seconds. Some subduction zone earthquakes generate tsunamis. For tsunami analysis, "coseismic" may refer to a time scale of several minutes. Earlier geodetic observations of subduction zone earthquakes may span months to a few years. In such cases, "coseismic" may refer to a time scale of a few years. In the present work, coseismic takes the geodetic meaning. "Postseismic" refers to a time scale of hours to tens of years after the earthquake, with "short-term" indicating hours to a few years. "Interseismic" refers to the time between two events, but it often excludes the short-term postseismic period. A subduction earthquake cycle is decades to centuries long. The redistribution of mass at the surface of the Earth due to the growth and melting of large ice sheets is at the time scale of $10^3 - 10^4$ years (James et al., 2000). The time scale of active faulting constrained by field geology is usually the order of 10^5 years or more

Table 1.2. Time scales (years).

Coseismic and postseismic	Short term postseismic	Interseismic	Post-glacial rebound	Geological	
				Neotectonic	Paleomagnetic
$0 - 10^1$	$\sim 10^1$	$\sim 10^2$	$10^3 - 10^4$	10^5	$> 10^6$

(neotectonic time scale). For comparison, plate or crustal block displacements constrained by paleomagnetic observations can be of the time scale of millions to hundreds of millions of years.

Different methods play different roles in observing crustal deformation associated with subduction zone earthquakes (Figure 1.2). Global Positioning System (GPS) developed by the U.S. Department of Defence is now widely used in precise surveying (e.g., Hofmann-Wellenhof et al., 1997). There are two types of GPS measurements: continuous recording and campaign style measurements. Continuous GPS data have good temporal coverage and resolution but usually poor spatial resolution except where the continuous GPS stations are very densely spaced such as in Japan. Campaign GPS data have poor temporal resolution, but a dense network can be organized to increase spatial resolution. GPS data can be used to study the crustal deformation in earthquake cycles and the static rupture and deformation process. In contrast, seismic methods can be used to study fault motion of several seconds to several minutes time scale and provide good information on the dynamic rupture process. Seafloor deformation of a time scale of several minutes due to a plate boundary earthquake may generate tsunami waves, and the recorded local and distant tsunami heights can be used to constrain the earthquake rupture process and faulting parameters (e.g., Satake et al., 2003). Tide gauges that measure sea

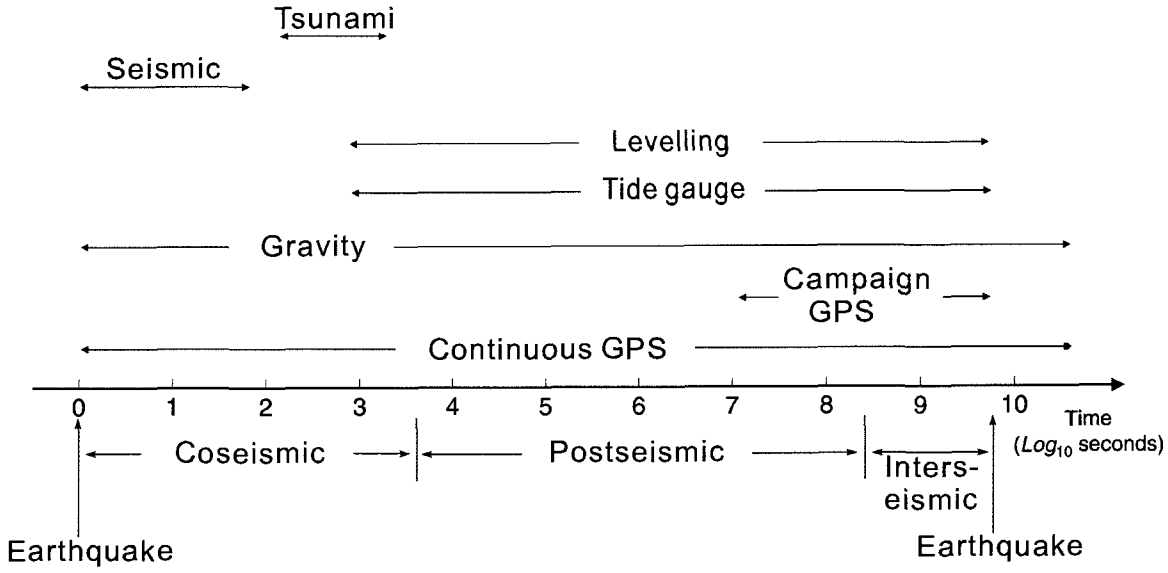

Figure 1.2. Observational methods used to constrain crustal deformation associated with subduction zone earthquakes.

level change reflect coastal uplift and subsidence relative to a global sea level reference, and levelling surveys provide measures of relative elevation changes or regional tilts. These two types of data provide good constraints on the vertical component of crustal deformation. Gravity changes due to changes in elevation can also help detect vertical crustal motion. These methods are complementary to GPS measurements which have good horizontal resolution but poorer vertical resolution. In the present work, however, we mainly consider the horizontal deformation field.

1.4. Structure of This Thesis

After this introduction, the second chapter describes the mathematical background of the numerical model, and the third chapter tests the effects of various model parameters using a simple two-dimensional (2-D) model. The fourth chapter focuses on the application of a three-dimensional (3-D) viscoelastic finite element model to the Chile subduction zone. Conclusions will be drawn in Chapter 5.

Chapter 2. Theoretical and Numerical Background

2.1. Mathematical Background

2.1.1. Rheology and Constitutive Relation

Rocks appear to be elastic and brittle, but folded sedimentary rocks and strongly deformed metamorphic rocks make it obvious that viscous deformation is also significant. Laboratory experiments and postglacial rebound analyses indicate that rocks deform both elastically and viscously depending on the time scale of the deformation and loading.

For a solid continuum, one end-member scenario of the rheology spectrum is pure elasticity. Instantaneous response of the Earth to loading or unloading is usually elastic. For example, a sudden slip along a fault (earthquake) causes elastic coseismic deformation surrounding the hypercentre. The relationship between elastic shear strain ε_{xy}^{E} and shear stress σ_{xy} in an elastic medium is given by:

$$\sigma_{xy} = 2\mu\varepsilon_{xy}^{E} \tag{2-1}$$

where μ is the shear modulus or rigidity, defined as

$$\mu = \frac{E}{2(1+\upsilon)} \tag{2-2}$$

where E is the Young's modulus, and υ is the Poisson's ratio.

The other end-member scenario of the rheology spectrum is purely viscous behaviour. On geological time scales, the deformation in the entire mantle must be viscous. On time scales of larger than 10^1 years, not all the mantle deforms elastically. Therefore,

postseismic and interseismic crustal deformation could be affected by viscous deformation in the underlying mantle. This effect is going to be studied in this thesis. In contrast to the elastic medium, stress in a viscous medium is a function of strain rate as well as other physical properties. Subject to a constant load, the deformation in a viscous medium changes with time (viscous flow). There are two types of viscous flow, Newtonian and Non-Newtonian. If we consider shear stress only, the Newtonian viscous flow obeys

$$\sigma_{xy} = 2\eta \dot{\varepsilon}_{xy}^{V} \tag{2-3}$$

where ε_{xy}^{V} is the viscous shear strain, η is the viscosity. A dot at the top denotes the time derivative (rate) of the variable. The Non-Newtonian viscous flow includes power-law flow and exponential-law flow (Melosh, 1980). A general form of the power law is

$$\dot{\varepsilon}_{xy} = A_1 \sigma_d^n \exp^{-\frac{Q}{RT}} \tag{2-4}$$

where A_1 is a constant, σ_d is the differential stress (difference between the maximum and minimum principle stresses), Q is the activation energy for creep, R is the universal gas constant, and T is absolute temperature. The power n is an experimentally determined parameter. The power n typically varies between 1 – 2 when $\sigma_d < 20$ MPa and between 2 – 4 when $20 < \sigma_d < 200$ MPa (http://jove.geol.niu.edu/faculty/fischer/PDFs/lect_7.pdf). If $n = 1$, equation (2-4) describes the Newtonian flow (2-3). An expression of the exponential flow law is

$$\dot{\varepsilon}_{xy} = A_2 e^{\beta \sigma_d} \sigma_d^n \exp^{-\frac{Q}{RT}} \tag{2-5}$$

where A_2 and β are constants. Other variables and parameters are the same as in (2-4). The exponential flow is generally considered unimportant for most Earth processes,

because it requires very large differential stresses. For various objectives, the power law may better describe the real viscous flow in the Earth, but the first-order pattern of the viscous flow in the upper mantle is very often well approximated by using the Newtonian viscous flow law.

In reality, the rheology of the Earth is complicated: The rocks can be purely elastic, or purely viscous, or viscoelastic, depending on in situ conditions. Rock properties in the Earth are heterogeneous. The lithosphere may be well described using an elastic rheology even on geological time scales, but the rheology of the underlying mantle is likely to be a case between the two end-member scenarios. In earthquake and post-glacial rebound analyses, material in the upper mantle is usually represented using a Maxwell viscoelastic body (Thatcher and Rundle, 1984; Wang et al., 1994; Piersanti, 1999; James et al., 2000). In this thesis, the Maxwell rheology is assumed for the upper mantle.

The total response of a Maxwell viscoelastic medium to loading consists of elastic and viscous responses. Elastic and viscous behaviours can be represented by a spring and a dashpot, respectively (Figure 2.1). Given an instantaneous stretch, the deformation of the system in Figure 2.1 is at first purely elastic (in the spring). Subsequently, viscous deformation (in the dashpot) takes place, and the elastic stress (spring) relaxes. After a long time, the Maxwell body will be completely relaxed through the viscous deformation. Shear strain in the Maxwell body is given by:

$$\varepsilon_{xy} = \varepsilon_{xy}^{E} + \varepsilon_{xy}^{V} \tag{2-6}$$

Newtonian viscous flow is assumed in the Maxwell body. Assuming that shear stress is a continuous function of time, differentiating (2-1) and (2-6) with respect to time, and combining them with (2-3), we obtain:

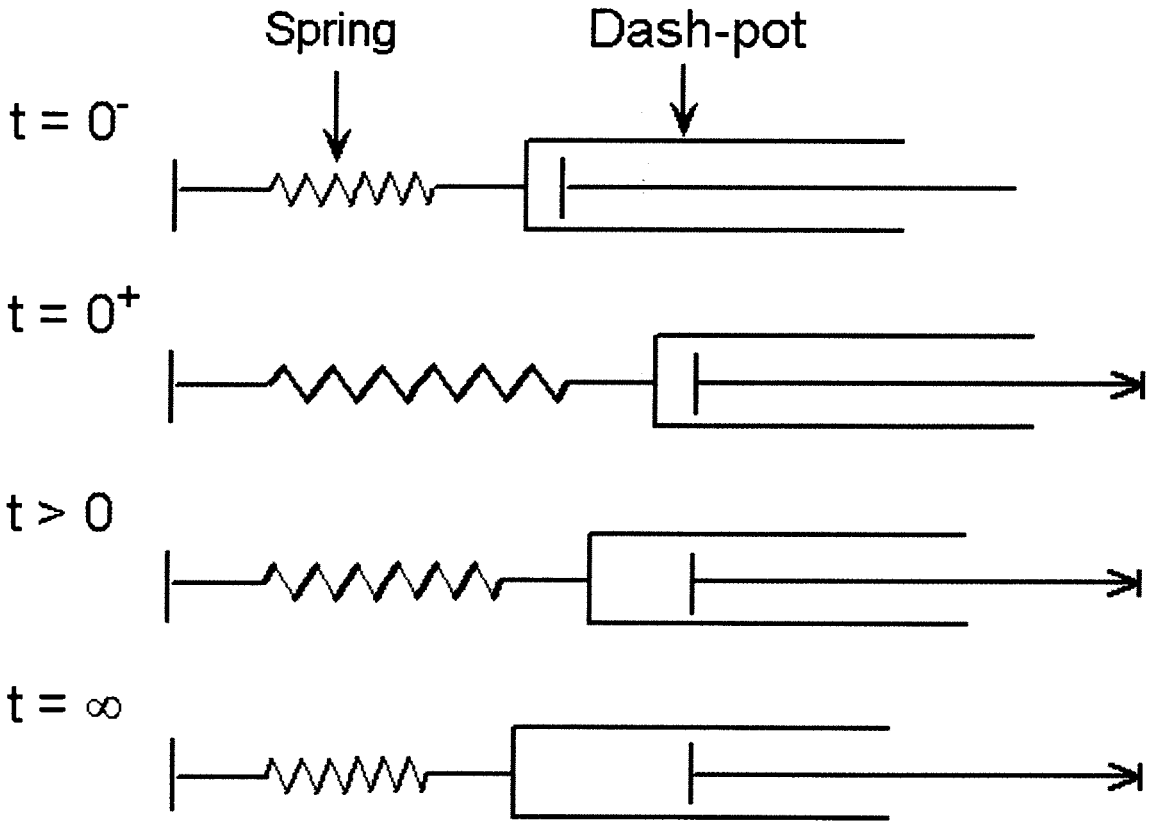

Figure 2.1. The spring and dash-pot represent elastic and viscous components in a Maxwell body, respectively. At $t = 0^-$, there is no displacement in the Maxwell body. At $t = 0^+$, the response to an instantaneous stretch is purely elastic, (the displacement is entirely in the spring). Subsequently, viscous behaviour takes place, and the spring relaxes ($t > 0$). After a long time ($t = \infty$), the stress is completely relaxed through viscous deformation.

$$\dot{\varepsilon}_{xy} = \frac{\dot{\sigma}_{xy}}{2\mu} + \frac{\sigma_{xy}}{2\eta} \tag{2-7}$$

If the shear strain is kept constant, that is, $\dot{\varepsilon}_{xy} = 0$, the solution of (2-7) for the shear stress is

$$\sigma_{xy} = \sigma_0 \exp(-\frac{\mu}{\eta} t) \tag{2-8}$$

where σ_0 is the initial shear stress, and t is time. Equation (2-8) indicates that a Maxwell body under constant shear strain exhibits exponential stress relaxation. After $T_M = \frac{\eta}{\mu}$, the stress is $\frac{1}{e}$ times the initial value. T_M is called the Maxwell relaxation time and can be rewritten in terms of the Poisson's ratio υ and the Young's modulus E:

$$T_M = \frac{\eta}{\mu} = \frac{2\eta(1+\upsilon)}{E} \tag{2-9}$$

In 3-D, the elastic strain ε^E can be written in tensor notation:

$$\varepsilon_{ij}^E = \frac{1+\upsilon}{E}\sigma_{ij} - \frac{\upsilon}{E}\sigma_{kk}\delta_{ij} \tag{2-10}$$

where σ is stress, δ is the Kronecker delta, and i and $j = x, y, z$. A repeated index indicates summation, e.g., σ_{kk} means $\sigma_{xx} + \sigma_{yy} + \sigma_{zz}$. For linear rheology, the viscous strain is defined as:

$$\dot{\varepsilon}_{ij}^V = \frac{1}{2\eta}(\sigma_{ij} - \frac{\sigma_{kk}}{3}\delta_{ij}) \tag{2-11}$$

Differentiating (2-10), and combining it with (2-11), we obtain the constitutive equation for the Maxwell material

$$\dot{\varepsilon}_{ij} = \dot{\varepsilon}_{ij}^{\ E} + \dot{\varepsilon}_{ij}^{\ V} = \frac{1+\upsilon}{E}\dot{\sigma}_{ij} - \frac{\upsilon}{E}\dot{\sigma}_{kk}\delta_{ij} + \frac{1}{2\eta}(\sigma_{ij} - \frac{\sigma_{kk}}{3}\delta_{ij}) \qquad (2\text{-}12)$$

2.1.2. Finite Element Formulation

The finite element program used in this work was developed by Jiangheng He, Pacific Geoscience Centre, Geological Survey of Canada, with the aid of the advanced version of the Finite Element Program Generator developed at the Institute of Mathematics, Chinese Academy of Science (Liang, 1991). This section very briefly outlines the mathematical formulation of the finite element method.

The stress equilibrium equation for a hydrostatically pre-stressed continuum is:

$$\nabla \cdot \sigma - \rho g \nabla w = 0 \qquad (2\text{-}13)$$

where ρ and g are density and gravitational acceleration, respectively, and w is vertical displacement. The stress tensor in this equation is the non-hydrostatic (or non-lithostatic) stress; that is, the hydrostatic component has been subtracted. If the equation were to describe the total stress, the second term would just be $\rho\vec{\mathbf{g}}$. Although the hydrostatic component is removed, its effect of tending to bring a perturbed system back to the hydrostatic state should be retained, which results in the second term $-\rho g \nabla w$ (Peltier, 1974). Therefore (2-13) describes a system different from one that completely ignores gravity.

The tensor notation used above is useful for explaining the physics, but the complexity of the equations in theoretical mechanics and the finite element theory necessitates the use of a matrix notation. With the matrix notation, the strain tensor is written as a 6 × 1 single-column matrix and called a six-dimensional (6-D) strain vector

$\epsilon = [\varepsilon_{xx}, \varepsilon_{yy}, \varepsilon_{zz}, \varepsilon_{xy}, \varepsilon_{yz}, \varepsilon_{zx}]^\tau$, where τ denotes transpose operation. Similarly, stress is written as a 6-D stress vector $\boldsymbol{\sigma} = [\sigma_{xx}, \sigma_{yy}, \sigma_{zz}, \sigma_{xy}, \sigma_{yz}, \sigma_{zx}]^\tau$.

Our computer program solves for the displacement field. Other desired quantities such as velocity, strain, and stress are derived from the displacement solution. The relation between displacement and (infinitesimal) strain is:

$$\epsilon = \mathrm{L}\mathbf{U} \tag{2-14}$$

where $\mathbf{U} = [u, v, w]^\tau$ is the 3-D displacement vector, and L is a 6 × 3 matrix of linear differentiation operator defined by

$$\mathrm{L} = \begin{pmatrix} \frac{\partial}{\partial x} & 0 & 0 & \frac{\partial}{\partial y} & 0 & \frac{\partial}{\partial z} \\ 0 & \frac{\partial}{\partial y} & 0 & \frac{\partial}{\partial x} & \frac{\partial}{\partial z} & 0 \\ 0 & 0 & \frac{\partial}{\partial z} & 0 & \frac{\partial}{\partial y} & \frac{\partial}{\partial x} \end{pmatrix}^\tau$$

Using the matrix notation, (2-12) can be expressed as:

$$\dot{\epsilon} = \mathrm{D}^{-1}\dot{\boldsymbol{\sigma}} + \mathrm{D}_v^{-1}\boldsymbol{\sigma} \tag{2-15}$$

where D and D_v are material matrices defined as

$$\mathrm{D} = \frac{E}{(1+\nu)(1-2\nu)} \begin{pmatrix} 1-\nu & \nu & \nu & 0 & 0 & 0 \\ \nu & 1-\nu & \nu & 0 & 0 & 0 \\ \nu & \nu & 1-\nu & 0 & 0 & 0 \\ 0 & 0 & 0 & \frac{1-2\nu}{2} & 0 & 0 \\ 0 & 0 & 0 & 0 & \frac{1-2\nu}{2} & 0 \\ 0 & 0 & 0 & 0 & 0 & \frac{1-2\nu}{2} \end{pmatrix} \tag{2-16a}$$

and

$$\mathbf{D}_v^{-1} = \frac{1}{2\eta}\begin{pmatrix} \frac{2}{3} & -\frac{1}{3} & -\frac{1}{3} & 0 & 0 & 0 \\ -\frac{1}{3} & \frac{2}{3} & -\frac{1}{3} & 0 & 0 & 0 \\ -\frac{1}{3} & -\frac{1}{3} & \frac{2}{3} & 0 & 0 & 0 \\ 0 & 0 & 0 & 1 & 0 & 0 \\ 0 & 0 & 0 & 0 & 1 & 0 \\ 0 & 0 & 0 & 0 & 0 & 1 \end{pmatrix} \tag{2-16b}$$

The finite element method does not solve partial differential equations like (2-13). Instead, it solves an equivalent integral equation based on the virtual work principle (Yin, 1987). The virtual work equation associated with (2-13) reads

$$\int_V \delta\epsilon^T \cdot \boldsymbol{\sigma} dV - \int_V \delta\mathbf{U}^T \cdot \rho g \nabla w dV - \int_S \delta\mathbf{U}^T \cdot \mathbf{f} ds = \mathbf{0} \tag{2-17}$$

where V is volume, S is the portion of boundary of V where traction boundary condition is prescribed, and $\mathbf{f}$ is the boundary force applied. $\delta\epsilon$ and $\delta\mathbf{U}$ are virtual strain and virtual displacement, respectively. Mathematically, they are the variations of the strain and displacement functionals. The physical meaning of (2-17) is that the total virtual work done to the system by external forces on virtual deformation equals the total incremental virtual energy. Equation (2-17) differs from (2-13) in that the physical quantities involved are no longer required to be differentiable. For this reason, this "weak form" equation is a more general and hence more fundamental statement of the physical problem. The finite element method determines the displacement function that satisfies (2-17) in the functional space.

In the finite element method, the model domain is divided into a number of elements, each having a number of nodal points. Displacement $\mathbf{U}$ in element e is represented by

nodal values using polynomial shape (or interpolation) functions. If there are M nodal points in the element

$$\mathbf{U} = \mathbf{N}\mathbf{U}_e \tag{2-18}$$

where $\mathbf{U}_e = [u_1, v_1, w_1, u_2, v_2, w_2, \ldots, u_M, v_M, w_M]^\tau$ is the $3M \times 1$ one-column matrix containing element nodal displacements, and N is a $3 \times 3M$ matrix consisting of shape functions. Thus (2-14) becomes

$$\epsilon = \mathrm{L}\mathbf{N}\mathbf{U}_e \equiv \mathbf{B}\mathbf{U}_e \tag{2-19}$$

The interpolation of the vertical displacements in the element is

$$w = \mathrm{I}_w\mathbf{U} = \mathrm{I}_w\mathbf{N}\mathbf{U}_e \tag{2-20}$$

where $\mathrm{I}_w = [0,0,1]$. Note that the $1 \times 3M$ matrix $\mathrm{I}_w\mathrm{N}$ is simply the third row of N.

Combining (2-17) and (2-19), noting that $\delta\epsilon = \mathrm{B} \cdot \delta\mathbf{U}$, and dropping the resultant common factor $\delta\mathbf{U}_e$, we obtain the following virtual work equation for element e:

$$\int_e \mathrm{B}^\tau \boldsymbol{\sigma} dV - \int_e \mathrm{N}^\tau \rho g \nabla(\mathrm{I}_w\mathrm{N})\mathrm{U}_e dV = \int_{S\cap e} \mathrm{N}^\tau \mathbf{f} ds \tag{2-21}$$

where $\nabla = \left[\frac{\partial}{\partial x}, \frac{\partial}{\partial y}, \frac{\partial}{\partial z}\right]^\tau$ is understood to be a 3×1 matrix operator.

To use our specific constitutive relation with (2- 21), we need to deal with the time dependence in the Maxwell rheology. To do this, we apply a backward difference scheme for the time to (2-15), which yields

$$\mathrm{D}\frac{\epsilon^{n+1} - \epsilon^n}{\Delta t} = \frac{\boldsymbol{\sigma}^{n+1} - \boldsymbol{\sigma}^n}{\Delta t} + \mathrm{D}\mathrm{D}_V^{-1}\boldsymbol{\sigma}^{n+1} \tag{2-22}$$

where Δt is time step length, which does not have to be constant. Therefore, stress at time step $n+1$ is:

$$\boldsymbol{\sigma}^{n+1} = \mathrm{D}_s^{-1}\mathrm{D}(\boldsymbol{\epsilon}^{n+1} - \boldsymbol{\epsilon}^{n}) + \mathrm{D}_s^{-1}\boldsymbol{\sigma}^{n} \tag{2-23}$$

where $\mathrm{D}_s = \mathrm{I} + \Delta t\,\mathrm{D}\mathrm{D}_v^{-1}$ with I being the identity matrix. Equation (2-23) shows that stress at a given time step can be determined from strain of the same time step and stress and strain of the previous time step.

Substituting (2-23) into (2-21) at time step $n+1$ and writing strain in terms of nodal displacement using (2-19), we obtain

$$\mathrm{K}_e^{n+1}\mathbf{U}_e^{n+1} = \mathbf{F}_e^{n+1} \tag{2-24}$$

where

$$\mathrm{K}_e^{n+1} = \int_e \mathrm{B}^{\tau}\mathrm{D}_s^{-1}\mathrm{D}\mathrm{B}dV - \int_e \mathrm{N}^{\tau}\rho g\nabla(\mathrm{I}_w\mathrm{N})dV$$

is the elemental stiffness matrix, and

$$\mathbf{F}_e^{n+1} = \int_{S\cap e} \mathrm{N}^{\tau}\mathbf{f}ds + \int_e \mathrm{B}^{\tau}\mathrm{D}_s^{-1}\mathrm{D}\boldsymbol{\epsilon}^{n}dV - \int_e \mathrm{B}^{\tau}\mathrm{D}_s^{-1}\boldsymbol{\sigma}^{n}dV$$

is the elemental equivalent nodal force vector. The global stiffness matrix K^{n+1} and nodal force vector $\mathbf{F}^{n+1}$ are obtained by summing up elemental $\mathbf{K}_e^{n+1}$ and $\mathbf{F}_e^{n+1}$, respectively, over all elements. That is, for each time step we solve the global algebraic system

$$\mathrm{K}^{n+1}\mathbf{U}^{n+1} = \mathbf{F}^{n+1} \tag{2-25}$$

for the global nodal displacement vector $\mathbf{U}^{n+1}$. Pre-stress σ_0 at $n = 0$ may or may not be zero. Displacement at each time step is calculated from (2-25). Strain and stress at the corresponding time step are determined from (2-19) and (2-23), respectively. For linear rheology such as the Maxwell rheology used in this work, K^{n+1} may vary between time steps only because of different Δt values. For nonlinear rheology such as (2-4) and (2-5), K^{n+1} will depend on $\mathbf{U}^{n+1}$, and (2-25) will have to be solved iteratively. The split-node

method (Melosh and Raefsky, 1981) is used in the finite element code to model discontinuous displacements (slip) along faults.

2.2. Benchmarking of the Modelling Code

Given that no 3-D viscoelastic analytical solutions are available, two steps are taken to benchmark the computer program. First, comparison is made with an analytical solution for a 2-D viscoelastic problem. This provides a test on how the code handles viscoelastic rheology and time-dependant deformation. Second, a 3-D analytical solution for a purely elastic dislocation problem is used to test the code's 3-D performance in the presence of faulting.

2.2.1. 2-D Viscoelastic Boxcar Model

I compare analytical and numerical solutions for the Heaviside response of a thin incompressible, hydrostatically pre-stressed Maxwell viscoelastic channel to a 2-D boxcar load of half-width L (Figure 2.2a). The vertical displacement at the top surface of the channel is given by (Wu, 1992):

$$w(x) = \int_{-\infty}^{+\infty} \frac{-\sigma_A L(k)}{\rho g + 2\mu k\gamma}\left(1 + \frac{2\mu k\gamma}{\rho g}\left(1 - e^{\beta t}\right)\right)e^{ikx}dk \qquad \text{(2-26a)}$$

where σ_A is the magnitude of the 2-D boxcar load, ρ is density, g is gravitational acceleration, μ is shear modulus, k is wavenumber, $L(k)$ is the representation of the unit boxcar load in the k domain, x is distance from the load centre, and the relaxation time β and γ are given by:

$$\beta = \frac{\rho g \mu}{\eta(\rho g + 2\mu k \gamma)} \tag{2-26b}$$

$$\gamma = \frac{(\cosh(kH))^2 + (kH)^2}{\cosh(kH)\sinh(kH) - kH} \tag{2-26c}$$

where η is the viscosity, and H is the thickness of the channel. The same solution has been used by Wu (1992) to benchmark his finite element code for post-glacial rebound analysis. The FORTRAN source code that I used to compute the vertical displacement given by this analytical solution was written by Jiangheng He, Pacific Geoscience Centre, Geological Survey of Canada.

Because of the symmetry of the problem, we only need to consider one half of the model domain to the right of the centre of the boxcar load. A 2-D boxcar load of magnitude 15 MPa with a 1000 km half-length is assumed in this test. The uniform channel is assumed to be 100 km thick. The top boundary except the load area is a free surface. Because of the symmetry condition, horizontal displacement at the left boundary is zero but vertical deformation is free. At the bottom, the vertical displacement is zero, but deformation in the horizontal direction is free. The right-hand-side boundary is set 20,000 km away (200 times the channel thickness) to approximate the laterally infinite channel. The finite element mesh from 0 to 4,000 km distance is shown in Figure 2.2a. The mesh from 4,000 km to 20,000 km (not shown) is similar to that in Figure 2.2a but with horizontally wider elements. Elements most distant from the load area are more than 500 km in horizontal dimension. Displacement around the edge of the boxcar load (x = 1000 km) changes sharply, and therefore elements less than 1 m in size are used in this area to provide sufficient accuracy. The analytical solution (2-26a) requires an incompressible material. The incompressibility is approximated using a Poisson's ratio of

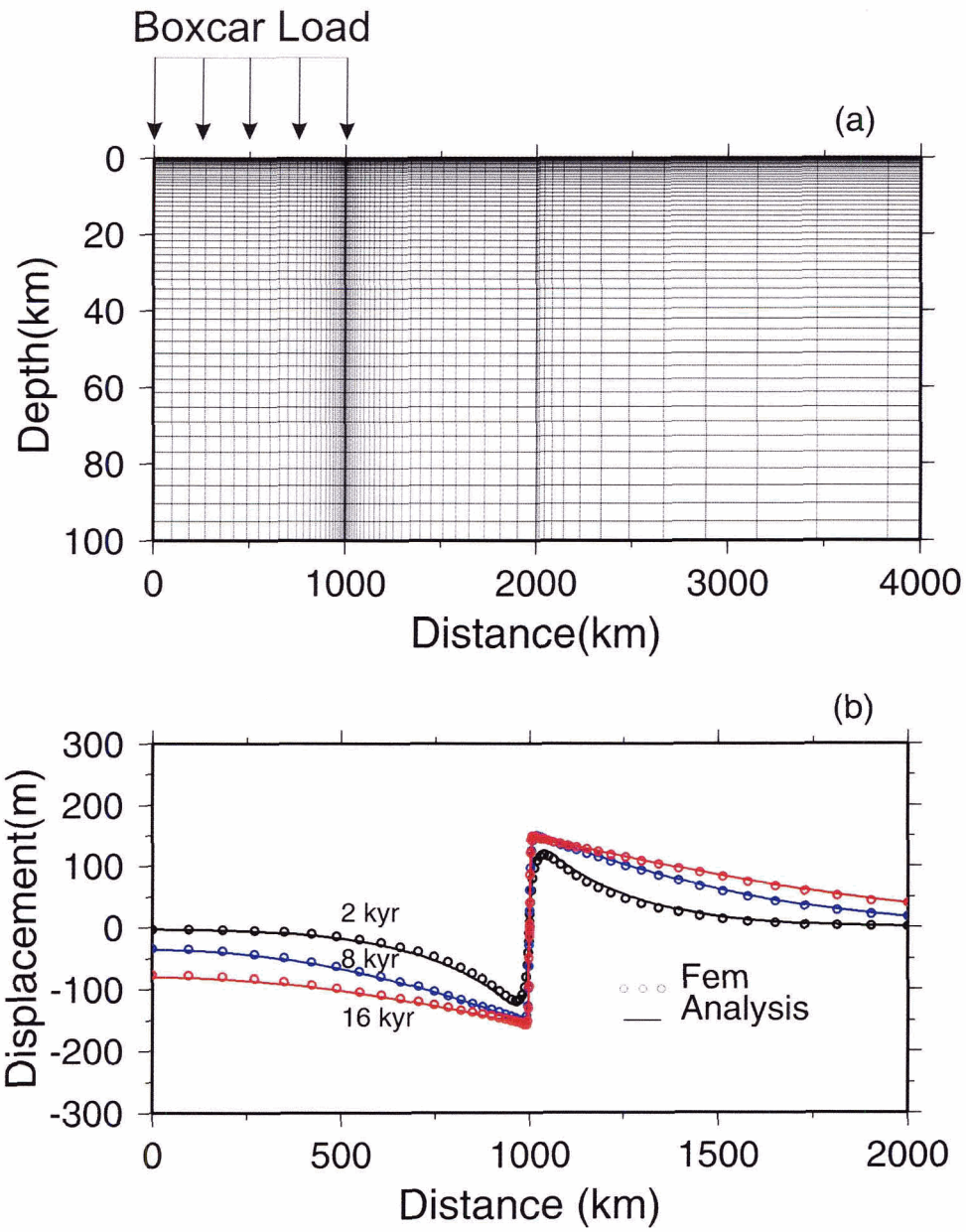

Figure 2.2. 2-D viscoelastic Boxcar model. (a) The finite element mesh (the entire mesh is from 0 to 20,000 km). The load is a 2-D boxcar with a magnitude of 15 MPa and a 1,000 km half length. (b) Vertical displacement at zero depth. Solid lines represent analytical solutions. Circles represent model results.

0.4999 in the finite element model. Numerical difficulties of modelling incompressible materials are alleviated by the use of the B-bar method (Hughes, 1980, 1987). Δt for each time step varies from 10^5 seconds at the beginning of the run to 10^3 years near the end (2×10^4 years). Other model parameters are listed in Table 2.1. According to (2-9), the Maxwell time T_M for this system is 16.8 years.

Calculated surface vertical displacements are shown in Figure 2.2b. Model results (circles) agree well with the analytical solution (solid lines). In the load area from 0 to 1000 km, downward displacement (negative values) increases with time. This indicates viscous creep under the constant load. At distances larger than 1000 km, the displacement is upward (positive values). Because the material is incompressible, pressing part of the channel downward leads to upward creeping in other areas. The flow of material is the fastest around the edge of the load (1000 km), which causes large contrasting displacements on both sides of the edge (Figure 2.2a). After a long time ($t >> T_M$), displacements within and outside the load area (0 to ~1000 km) will both be uniform but with opposite signs. Figure 2.2b indicates that the program yields accurate results in numerically calculating viscoelastic deformation. Compared to Wu's (1992) finite element results for the same solution, our code yields much more accurate results.

Table 2.1. Parameters of the benchmarking models.

Property / Models	Viscosity (Pa s)	Young's modulus (GPa)	Poisson's ratio	Density (kg/m^3)	gravity (m/s^2)
Boxcar Model	3.03×10^{19}	1.13×10^{11}	0.4999	5000	9.82
Okada Model	∞	1.2×10^{11}	0.25		

2.2.2. Rectangular Fault in an Elastic Half Space

Okada (1985, 1992) presented a complete set of analytical expressions for internal displacements due to shear and tensile faults in an elastic half-space for both point and finite rectangular sources. The analytical solution for a 100 × 100 km rectangular fault with a 15° dip is used to compare with finite element modelling results in this section (Figure 2.3). The updip edge of the fault is arbitrarily assumed to be "buried" at 0.2 km depth. A uniform 10-meter pure-thrust slip is applied over the rectangular fault. In the finite element model, the slip discontinuity at the fault edges (step change from 10-m to zero slip) requires the use of small elements. As a result of the split-node formulation for faulting (Melosh and Raefsky, 1981), the transition from 10-m slip to no slip occurs linearly over one element. Therefore smaller elements around the edges better approximate the singularity. However, results away from these edges are not very sensitive to the sharpness of the transition. If the size of the elements surrounding the fault is less than 5 km, calculated surface deformation matches the analytical solution very well except right above the shallower parts of the edges. In areas far away from the fault, element size is 500 km or more. Model parameters are listed in Table 2.1.

Surface horizontal and vertical displacements along lines parallel to the y axis (in the dip direction of the rectangular fault) are plotted in Figure 2.4. The model results agree well with the analytical solutions even though most elements are as large as about 40 km. The spike in the surface vertical displacement in the analytical solution near distance 0 (Figure 2.4c) results from the buried fault; that is, the thrust motion of the fault squeezes the material above its updip edge to cause extremely large localized uplift. The finite element solution does not have this sharp peak because of the large element size (5 km)

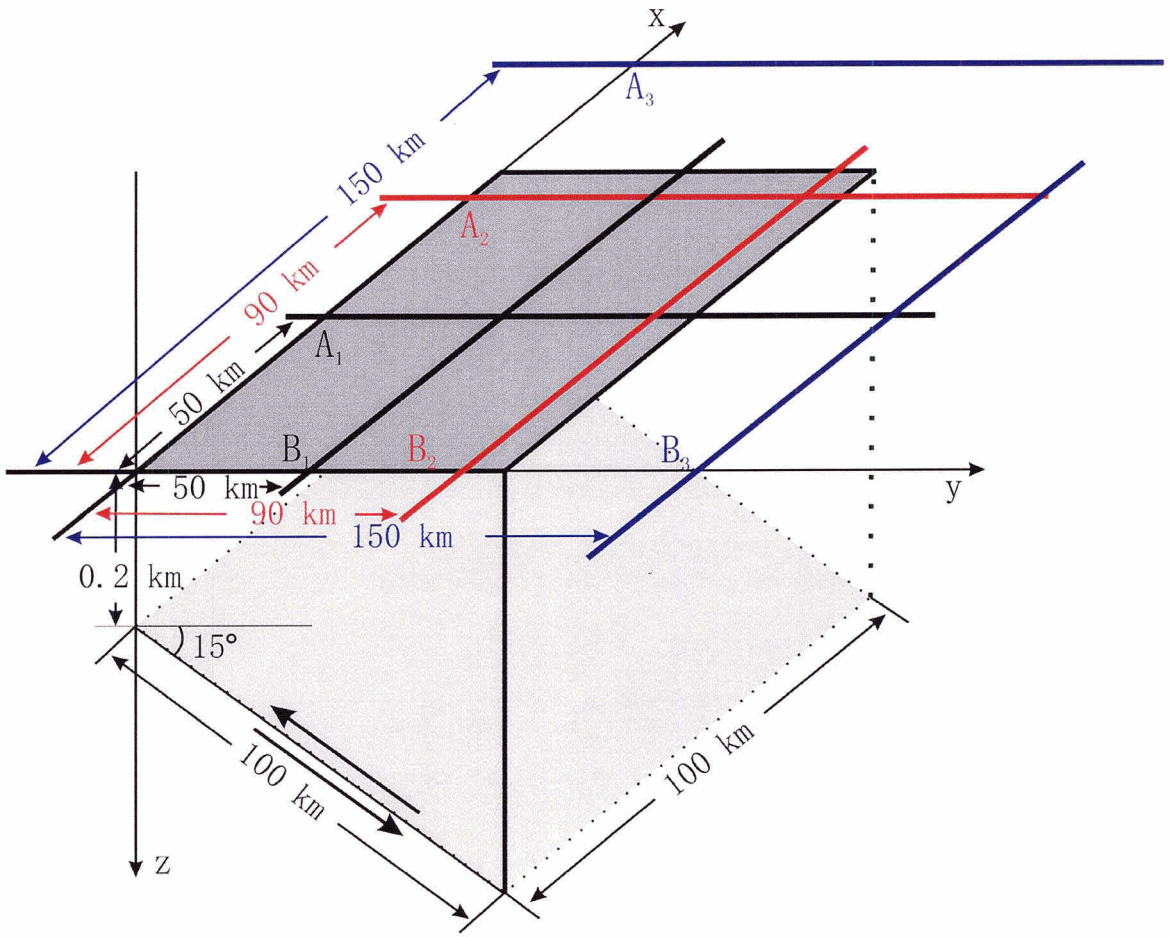

Figure 2.3. 3-D elastic Okada (1992) model. The rectangular fault with 100 × 100 km width and length is 15° dip. The updip edge of the fault is 0.2 km in depth. Results will be plotted along lines A_1, A_2, A_3, B_1, B_2, and B_3 in Figures 2.4 and 2.5.

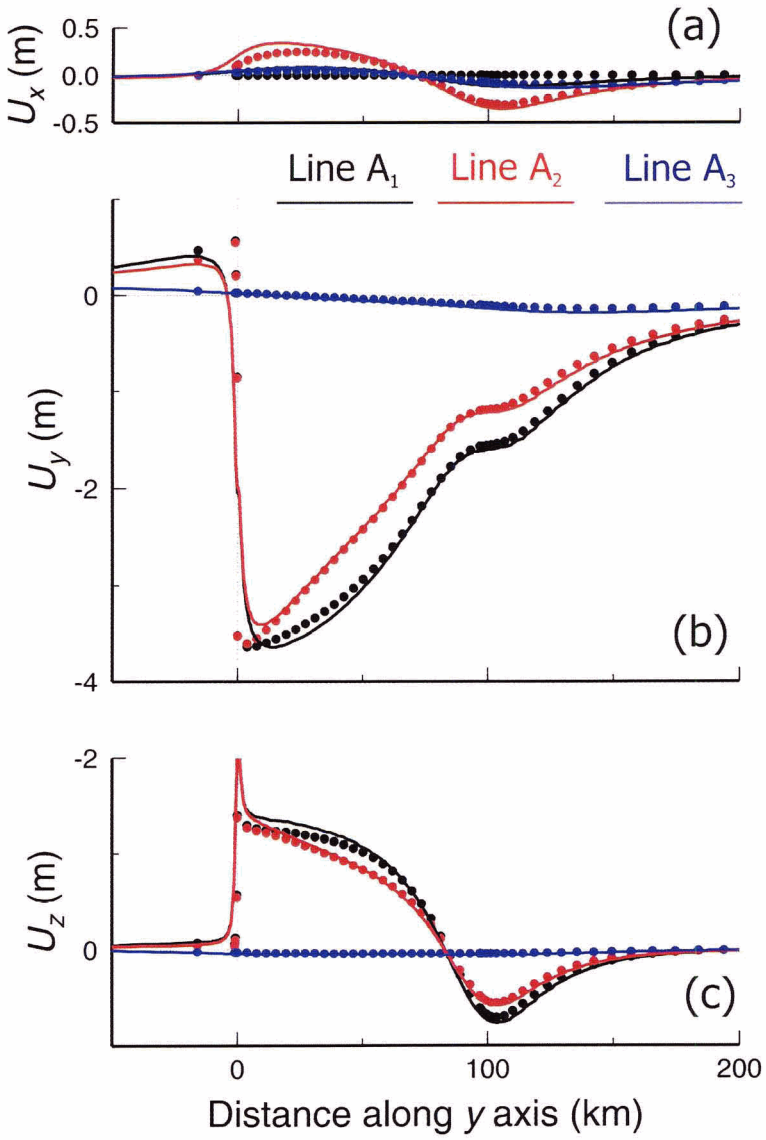

Figure 2.4. Surface displacements along lines A_1 (black), A_2 (red) and A_3 (blue) in Figure 2.3. Solid lines and circles represent analytical and finite element results, respectively. (a) Strike-parallel displacement U_x. (b) Trench-normal displacement U_y. (c) Surface vertical displacement U_z.

in this area. Using smaller elements in this area would improve the accuracy.

Surface horizontal and vertical displacements along lines B_1, B_2 and B_3 parallel to the x axis (in the strike direction) are plotted in Figure 2.5. The model results agree well with the analytical solutions.

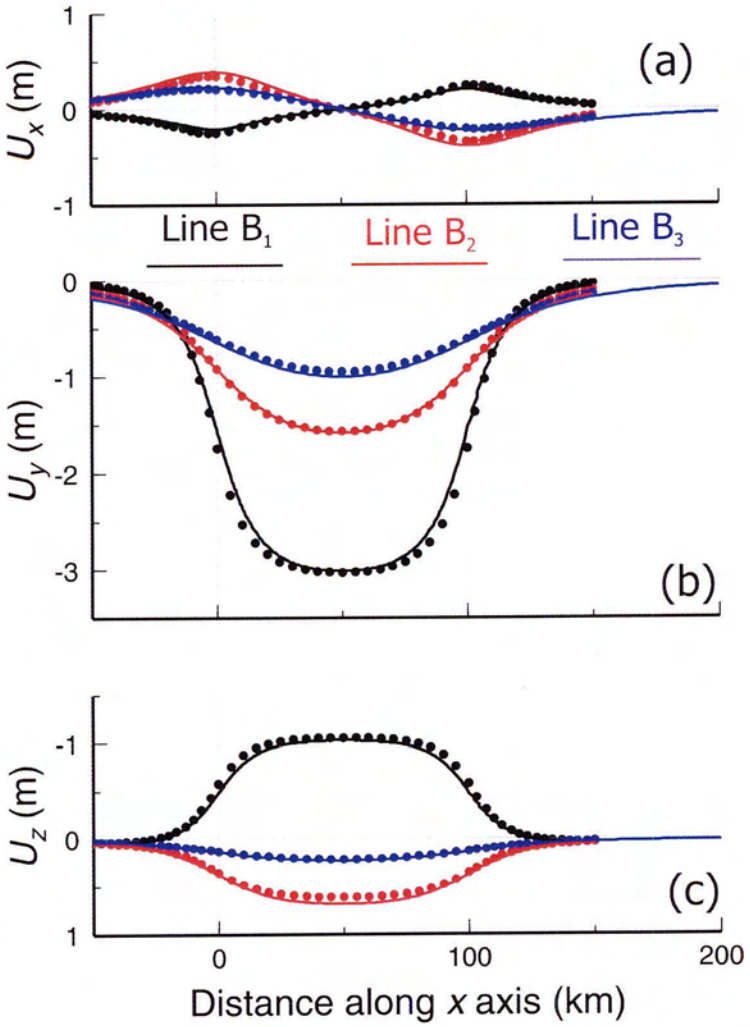

Figure 2.5. Surface displacements along lines B_1 (black), B_2 (red) and B_3 (blue) in Figure 2.3. Solid lines and circles represent analytical and finite element results, respectively. (a) Strike-parallel displacement U_x. (b) Trench-normal displacement U_y. (c) Surface vertical displacement U_z.

Chapter 3. Viscoelastic Finite Element Modelling

3.1. Model Concept

The model used to study postseismic and interseismic deformation is schematically shown in Figure 3.1. The model consists of an elastic oceanic plate (and slab), an elastic continental plate, and a viscoelastic upper mantle. For a subduction fault in the interseismic period, a shallow portion is assumed to be locked (locked zone), and from a certain depth downdip, the fault is assumed to slip at the full plate convergence rate. In the locked zone, the slip deficit accumulated during the interseismic period is assumed to be completely recovered in future earthquakes. After removing steady state plate convergence, the locked zone of the fault can be equivalently described as to slip backwards slowly, and the slip deficit becomes backslip (Savage, 1983). In reality, the fault slip over the locked zone is likely to be time dependant and may be better described with a laboratory-derived time- and state-dependent friction law (Ruina, 1983; Dieterich, 1978, 1994). The present work is designed to understand crustal deformation in response to given faulting motion, not the mechanics of the fault itself. Therefore, slip along the fault is kinematically prescribed.

Although in general the crust at shallow depths deforms elastically in earthquake cycles, it is coupled with the more viscous rocks at greater depths (lower crust and the mantle). The rheology of the upper mantle may play an essential role in controlling postseismic and interseismic deformation of the upper crust. For models with a purely elastic medium (e.g., the dislocation model), given medium properties, fault geometry

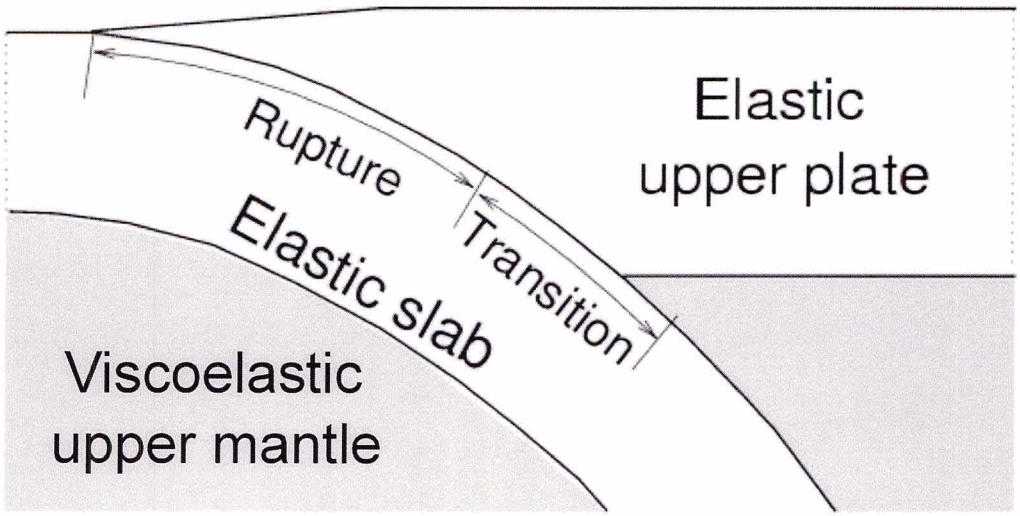

Figure 3.1. Conceptual representation of the subduction zone model (modified from Wang et al., 2001).

and plate convergence rate, the model results are controlled only by the position and size of the locked zone and a transition between zones of no slip and full slip. But for models with a viscoelastic medium (e.g., the model used in this chapter), stress relaxation of the viscoelastic medium greatly contributes to the postseismic and interseismic crustal deformation. Details of this effect will be discussed in sections 3.3 and 3.4.

3.2. Slip Budget and Decomposition

The simplest view of an earthquake cycle is that the fault is completely locked during the interseismic period, and the accumulated slip deficit is completely recovered during an earthquake. This process can be illustrated by the stairway case in Figure 3.2a. The other end-member scenario is that the fault slips continuously and aseismically at all times, as shown by the straight dashed line in Figure 3.2a. The dot-dashed line in Figure 3.2a describes an intermediate case in between. In the real Earth, the fault slip distribution is likely to be a complicated function of space and time. For example, some parts of the locked zone may slip aseismically before and/or after an earthquake; some parts of the locked zone may slip aseismically during an interseismic period; and the size of the locked zone may change with time in response to thermal, chemical, and hydrogeological processes. My work focuses on the first-order behaviour of the mechanical system. For simplicity, the faulting behaviour has been idealized. In the model, any aseismic slip is averaged over the entire interseismic period, such that the fault slips interseismically at a constant rate that is less than the plate convergence rate ("partial locking"). The same treatment of fault motion was used by Zheng et al. (1996).

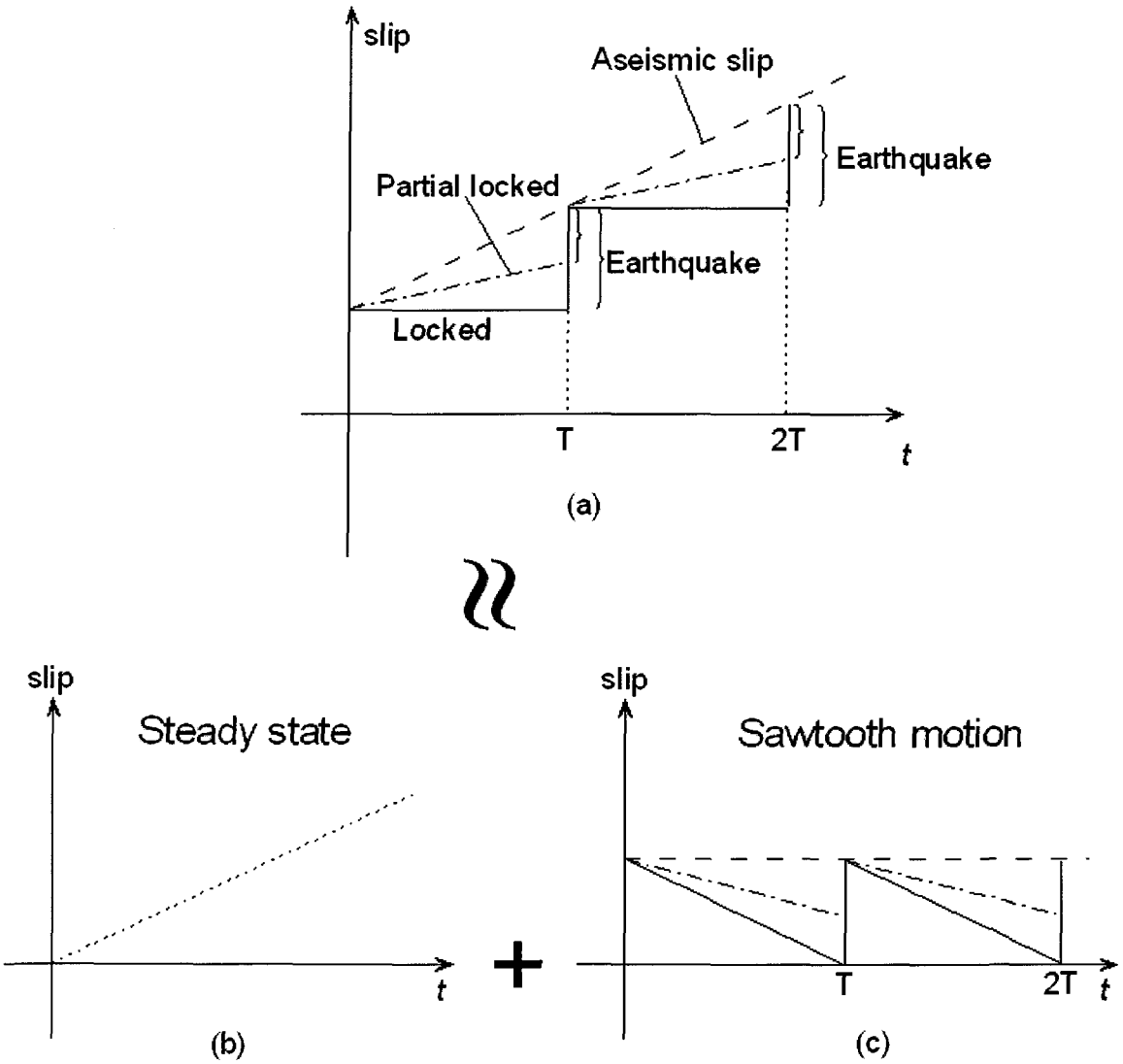

Figure 3.2. Decomposition of fault slip into a steady slip and a sawtooth motion. Dashed and solid lines represent aseismic slip and purely seismic slip, respectively, and dash-dotted line represents an intermediate case.

The slip budget in Figure 3.2a can be described as a superposition of steady plate motion shown in Figure 3.2b and repetitive cycles of a sudden forward slip (earthquake) followed by backward slow slip (slip deficit) shown in Figure 3.2c. It is assumed that the steady motion component has no contribution to crustal deformation and is subtracted from the model. Therefore, we only need to consider the sawtooth cyclic component. With this decomposition, the aseismic component of the fault motion (assumed to be continuous slow slip) in the interseismic period is removed as part of the steady state plate motion. In other words, the effect of partial aseismic interseismic slip is modelled using a slower backslip rate.

Deformation of a viscoelastic Earth in an earthquake cycle (the sawtooth fault motion) is therefore a combination of that caused by the coseismic forward slip (EQ) and that caused by the interseismic backslip (BK). If we denote deformation purely in response to a unit earthquake slip S_{EQ}, and deformation purely in response to unit backslip rate S_{BK}, the total (time-dependent) deformation S_{total} can be described as:

$$S_{total} = M(aS_{EQ} + bS_{BK}) \qquad M \in (0,\infty), a \in [0,1], b \in [0,1] \tag{3-1}$$

where M, a, and b are scaling constants. By changing the values of these constants, (3-1) describes crustal deformation in response to a range of coseismic slips and plate convergence rates.

Figure 3.3a illustrates two models with the same coseismic slip ($a = 1$) but different subduction rates, $b = 1$ and $b = 0.5$ (solid and dashed lines, respectively). If the cycle length for the subduction zone with the subduction rate 1 ($b = 1$) is T, it takes $2T$ for the subduction zone with the subduction rate 0.5 ($b = 0.5$) to complete an earthquake cycle.

Figure 3.3b illustrates two models with the same plate convergence rate ($b = 1$) but

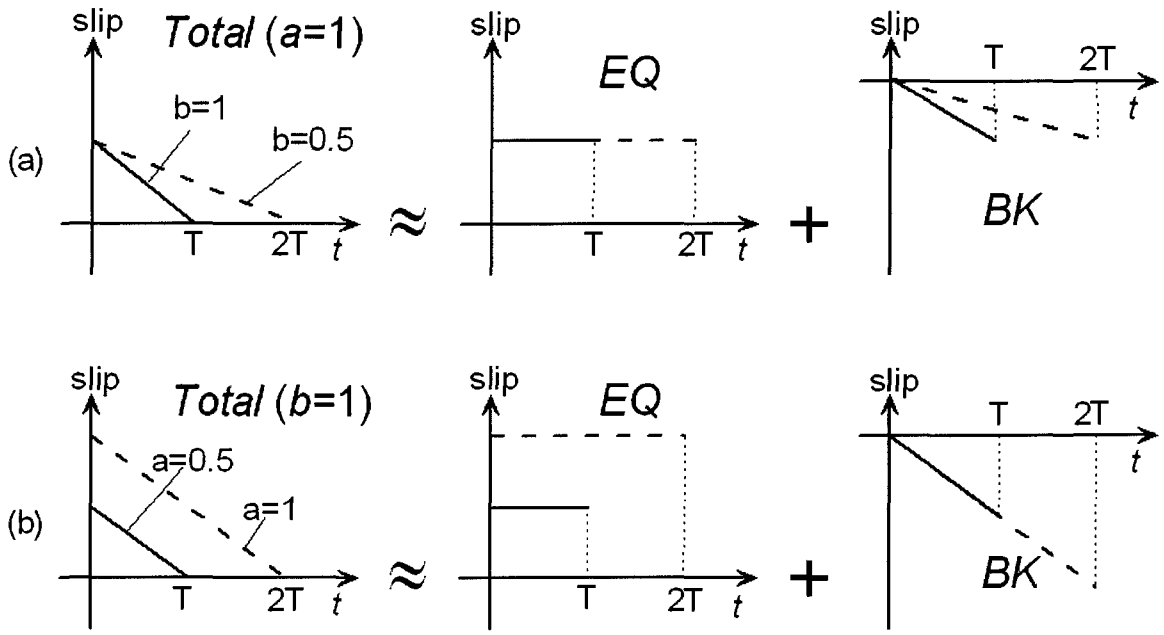

Figure 3.3. Decomposition of the sawtooth motion in Figure 3.2c into an earthquake event and fault slip deficit (backslip) in an earthquake cycle. *EQ* and *BK* represent the earthquake event and the fault slip deficit, respectively. (a) Two models with the same coseismic slip but different subduction rates. (b) Two models with the same subduction rate but different coseismic slips.

different coseismic fault slips, $a = 1$ and $a = 0.5$ (dashed and solid lines, respectively). If the cycle length for the subduction zone with the coseismic fault slip 0.5 is T, the cycle length for the subduction zone with the coseismic fault slip 1.0 is 2T.

3.3. Relaxation of the System

"Relaxation" in this thesis means that stress decreases with time subject to an externally imposed and fixed displacement field. Velocity becomes smaller due to the effect of stress relaxation. A schematic model in Figure 3.4 is used to illustrate the relaxation of the system. Trench-normal displacements along surface line AB in response to an instantaneous (coseismic) slip assigned to the fault are schematically shown in Figure 3.5 ($t = 0$). Stress in a deformed purely elastic body, that is, if the mantle viscosity is ∞, never relaxes (Figure 3.5a). With an inviscid mantle, that is, if the mantle viscosity equals 0, the mantle relaxes instantly (Figure 3.5b). With a finite mantle viscosity (Figures 3.5c, 3.5d), the coseismic deformation ($t = 0$) is the same as that of a purely elastic system (Figure 3.5a). After a long time $t = \infty$ ($t >> T_M$, where T_M is the Maxwell time), the system is completely relaxed, and the displacement (Figure 3.5c, 3.5d) is the same as that of an elastic plate on top of an inviscid fluid (Figure 3.5b). However, at a given time $0 < t < \infty$ (e.g., t_1 or t_2 in Figure 3.5c), displacement with a smaller upper mantle viscosity (Figure 3.5c) is closer to the completely relaxed state than that with a larger viscosity. This means that stress in the system with a smaller viscosity relaxes faster than that with a larger viscosity. It can be shown that in Maxwell viscoelastic deformation, time scales with viscosity and hence the Maxwell time. Obviously, the system with a smaller viscosity has a faster deformation rate (velocity) after the

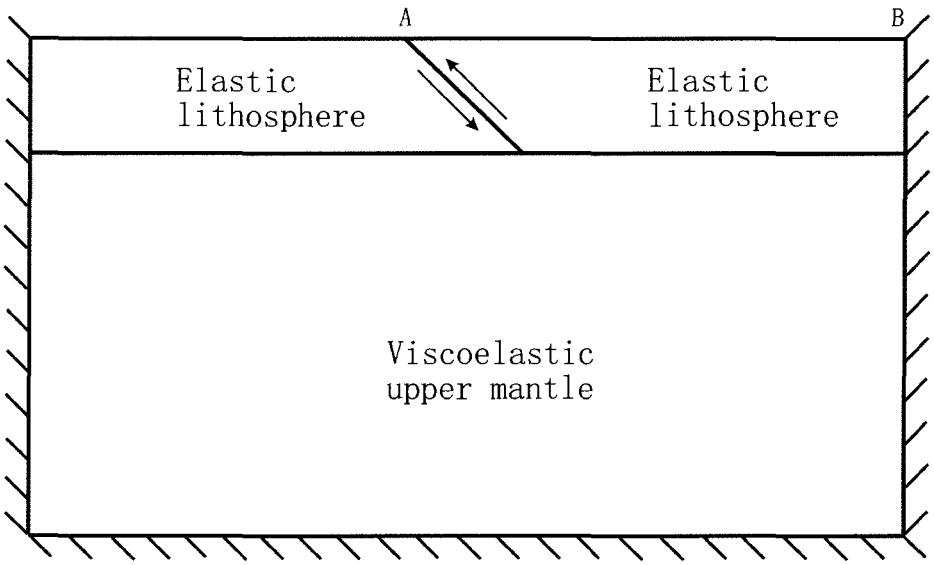

Figure 3.4. A schematic figure of a subduction boundary. Surface horizontal displacement along AB in response to thrust faulting will be plotted in Figure 3.5.

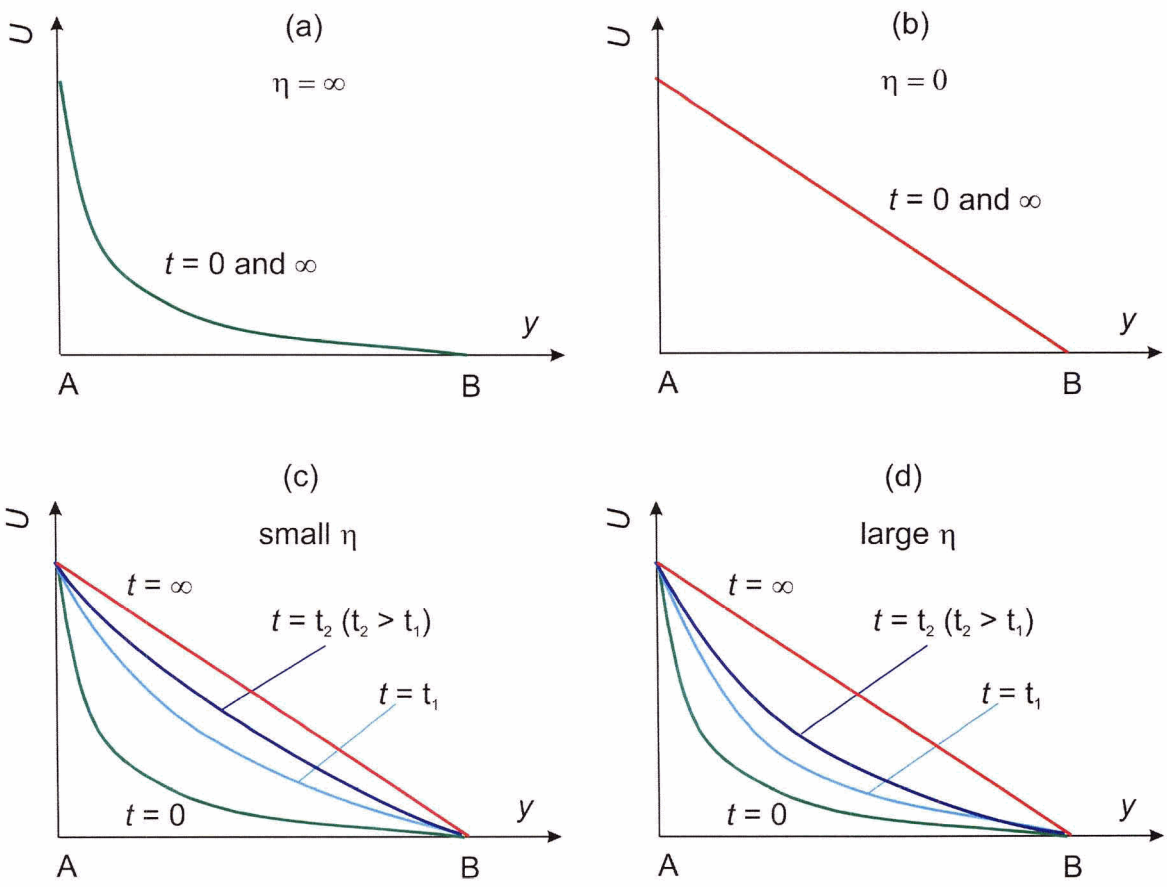

Figure 3.5. A schematic illustration of crustal deformation in response to a subduction zone earthquake. *U* is trench-normal surface horizontal displacement along line AB in Figure 3.4. (a), (b), (c) and (d) describe deformation with different upper mantle viscosities η. *t* denotes time. t_1 and t_2 represent two different time points.

earthquake. Because geodetic data usually provide deformation rates (e.g., velocities and strain rates) not displacements, discussions in the rest of the thesis will focus on velocity patterns.

For the imposed earthquake deformation in my model, stresses in the elastic plates do not begin to relax until stresses in the viscoelastic neighbour (the upper mantle) do. The relaxation of the viscoelastic upper mantle and its interaction with the elastic plates lead to material flow. When the flow will stop, that is, when the system is relaxed, depends on the mantle viscosity.

3.4. 2-D Subduction Zone Models

3.4.1. A Reference Model

Model parameters in Table 3.1 are used to derive a theoretical 2-D reference model of crustal deformation in subduction zone earthquake cycles with a unit coseismic fault slip and a unit subduction (backslip) rate. The thicknesses of the oceanic plate (and slab) and continental plate are assumed to be the same (h). The cycle length is assumed to be 30 upper-mantle Maxwell time T_M. This cycle length is chosen so that the system is nearly relaxed at the end of each cycle (see subsequent discussions). A one-meter coseismic slip is assumed, but the results can be linearly scaled for any coseismic slips. Using parameters in Table 3.1, the Maxwell time of the upper mantle is 15 years. The unit subduction rate is assumed to be $\frac{1m}{30T_M} = 2.22 \ \ mm/yr$ and the results can be scaled using (3-1). If we multiply both the unit coseismic slip and the backslip rate by 20 (the M constant in equation (3-1)), the reference model represents an earthquake cycle of a

Table 3.1. Reference model parameters. Density: 3,300 Km/m^3, gravitational acceleration: 10 m/s^2

Property / Layers	Viscosity (Pa s)	Young's modulus (GPa)	Poisson's ratio	Thickness (km)
Elastic	∞	1.2×10^{11}	0.25	$h = 30$
Viscoelastic	3.0×10^{19}	1.6×10^{11}	0.25	$15h$

20-meter coseismic slip followed by 450 years of fault locking with a convergence rate of 4.4 cm/yr. Widths of the locked and transition zones are both assumed to be $2h$. For simplicity, the fault is assumed to be straight in the downdip direction with a dip of 15°. The z-axis is oriented downward, and the y-axis is oriented landward. The centre of reference is fixed at the trench. The updip end of the fault is at the trench and at a depth of 0.2 km.

The finite element mesh used for modelling is shown in Figure 3.6. According to tests with dense and sparse model meshes, meshes with elements of 10 km horizontal dimension around the fault provide adequate accuracy.

The fault does not reach the surface because of practicality of mesh construction, and elements there are small with less than 10 m vertical nodal spacing. Coseismic slip badly deforms the elements around the updip end of the fault, and hence the displacements in that area are not reliable (see discussion on a similar problem in section 2.2.2), but displacements a few tens of kilometres away are little affected.

The reference model is used to study the effect of system relaxation discussed in section 3.3. Because of the presence of purely elastic units such as the subducting and overriding plates, it takes much longer for the subduction system to relax after an

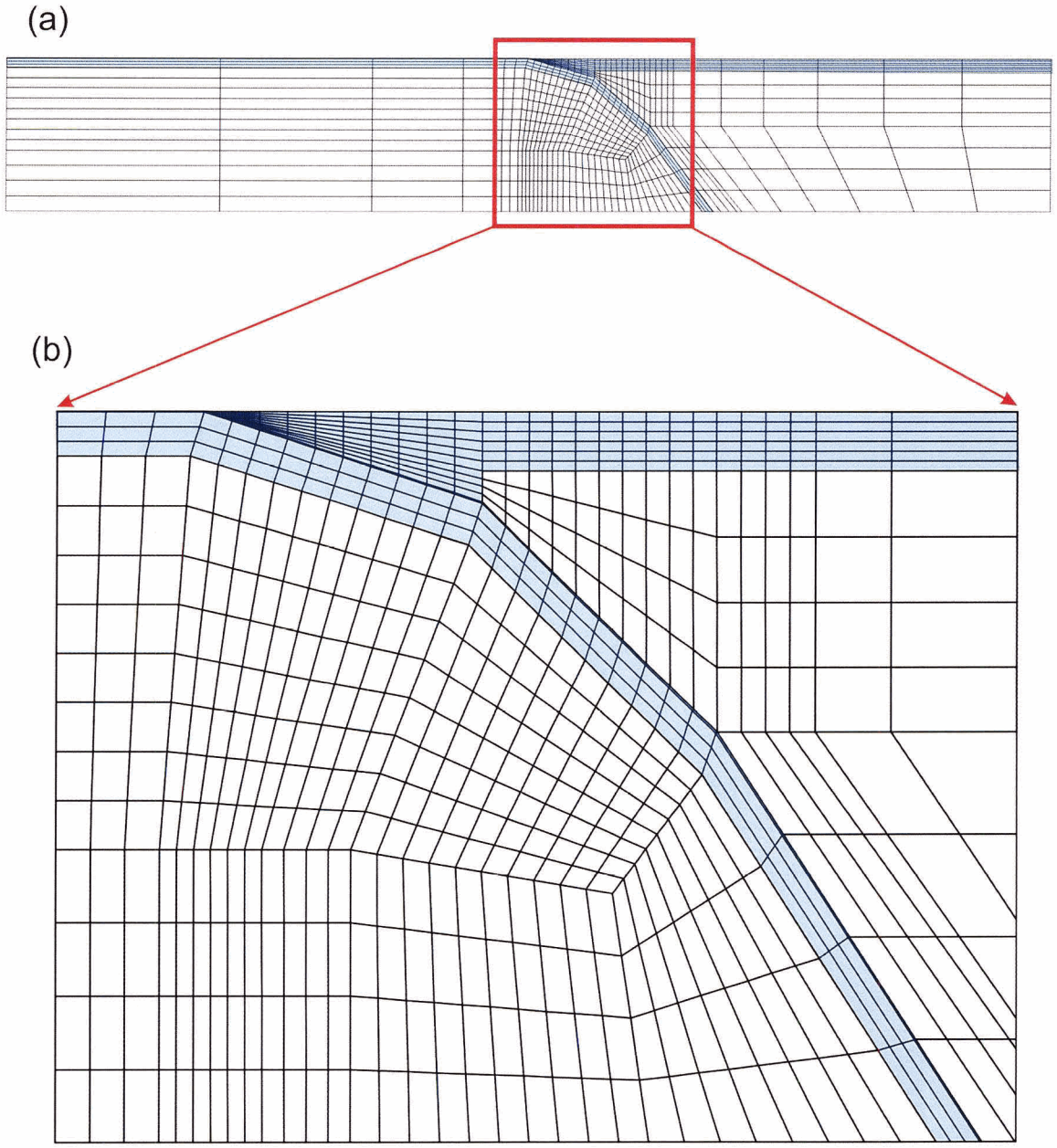

Figure 3.6. Finite element mesh used for the modelling. Coloured elements represent elastic plates. White elements represent viscoelastic upper mantel. (a) Entire mesh. (b) Centre part of the mesh.

earthquake than for a purely Maxwell body. Surface velocities purely in response to a single earthquake without subsequent locking of the fault (no backslip) are shown in Figure 3.7. The velocities are relative to distant model boundaries not the trench. This is why the horizontal velocity at the trench is not zero even though there is no backslip. The trench position slowly moves back and forth in earthquake cycles. We believe this is a physically reasonable behaviour but is neglected in most earthquake cycle models. Horizontal velocity Vy^{EQ} is negative except near the trench and depicts the upper plate's tendency to catch up with the coseismic motion of its most seaward part. At a distance $5h$ – $10h$, the horizontal velocity at $25T_M$ (25 mantle Maxwell time) is less than 10% of that at $5T_M$. The system is practically relaxed $25T_M$ after the earthquake. The surface velocities approach zero at $85T_M$ after the earthquake. Different upper mantle viscosities have been tested to study the relationship between the system relaxation time and the upper mantle Maxwell time. Generally, the system can be considered relaxed at a time about $25T_M$.

Surface velocities at 5 T_M and $25T_M$ in response to the earthquake (Vy^{EQ} and Vz^{EQ}) without subsequent fault locking are re-plotted in the upper panels of Figure 3.8. Both horizontal and vertical velocities decrease with time because of the relaxation of the system discussed above.

Surface velocities in response to fault locking without the preceding earthquake are plotted in the middle panels of Figure 3.8. The peak value of the surface vertical velocity increases with time. Surface horizontal velocity at distances $>3h$ increases with time. This represents landward spread of the effect of fault locking with on-going plate motion. However, surface horizontal velocity at distances $0h$ – $3h$ changes only slightly with time

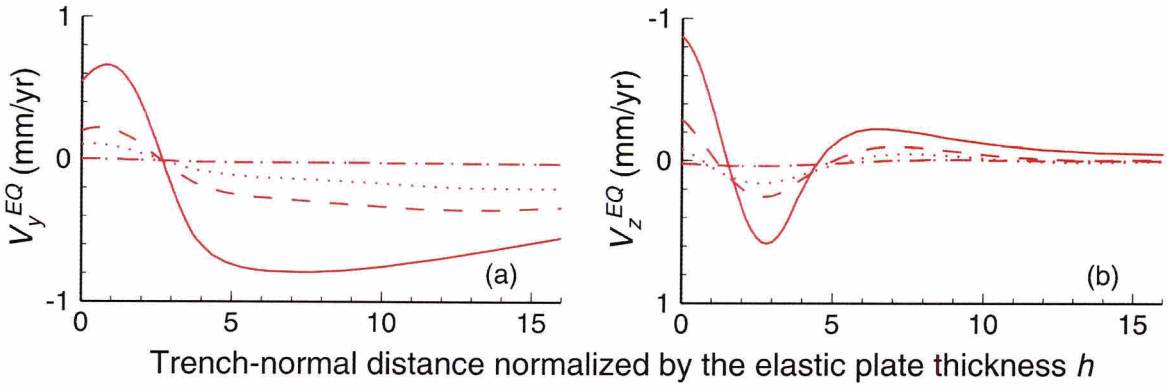

Figure 3.7. Surface velocities of the reference model, in response to an earthquake alone, at different times: $5T_M$, $15T_M$, $25T_M$, and $85T_M$ (from solid line to dot-dashed line), where T_M is the mantle Maxwell time.

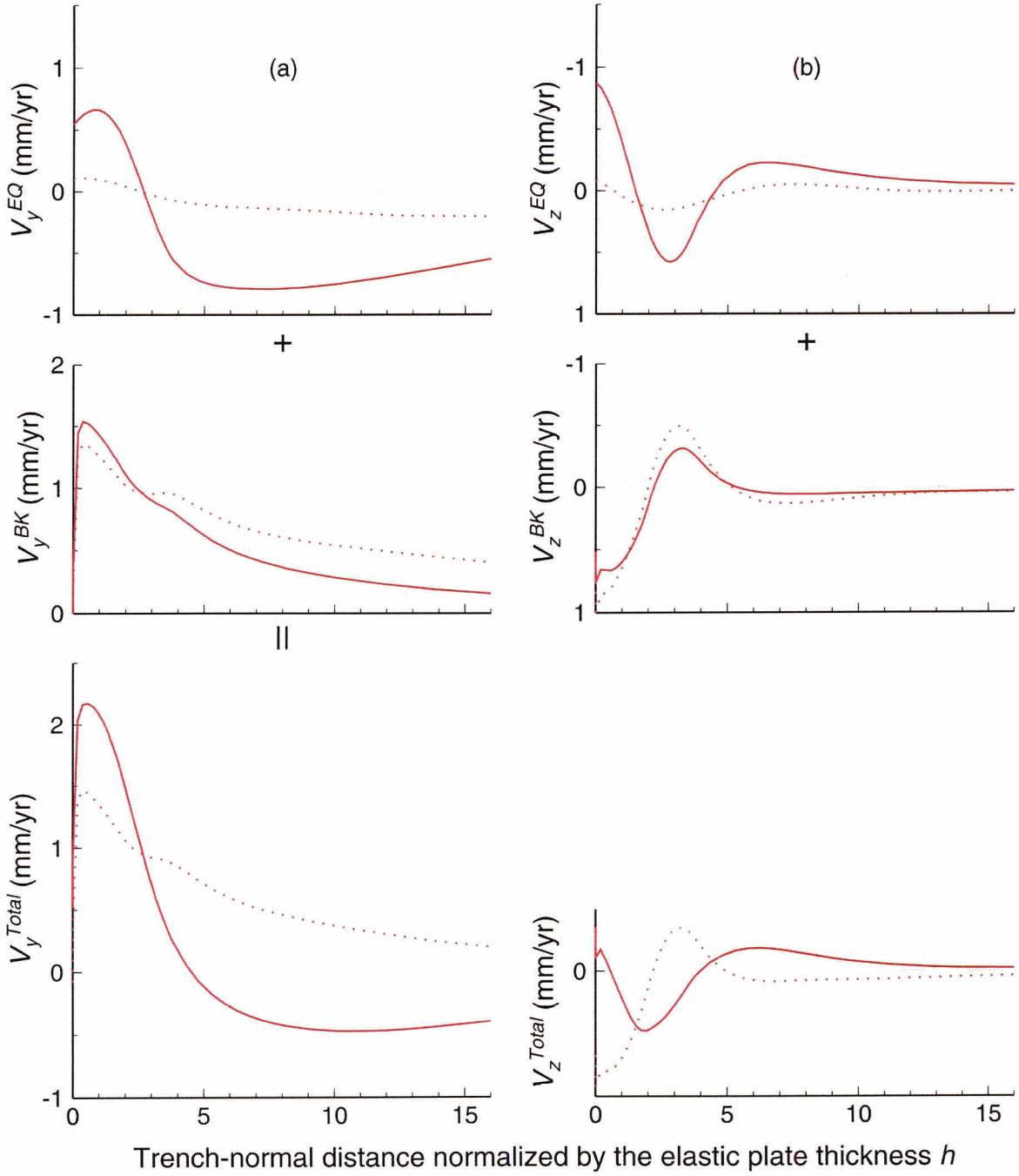

Figure 3.8. Surface velocities of the reference model. Horizontal velocities in response to earthquake alone, to fault locking alone, and to earthquake with subsequent fault locking are shown in the upper, middle, and bottom panel, respectively. Solid and dotted lines represents times of $5T_M$ and $25T_M$.

because the backslip rate along the fault is fixed.

Velocities in response to the earthquake as well as subsequent fault locking are obtained by combining V^{EQ} and V^{BK} (bottom panels of Figure 3.8). By comparing V^{EQ} and V^{BK} to V^{Total}, it is obvious that, crustal deformation (V^{Total}) is dominated by the earthquake component (V^{EQ}) at the early stage of the interseismic period, but by fault locking component (V^{BK}) at later stages. The reason is as follows. The coseismic slip induces a shear stress in the deep part of the fault and parts of the upper mantle. At the early stage of the interseismic period, the effect of stress relaxation induced by the coseismic slip dominates. At the later stage, the stresses induced by the coseismic slip are increasingly relaxed as discussed above. The effect of plate subduction then becomes dominant.

3.4.2. Single Versus Multiple Earthquake Cycles

Like periodically oscillating one end of a rope results in periodical deformation of the rope, kinematically prescribed cyclic fault slip results in cyclic crustal deformation. The crustal deformation at a given time depends on the fault slip and the stress field at that time. In the model, the fault slip pattern in any cycle is identical to that of the first cycle, but the stress field at the beginning of each cycle can be different. The pre-stress field at the beginning of the first cycle is assumed to be zero in the modelling. At the beginning of a later cycle, the stress perturbation resulting from previous cycles may not be zero unless the system is completely relaxed at the end of each cycle. However, we can expect similar crustal deformation in different earthquake cycles if residual stresses at the end of each cycle are small.

The reference model described in section 3.4.1 is used to obtain the results shown in Figure 3.9. The cycle length is $30T_M$, where T_M is the upper mantle Maxwell time. The main features of V_y and V_z in the 2nd and 4th cycle can be quite well represented by those of V_y and V_z in the 1st cycle. The small difference is because of the fact that stresses at the end of the first cycle are not completely relaxed. Therefore, deformation in later cycles can be approximated by the deformation in the first earthquake cycle. For simplicity, I only show the deformation pattern in the first earthquake cycle for later tests in this chapter unless otherwise specified.

3.4.3. Effects of Geometrical Parameters

In the preceding section, the time evolution of the deformation field in an earthquake cycle is studied given widths of the rupture and transition zones and fault dip. The present section is designed to study the sensitivity of the models to these geometrical parameters. The following models are simple variations of the reference model presented in section 3.4.1. All parameter values are as shown in Table 3.1, except the geometrical parameter to be tested.

First, the locked zone is fixed at $2h$ (h is the elastic plate thickness) as for the reference model. Figure 3.10 shows surface horizontal velocity in models with three different transition zone widths, $0h$, $2h$ and $4h$ (green, red, and blue lines, respectively). At $5T_M$, V^{EQ} (includes Vy^{EQ} and Vz^{EQ}, upper panel of Figure 3.10) is greatly affected by the width of the transition zone, but at $25T_M$, when the system is almost relaxed, V^{EQ} is almost the same for all three models. This reflects that the coseismic and short-term postseismic deformation is greatly affected by the transition zone width. Velocity in

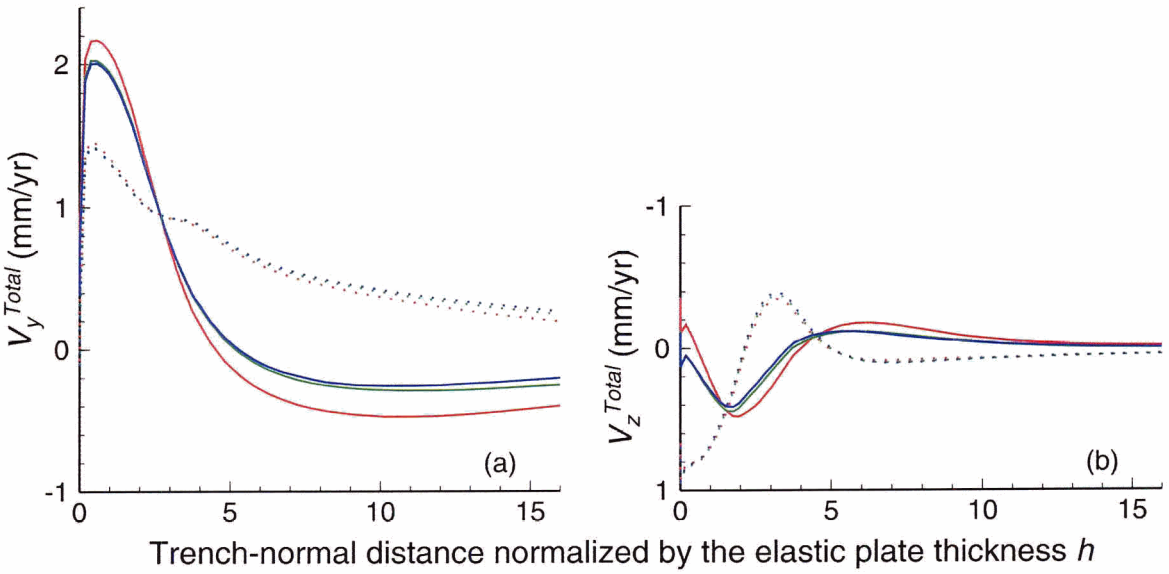

Figure 3.9. Surface velocities (mm/yr) in different cycles. Solid and dotted lines indicate $5T_M$ and $25T_M$ after an event, respectively. Red, green and blue lines represent the 1st, 2nd, and 4th cycle, respectively.

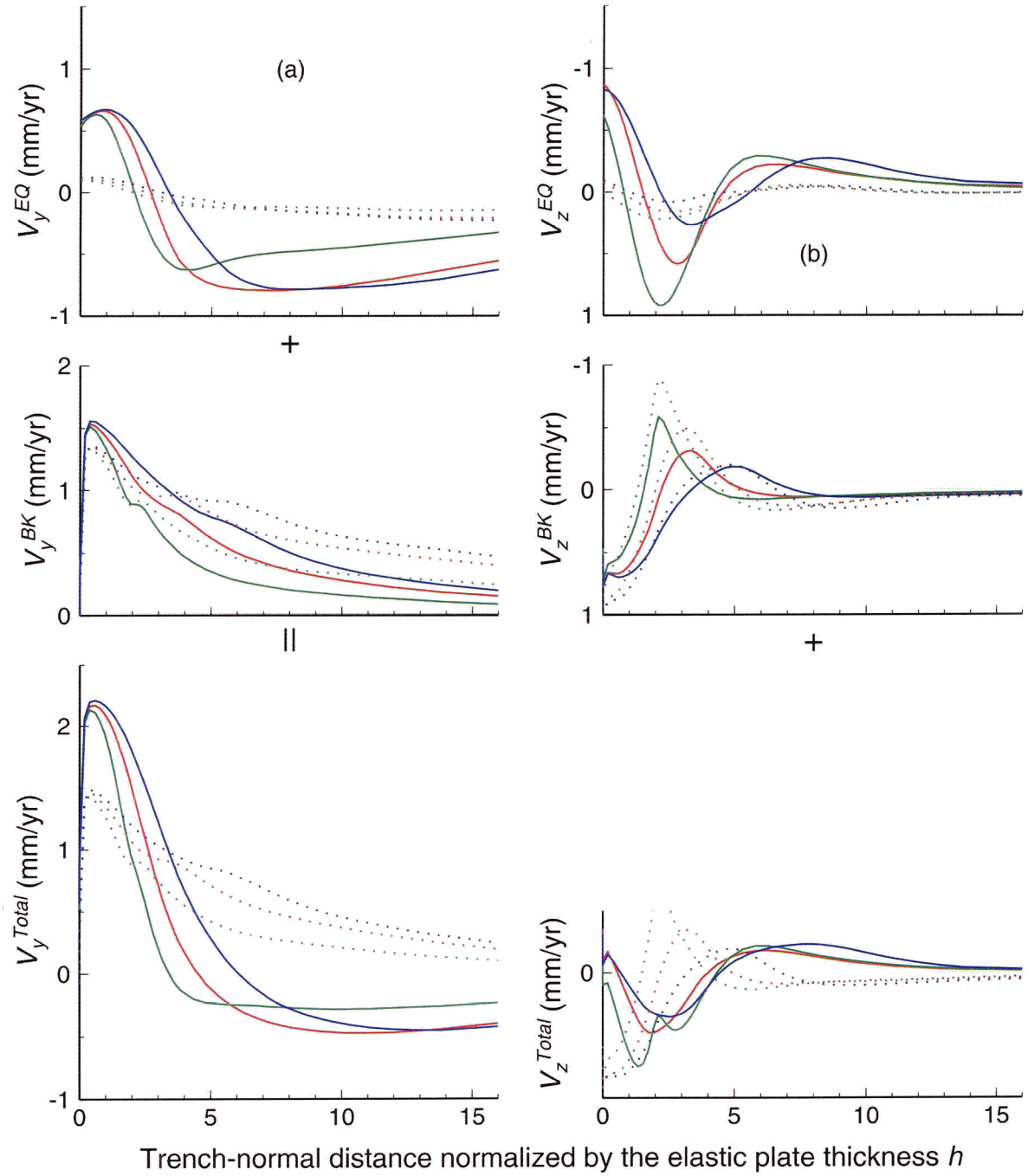

Figure 3.10. Surface horizontal velocities in models with the same locked zone width ($2h$) but different transition zone widths, $0h$ (green), $2h$ (red) and $4h$ (blue), where h is the thickness of the elastic upper plate. The width of the locked zone is $2h$. Solid and dotted lines indicate $5T_M$ and $25T_M$, respectively after the earthquake.

response to fault locking alone (V^{BK}) is systematically larger in models with wider transition zones, the mechanism of which is obvious.

For velocity in response to an earthquake with subsequent fault locking, high surface horizontal velocities (Vy^{Total}) extend farther landward for a wide transition zone (e.g., blue lines in bottom panel of Figure 3.10a). A wider transition zone affects a broader area. For vertical velocity profiles, the peak is sharper for a model with a narrower transition zone (Figure 3.10b). For the model with no transition zone, the peak positions of Vz^{EQ} and Vz^{BK} are both above the downdip edge of the locked zone, around $2h$, but with opposite directions. This results in a two-peak shape for Vz^{Total} (green curve in bottom panel of Figure 3.10b).

Models with different locked zone widths, $0h$, $2h$ and $4h$ are shown in Figure 3.11. The width of the transition zone is assumed to be $2h$ as in the reference model. It is obvious that a wider locked zone affects a wider area of the upper plate.

Surface velocities of models with different fault dips, 5°, 15° and 30° are shown in Figure 3.12. An interesting feature of Figure 3.12 is that Vy (V_y^{EQ} and V_y^{BK}) with the fault dip 15° is similar to V_y with the fault dip 30°, while V_z (V_z^{EQ} and V_z^{BK}) with the fault dip 15° is similar to V_z with the fault dip 5°. This reflects that the horizontal and vertical fault slip components do not vary equally with the fault dip.

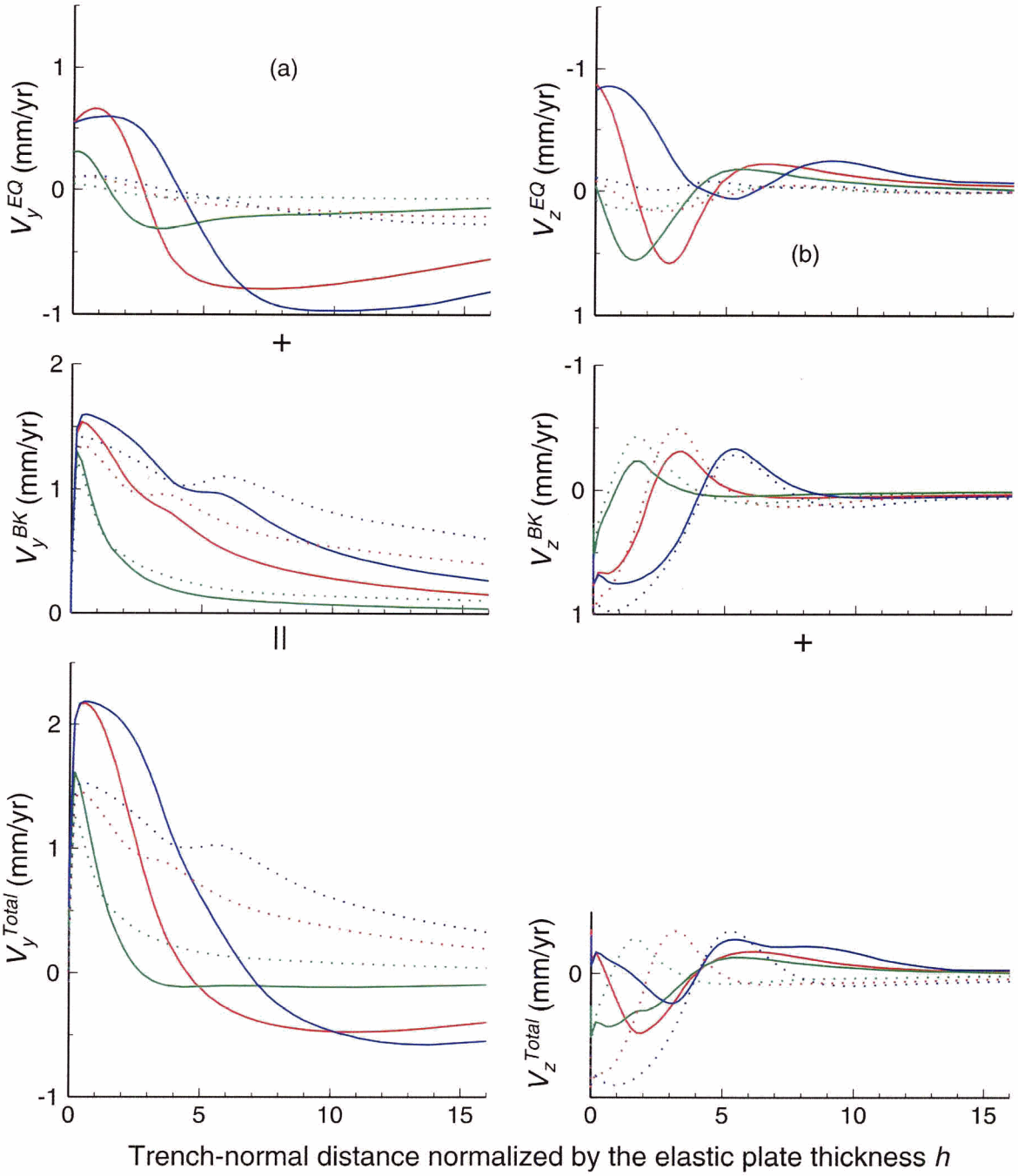

Figure 3.11. Surface displacements (m) of models with the same transition zone width but different locked zone widths. Solid and dotted lines indicate $5T_M$ and $25T_M$ after earthquake, respectively. Green, red and blue lines represent the locked zone widths of $0h$, $2h$ and $4h$, respectively. The transition width is assumed to be $2h$.

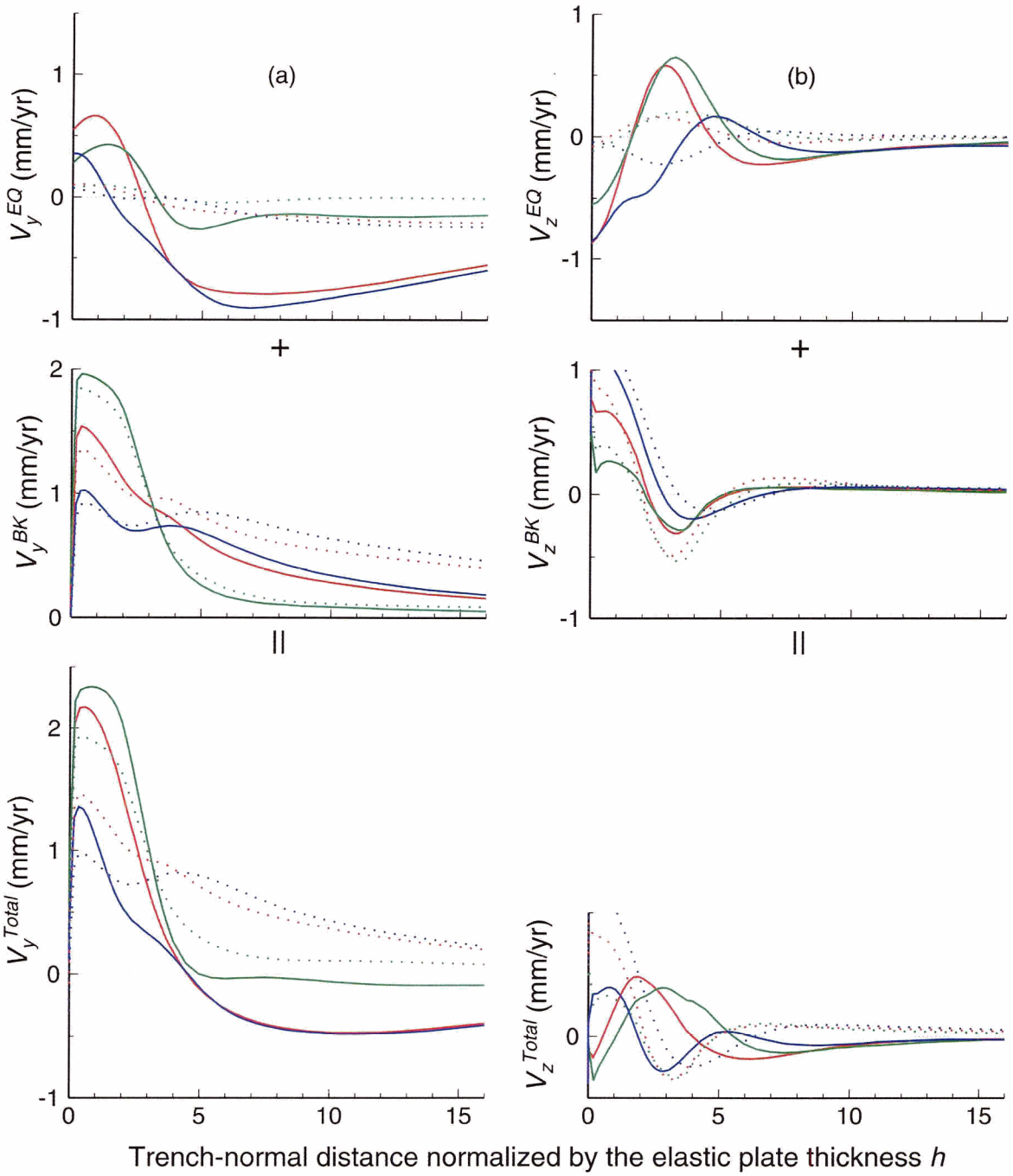

Figure 3.12. Surface velocities (mm/yr) of models with different fault dips. Solid and dotted lines represent times of $5T_M$ and $25T_M$, respectively. Green, red and blue lines represent models with fault dips of 5°, 15° and 30°, respectively.

Chapter 4. Applications to the Chile Subduction Zone

4.1. Tectonic Settings and the 1960 Great Earthquake

4.1.1. Tectonic Background

Figure 4.1 shows the tectonic settings of the western boundary of the South America plate. The Nazca plate that subducts beneath the South America plate is young and warm. The age of the subducting slab is greater than 30 Ma at central South America and becomes much younger to the south near Chile Ridge (Demets et al., 1990). Around latitude 47°S, the Chile Ridge subducts beneath the South America plate. South of the triple junction, the Antarctica plate subducts beneath the South America plate.

Demets et al. (1990) developed a global plate motion model NUVEL-1 that was constrained by spreading rates, transform fault azimuths, and earthquake slip vectors. Taking into account revisions to the geomagnetic reversal time scale, Demets et al. (1994) modified NUVEL-1 into a recalibrated global plate motion model NUVEL-1a. The average misfit is reduced from 6±1% of NUVEL-1 to < 2% of NUVEL-1a. NUVEL-1a predicts the subduction rate of the Nazca plate to be 80 mm/yr in a direction of N81°E at 32°S. However, Angermann et al. (1999) suggested a Nazca plate subduction rate of 66 mm/yr (directed N80°E) based on data from two GPS campaigns in 1994 and 1996 involving four sites on the Nazca plate and five sites defining a stable core of the South America plate. The campaign GPS data used in Angermann et al.'s model might not represent the long term motion because the four sites on the Nazca plate are near the

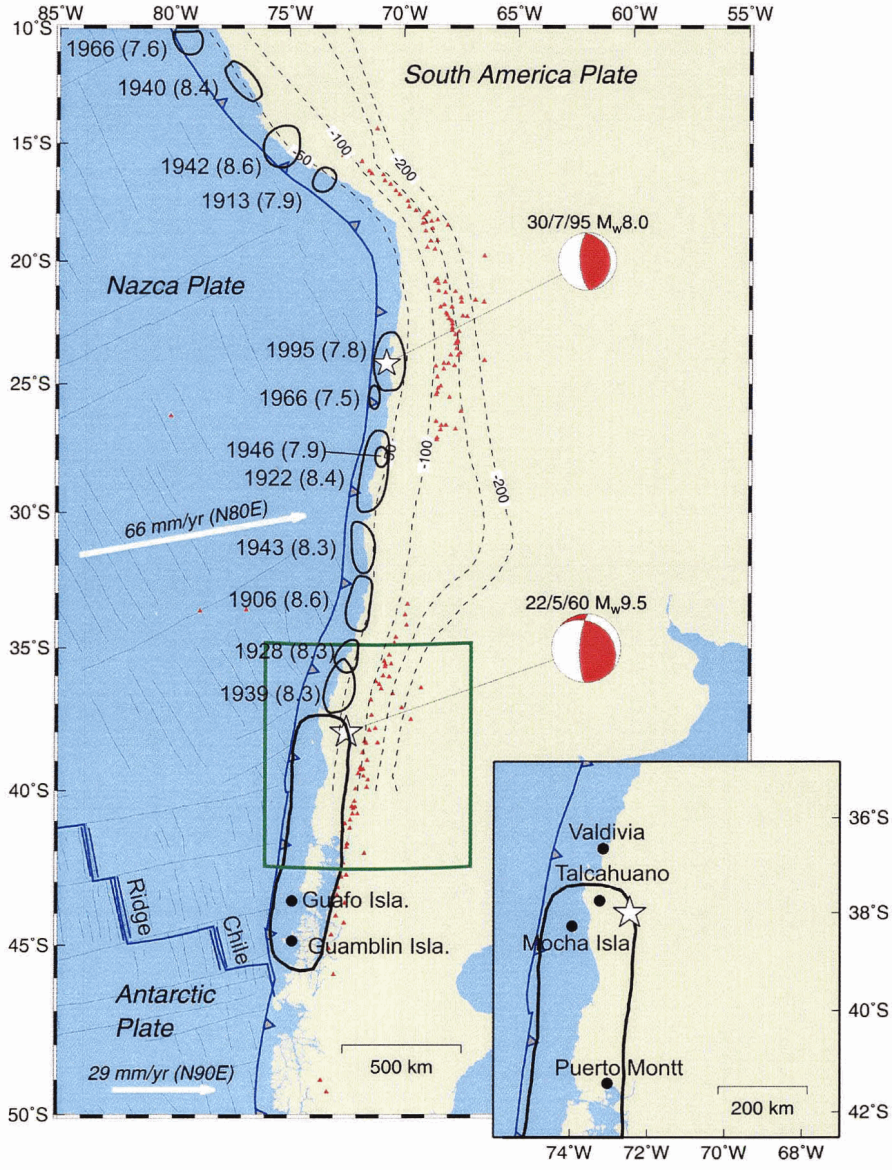

Figure 4.1. Tectonic setting of the Chile subduction zone. Rupture zones of earthquakes M > 7.5 over the past century (Kelleher, 1972; Klotz et al., 2001) are outlined with thick dark closed lines. White stars represent earthquakes Mw > 7.5 that occurred after 1960; the focal mechanisms of these two earthquakes are obtained from NEIC. The subducting slab is contoured using dashed lines (Klotz et al., 2001). Thick white arrows represent motion of the Nazca plate (Angermann et al., 1999) and Antarctic plate (Demets et al., 1994) relative to South America.

presently locked plate boundary and hence may be affected by internal elastic deformation of the oceanic plate. The subduction rate constrained by GPS campaigns may be lower because part of the total plate convergence may be consumed by such internal deformation. For this reason, the 66 mm/yr estimated by Angermann et al. (1999) may reflect "current" plate motion between the Nazca plate and the South America plate at a time scale of 10^2 years (see Table 1.2), and the 80 mm/yr estimated by Demets et al. (1994) may reflect long term, average plate motion at the geological time scale of $> 10^5$ years (see Table 1.2). However, the accuracy of GPS in 1994 and 1996 could also be lower than present because of the smaller number of satellites in the GPS constellation at that time. It is difficult to say which subduction rate better represents the current plate motion. The subduction rate of 66 mm/yr is arbitrarily used in a reference model of this work, but the rate of 80 mm/yr will also be tested.

4.1.2. Interplate Earthquakes and the 1960 Event

Large Mw > 7 interplate earthquakes repeatedly occur at the Chile subduction zone (Figure 4.2). The recurrence time for these large events varies from decades at 15°S to more than 100 years at 40°S (Kelleher, 1972; Nishenko, 1985). Large thrust events have ruptured almost every part of the western South America plate boundary over the past 100 years as shown in Figure 4.1.

The largest interplate earthquake ever recorded on earth occurred in this region on May 22nd, 1960. The great 1960 Chile earthquake and subsequent tsunami affected a disaster region populated by over 2.5 million people, claimed more than 2000 lives, and caused damage of 500 – 700 million U.S. dollars (Sievers et al., 1963; Housner, 1963).

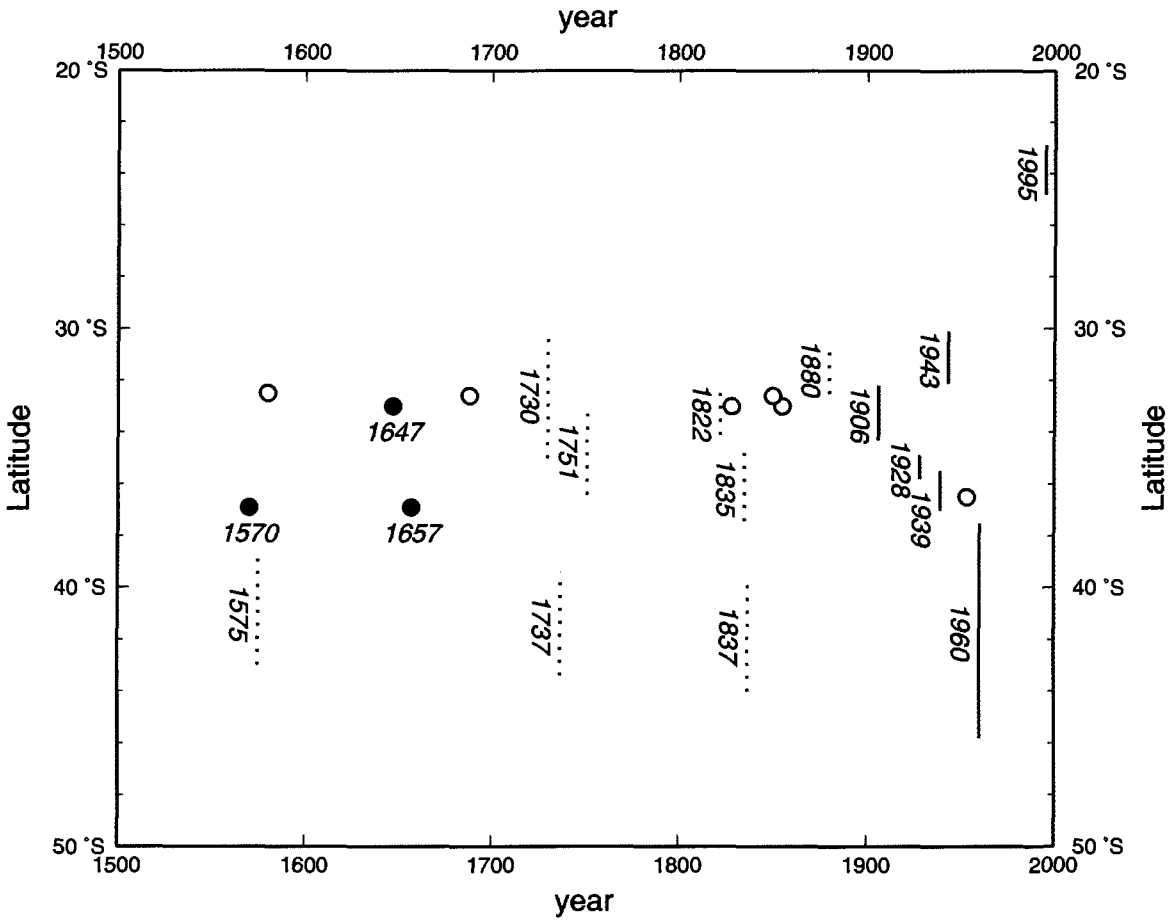

Figure 4.2. Space and time diagram of Chilean interplate earthquakes since 1550 between latitudes 30°S and 46°S (after Kelleher, 1972). All events except the 1995 event (Klotz et al., 1999) were summarized by Lomnitz (1970). Solid vertical lines represent the lateral extent of relatively well-determined rupture zones. Dashed lines indicate less reliable estimates based on descriptions by Lomnitz (1970). Circles represent events for which rupture zones are not constrained. Open circles represent 7.5 > M > 7 events. All other events are M 8 or larger.

Extreme shaking and seafloor deformation led to other natural hazards (tsunami, flood, landslide, etc.) (Duke and Leeds, 1963; Davis and Karzuloíc, 1963; Barrientos and Ward, 1990). The earthquake-induced tsunami propagated across the Pacific Ocean, and produced waves up to about 5 meters high along the Japanese coast (Satake et al., 2003). This great subduction zone earthquake was accompanied by a series of smaller events as shown in Table 4.1. The foreshocks started with an Ms = 8.3 event on May 21st with moment release 2.0×10^{21} Nm and included a total of nine large events (event 1-9 in Table 4.1) (Cifuentes, 1989). Cifuentes (1989) estimated the rupture length of the mainshock consisting of two sub-events (A and B in Table 4.1) to be 920 ± 100 km. Kanamori and Cipar (1974) estimated a seismic moment of 2.7×10^{23} Nm for the mainshock by matching the amplitude of synthetic seismograms with the observed ones. Based on complex amplitude measurements of low-frequency (1.0-5.0 mHz) normal model data, a line source propagating at a constant rupture velocity was used to obtain a source model consisting of three events (Cifuentes and Silver, 1989). These events include an event before the mainshock with 1150 s duration and moment 1.9×10^{23} N m, a mainshock with moment 3.2×20^{23} N m, and an event after the mainshock with 350 s duration and moment 0.4×10^{23} Nm. The total moment magnitude Mw of the 1960 events is 9.5 (Kanamori, 1977).

The 1960 Chile earthquake rupture propagated along strike by about 900 km southward from the hypocentre and a short distance northward (Figure 4.1). Coseismic landlevel changes range from 5.7 meters of uplift on the mainland coast and three offshore islands (Mocha, Guafo, and Guamblin) to 2.7 meters of subsidence near Valdivia (Plafker and Savage, 1970). Plafker (1972) deduced a rupture zone 120 km

Table 4.1. Foreshock sequence (Event 1-9) and initiation of the great 1960 Chile main shock (Event A and B) (from Cifuentes, 1989; Duda, 1963).

Event	Origin	ISS		Relocated		M_s
	Time, UT	Latitude (S)	Longitude (W)	Latitude (S)	Longitude (W)	
			May 21, 1960			
1	1002:52	37.57	73.07	37.17	72.96	8.3
2	1053:53	37.49	73.03	37.31	72.72	7.3
3	1300:06	37.30	72.93	37.07	72.74	6.5
			May 22, 1960			
4	0601:35	38.15	73.97	37.65	72.84	8.3
5	0810:54	37.81	72.63	37.22	72.51	5.8
6	1030:39	37.84	72.86	37.52	72.67	6.5
7	1032:42	37.68	72.67	37.52	72.35	7.3
8	1216:44	38.24	73.20	37.68	72.61	6.3
9	1855:57	38.06	72.74	37.79	72.49	7.8
A	1910:40	38.05	72.19	38.05	72.34	
B	1911:14	38.17	72.57	38.16	72.20	

wide and 1000 km long dipping 20° with 20 m of slip by analysing static deformation data and teleseismic surface waves. Barrientos and Ward (1990) developed an inversion model to infer coseismic fault slip distribution from surface deformation data including sea-level change, elevation difference, and horizontal strain. In their spatially variable fault slip model, the coseismic slip along the fault varies from 0 to 40 m. If the slip was assumed to be uniform along a rectangular fault of 850 km long, 130 km wide, and 20° dip, they obtained an average slip of 17 meters.

4.2. GPS Observations Along the Andean Margin

Over the past decade, the Andean subduction zone has been studied using the GPS technique. Norabuena et al. (1998) published crustal velocity values in Peru and Bolivia based on GPS measurements. Bevis et al. (1999) reported values for 12 GPS sites mainly in the Chilean forearc area north of 22°S. Klotz et al. (1999) showed that the present-day crustal deformation between latitudes 22°S and 26°S was strongly affected by the 1995 Antofagasta earthquake.

Starting in 1993, the GeoForschungsZentrum (GFZ) Potsdam, Germany, within the framework of South American Geodynamic Activities (SAGA) project and in cooperation with numerous local host organizations, established a large-scale GPS campaign network in Chile and western Argentina. In 2001, Klotz et al. published velocities at more than 200 GPS campaign sites in an area of about 2500 km long along the margin (from 22°S to 44°S) and 800 km wide (Figure 4.3). The data presented by Klotz et al. (2001) were based on GPS campaigns conducted in 1995 and 1996 in a section from 22°S to 26°S and in 1994 and 1996 in a section from 26°S to 44°S. GPS data from 17°S to 22°S in Figure 4.3 were obtained from Khazaradze (2001, personal communication). During each campaign, each site was occupied for at least three consecutive days with daily observation periods of more than 20 hours. All the campaign data, together with data from selected International GPS Service (IGS) sites and the GFZ South American permanent GPS stations, were processed using GFZ software EPOS.

Klotz et al. (2001) processed the GFZ GPS campaign data in three steps. (1) All the data were processed using the combined IGS satellite orbits and the Earth orientation parameters to obtain fiducial-free station coordinates. (2) The processed solution was

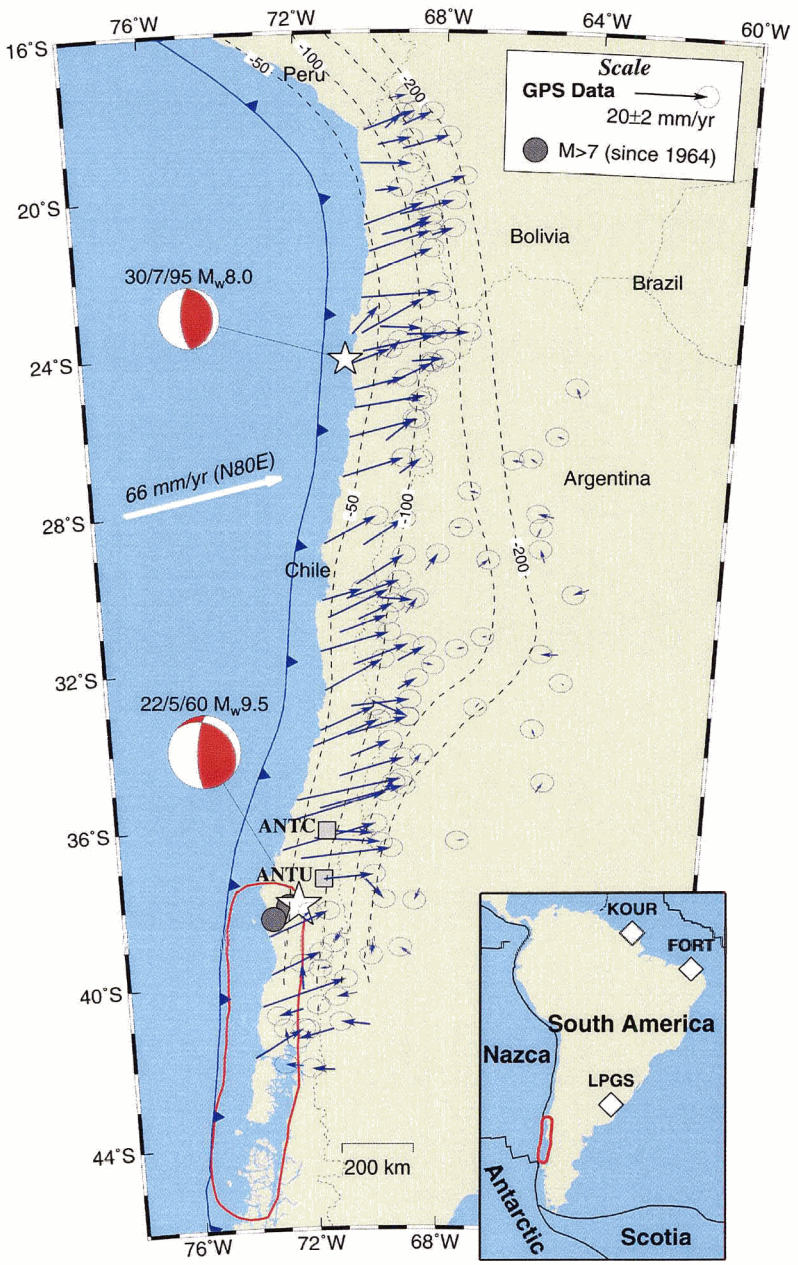

Figure 4.3. GPS velocities along the Chile margin (Klotz et al., 2001; Khazaradze et al., 2002). Velocity at station ANTC was reported by Kendrick et al. (1999). Red thick line outlines the rupture zone of the 1960 Mw 9.5 earthquake (Plafker, 1972). The epicentres of the 1995 $M_w = 8.0$ (Delouis et al., 1998) and 1960 $M_w = 9.5$ (Cifuentes, 1989) earthquakes are shown as white stars. Thin black contour lines represent the depth of the subducting slab. Filled circles show the only two earthquakes with M > 7 that occurred in the past 30 years in this region.

transformed into the International Terrestrial Reference Frame (ITRF97). (3) The ITRF97 solution was then transformed into a regional reference frame. The regional reference frame is fixed to a nominal "stable" South America that is defined using IGS stations KOUR, FORT, and LPGS (Figure 4.3, inset). No other constraints were imposed. Because of the large formal error estimates for the vertical components (Jordan et al., 1997), the vertical GPS data published by Klotz et al. (2001) do not have the sufficient resolution to reveal the vertical tectonic signal. Therefore, only the horizontal GPS velocities (Figure 4.3) are used in this work. In 1995, an earthquake of Mw 8.0 occurred at Antofagasta as shown in Figure 4.4 (Khazaradze, 2001, personal communication). The coseismic and postseismic crustal deformation of the 1995 event was modelled by Klotz et al. (2001) and subtracted from the GPS observations to yield the surface velocities in Figure 4.3.

The most prominent feature of the GPS observations in Figure 4.3 is that all the coastal sites are moving landward. This indicates that the thrust interface between the subducting oceanic Nazca plate and the overriding continental South America plate is currently locked. Using a 3-D dislocation model, Klotz et al. (2001) estimated that the depth of the downdip limit of the locked zone varies along strike: It is about 33 km deep North of 30°S, but reaches 50 km depth south of 35°S. An interesting feature is that from 38°S to 42°S, a contiguous group of inland sites about 200-400 km from the trench are moving seaward in a reverse direction. Klotz et al. (2001) qualitatively attributed this deformation pattern to postseismic relaxation effects of the 1960 Mw 9.5 Chile earthquake.

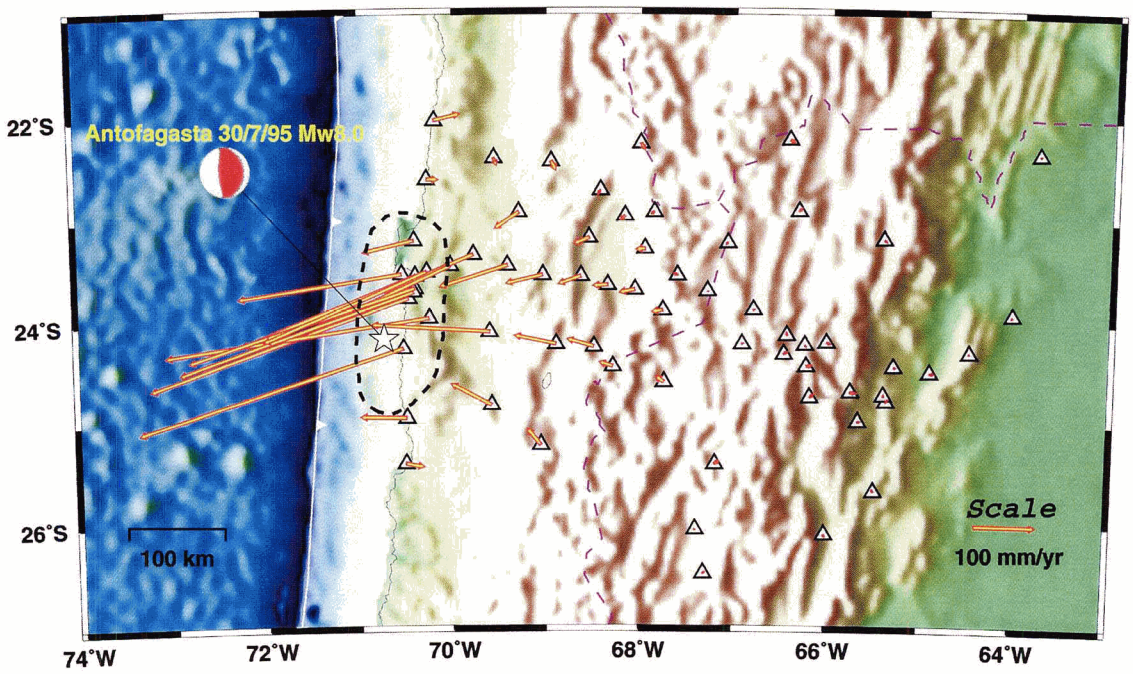

Figure 4.4. Coseismic displacements of the 1995 Mw 8.0 Antofagasta earthquake at GPS sites (Klotz et al., 1999). Dashed dark line outlines the rupture zone of the 1995 earthquake. Figure is provided by Khazaradze (2001, personal communication).

4.3. Processes Responsible for the Seaward Motion of Inland Sites

The above-mentioned seaward motion of inland sites 200-400 km from the trench cannot be an artifact for the following reasons. (1) It cannot be due to an error in the reference frame because all the GPS data in Figure 4.3 were processed using the same procedure and referenced to the same nominal stable South America plate. (2) It cannot be due to random errors because a contiguous subset of stations shows the same seaward deformation. (3) The coherent pattern of seaward motion occurs only landward of the rupture region of the great 1960 Mw 9.5 earthquake, suggesting a causal link. Seaward motion of inland sites landward of a great earthquake rupture area is not unique to this margin. Similar seaward crustal motion was reported at the Alaska subduction zone about 300-400 km from the trench (Freymueller et al., 2000; Savage et al., 1999). The seaward motion at Alaska spatially correlates to the rupture region of the great 1964 Mw 9.2 earthquake (Figure 4.5).

Small earthquakes cannot induce seaward coseismic slip in such a broad inland area 200-400 km from the trench, and no events of $M > 7$ have been recorded in this region since 1975. Around the rupture zone and very shortly after the earthquake, it is usually difficult to distinguish between contributions to postseismic deformation from fault afterslip and mantle relaxation (Pollitz et al., 1998). For the mechanisms of the seaward motion, we are led to three hypotheses: (1) Aseismic afterslip along the downdip extension of the thrust fault may have induced the seaward crustal deformation. (2) Interseismic silent slip events occurred during the three GPS campaign periods. (3) The

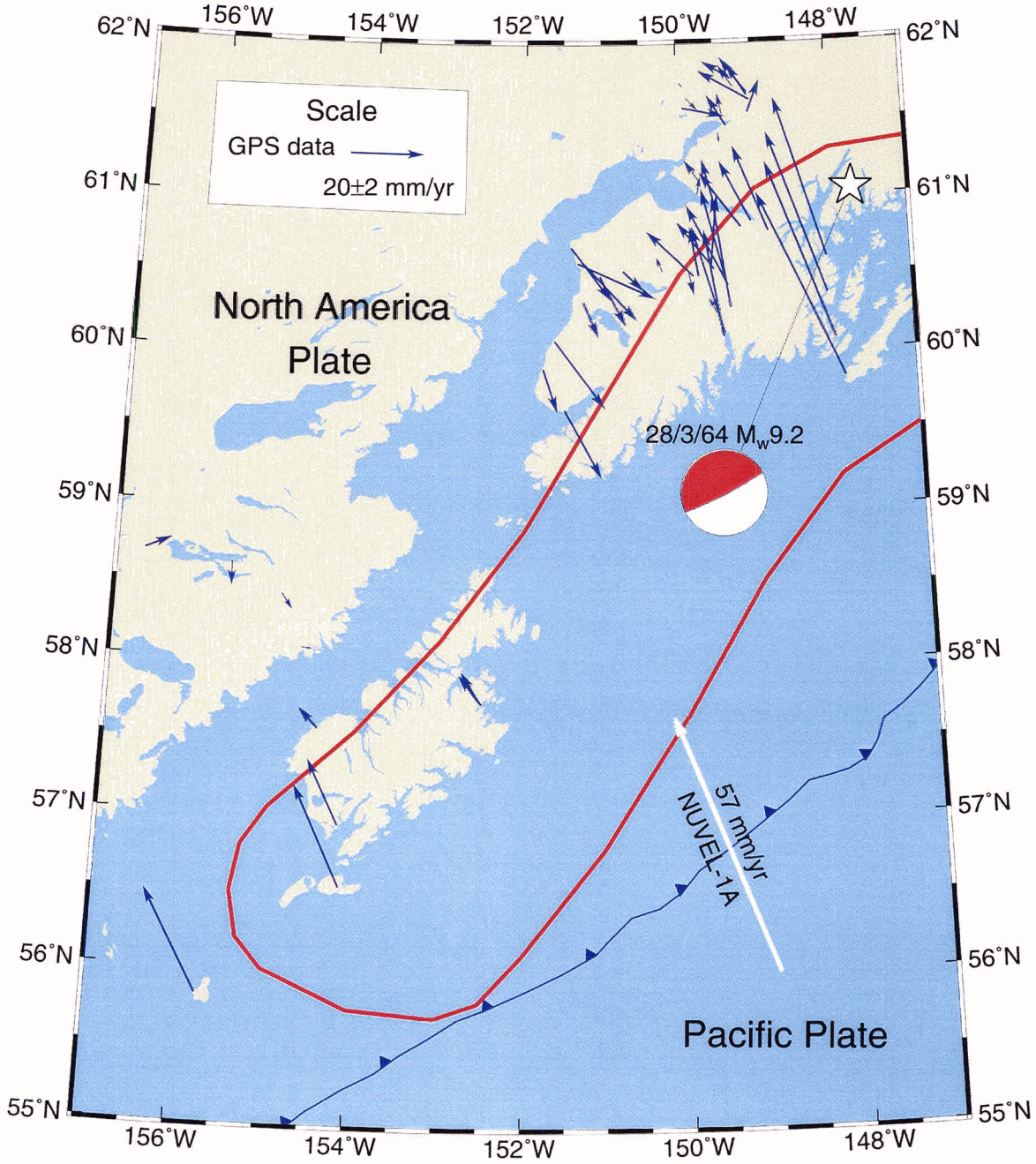

Figure 4.5. Horizontal GPS velocities relative to North America at the Alaska subduction zone (Freymueller et al., 2000). Red thick line outlines the area of geodetically measured coseismic crustal uplift and subsidence associated with the 1964 Alaska earthquake. Plate convergence vector is according to Demets et al. (1994). The epicentre of 1964 M_w = 9.2 (Doser et al., 1999) earthquakes is shown as a while star.

seaward motion of inland sites may be controlled by postseismic relaxation of upper-mantle stress induced by the great 1960 Chile earthquake. These hypotheses will be discussed in this section.

4.3.1. Aseismic Afterslip

An interplate great earthquake may induce aseismic afterslip along the downdip extension of the thrust fault that may continue for years after the event. Zweck et al. (2002a, 2002b) attributed the present-day seaward motion of inland GPS sites at the Alaska subduction zone (Figure 4.5) to postseismic fault slip beneath and north of the western Kenai Peninsula. Based on tide gauge data at the Chile subduction zone, Barrientos et al. (1992) used an analytical elastic solution to model aseismic afterslip over a downdip extension of the fault. In their model, an afterslip of 4 m over an 84-km wide portion of the fault with the upward-end point at 50 km depth provided the best fit to tide gauge observations.

In some cases, the rupture zone itself may not be locked immediately after the event, which means aseismic afterslip over parts of the rupture zone. For example, Heki and Tamura (1997) reported aseismic slip of the rupture zone after the Sanriku – Oki, Japan, earthquake of December 28th, 1994. Using continuous GPS date, they inferred an aseismic fault slip with a moment release comparable to that of the coseismic slip. In this thesis, the term "aseismic afterslip" refers to aseismic fault slip along the downdip extension of a thrust fault over years to decades after an event.

Using a 3-D model of dislocation in a uniform elastic half space (Okada, 1985, 1992, see section 2.2.2), I have conducted simple tests to evaluate the mechanism of aseismic

afterslip at the Chile subduction zone. A simplified model as shown in Figure 4.6 is used. The model consists of a locked zone and a downdip afterslip zone. Both the locked zone and the afterslip zone are assumed to have uniform slips. The GPS-observed seaward motion of inland area at the Chile subduction zone is about 200 – 400 km from the trench (Figure 4.3). If the seaward motion of inland GPS sites is due to aseismic afterslip, the slip cannot occur over the rupture zone of the 1960 Chile earthquake, but must be at a greater depth.

Based on plate geometry models in previously published papers (e.g., Klotz et al., 2001; Barrientos and Ward, 1990; Plafker, 1972), the locked zone is approximated by a 160 km downdip width and continuously steepens at a dip of 20°. The locked zone is extended along the entire margin, i.e., well beyond the 1960 rupture zone (Figure 4.6). The locking of the fault is modelled as a backslip of 66 mm/yr over the locked zone. The along-strike length of the afterslip zone is assumed to be 900 km, just landward of the 1960 rupture region. Following Barrientos et al.'s model (1992), I assume that the dip of the afterslip zone is 30°, and the depth of its upward edge is 55 km. The width of the afterslip zone and the afterslip rate will be varied to fit the GPS data. A Poisson's ratio of 0.25 is assumed in the model.

The modelling includes three steps: (1) The crustal deformation purely in response to fault locking over the locked zone is calculated using the Okada model (1985). (2) The crustal deformation purely in response to the aseismic slip of the afterslip zone is modelled using the Okada model (1985, 1992). (3) Model results in response to fault locking and aseismic afterslip are obtained by linearly combining the results of (1) and (2).

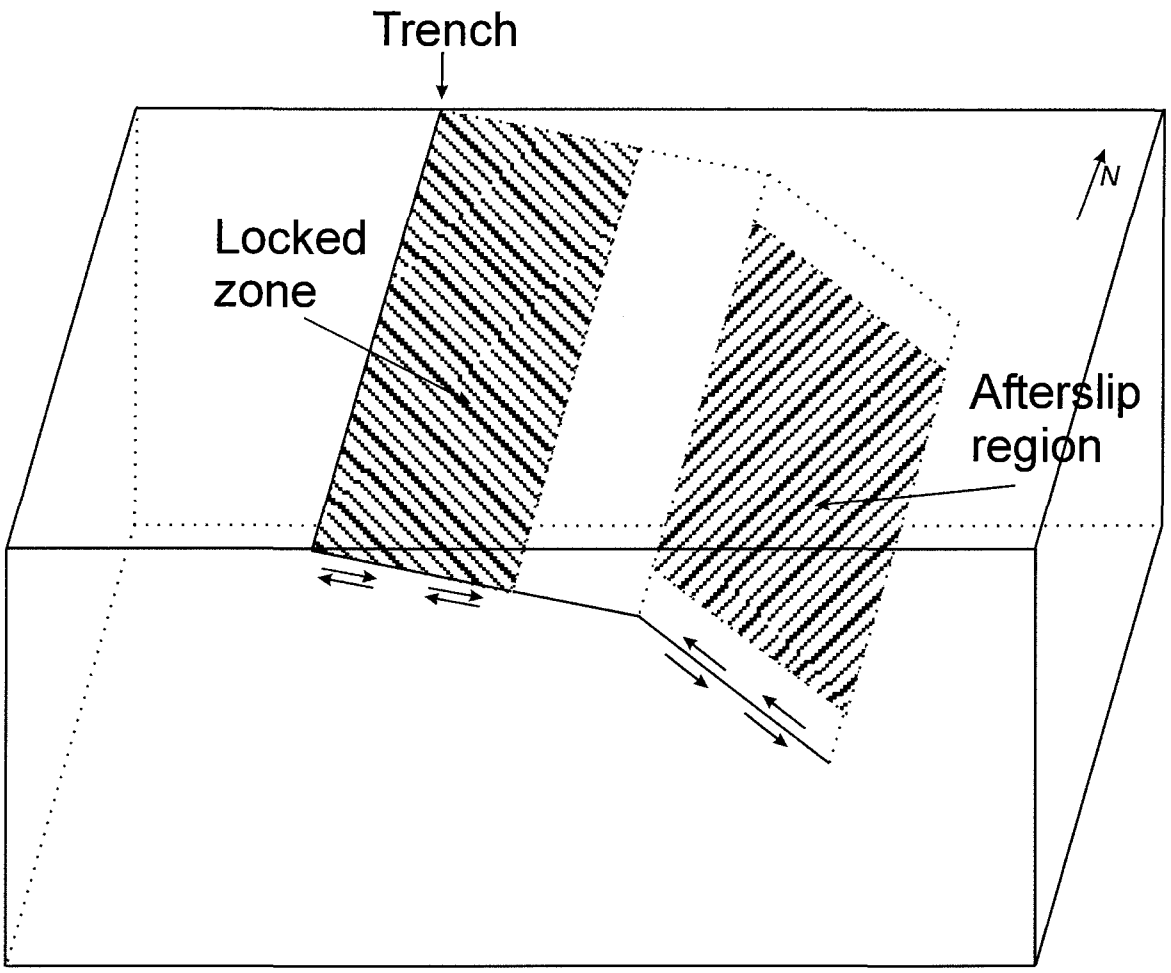

Figure 4.6. Conceptual representation of the model used to evaluate the afterslip mechanism for the seaward motion of inland GPS sites. Area shaded with backward dark lines represents the locked zone. Area shaded with forward dark lines represents the afterslip region.

The 3-D Okada elastic model uses a Cartesian reference frame and has a flat surface, but the GPS campaign data are on the surface of a spherical earth. In order to compare data and model results, the coordinates of the GPS data are mapped into a Cartesian reference frame through two steps. The spherical coordinates are mapped into a Cartesian reference frame X'O'Y' as shown in Figure 4.7 using Lambert Conformal Conical projection. Then the Cartesian reference frame X'O'Y' is shifted and rotated to the modelling reference frame XOY. The origin of the reference frame XOY is at the intersection point of the trench parallel line and the line of symmetry of the rupture zone. The x-axis is northward positive in the strike direction at N3.2°E. The y-axis is landward positive. The z-axis is downward positive.

Test 1: Assuming a downdip width of the afterslip zone 150 km (Test 1 in Table 4.2), an afterslip rate 90 mm/yr is found to fit the inland GPS observations (Figure 4.8a). The fit in the coastal area 100 – 200 km from the trench is rather poor. Increasing the afterslip rate leads to a better fit in the inland area 200 – 400 km from the trench but a poorer fit in the coastal area. Decreasing the afterslip rate leads to a better fit in the coastal area, but a poorer fit in the inland area. Different dips and depths of updip edge of the afterslip zone

Table 4.2. Parameters for modelling afterslip events. A locked zone of 160 km wide and 20° dip is used in modelling. The along-strike length of the locked zone is assumed to be extended along all the margin. The backslip over the locked zone is assumed to be 66 mm/yr in the direction of N80°E.

	Afterslip region				Afterslip	
	Length (km)	Width (km)	Dip (°)	Depth of the updip end point (km)	Afterslip rate (mm/yr)	Afterslip angle (°)
Test 1	900	150	30	55	90	80
Test 2	900	100	30	55	120	80

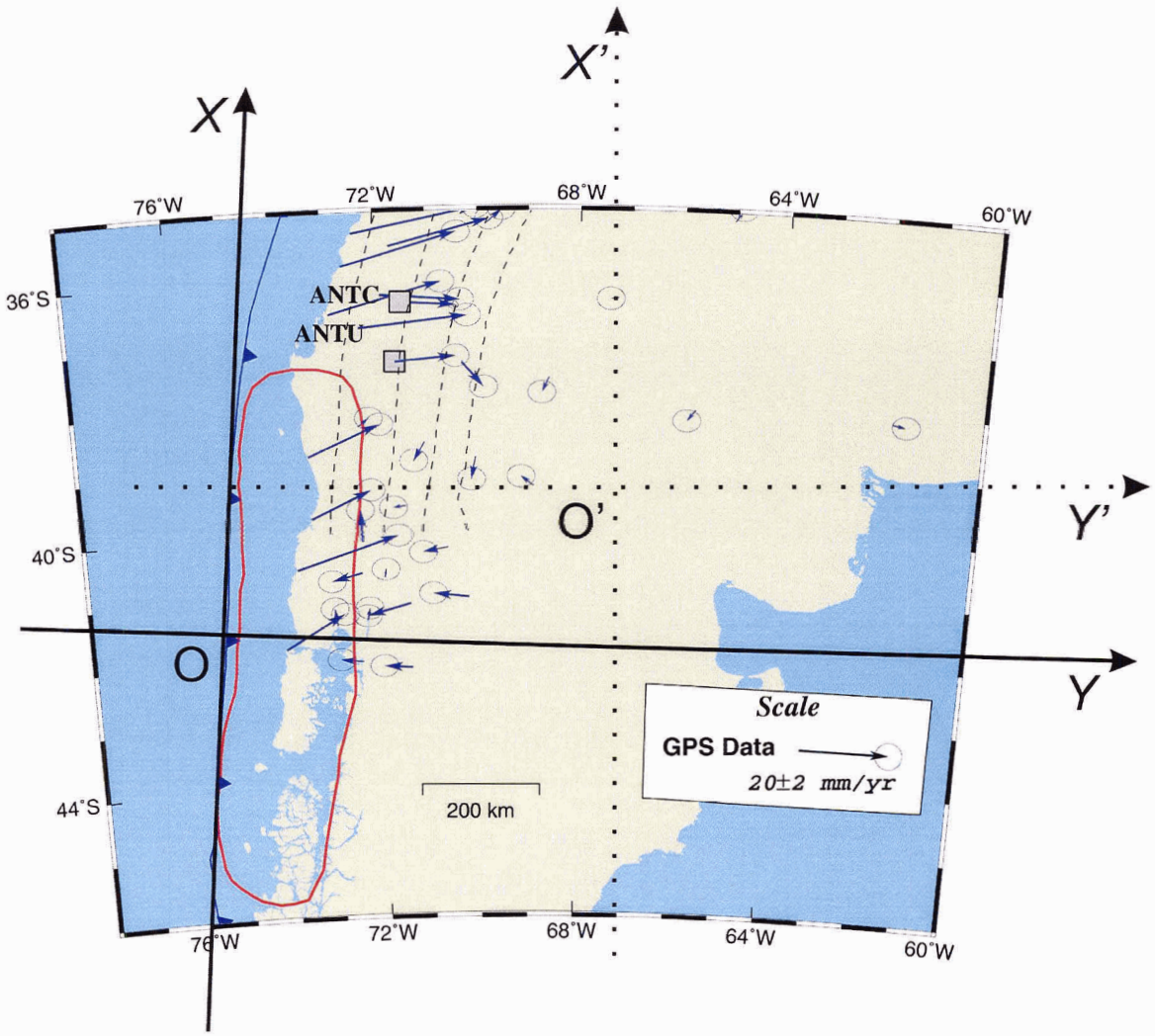

Figure 4.7. The reference frames used to map the spherical coordinates of the GPS observations into a Cartesian reference frame. First, the spherical coordinates are mapped into a Cartesian reference frame X'O'Y' using Lambert Conformal Conical projection. Then the coordinates in X'O'Y' are shifted and rotated into a Cartesian reference frame XOY for comparison with afterslip models.

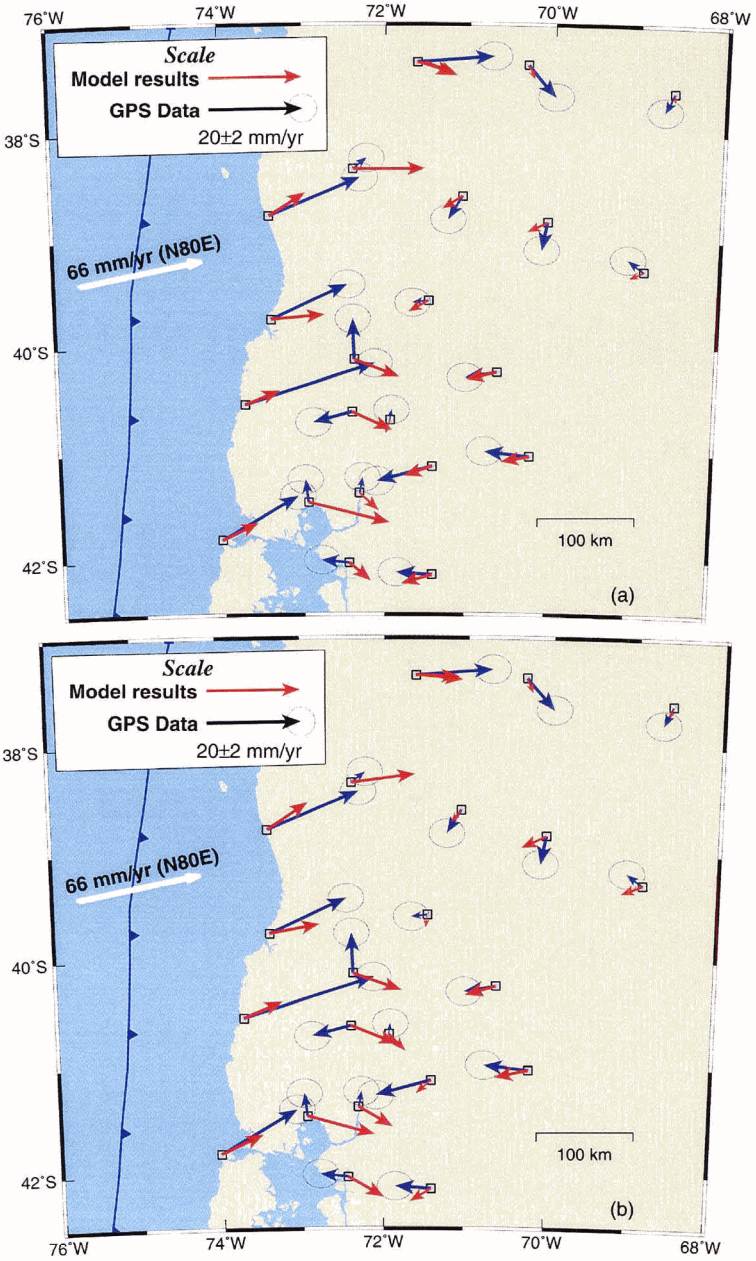

Figure 4.8. Comparison of the results of aseismic afterslip model with GPS observations. (a) Model parameters of Test 1 in Table 4.2 are used in the modelling. The downdip width of the afterslip region is 150 km. An afterslip rate 90 mm/yr is found to best fit the inland GPS observations. (b) Model parameters of Test 2 in Table 4.2 are used in the modelling. A downdip width of the afterslip region 100 km is assumed in this test. An afterslip rate 120 mm/yr best fits the inland GPS observations. Both models fail to fit coastal GPS data.

are tested, but these tests give a very poor fit to the observations. The results of these tests are not shown.

A fast afterslip rate 90 mm/yr 35 years after the earthquake is not impossible but highly unlikely. With a 150 km downdip width, the downdip edge of the afterslip zone is about 130 km deep. The plate interface may not behave like a fault because of the high temperature. Therefore, in addition to being unable to fit both coastal and inland GPS data simultaneously, Test 1 presents an unlikely physical mechanism.

Test 2: If the width of the afterslip zone is 100 km (Test 2 in Table 4.2), an afterslip rate 120 mm/yr is needed to fit the GPS observations (Figure 4.8b). The fit is still poor. If the width of the afterslip zone is varied from 150 km to 100 km, a larger afterslip rate of 120 mm/yr is required to better match the GPS observations 200 – 400 km from the trench. However, the poor fit in the coast area does not improve. The dip and depth of updip edge of the afterslip zone are varied by up to 50% to test the effects of these parameters, but these tests give a rather poor fit to the data (results are not shown).

A larger width of the afterslip zone requires a smaller aseismic afterslip rate to match the seaward motion of the inland area, but this leads to a poor fit in the coastal area. Decreasing the aseismic afterslip rate results in a better fit in the coastal area but a worse fit in the inland area. No reasonable geometry of the afterslip zone and the afterslip rate can be found to match the overall pattern of the GPS observations in both areas. Therefore, simple aseismic afterslip is unlikely a dominant mechanism for the seaward motion of the inland area.

4.3.2. Interseismic Silent Slip

Dragert et al. (2001) reported a silent aseismic slip event on the plate interface of the Cascadia subduction zone in 1999. A cluster of seven continuously monitoring GPS stations about 100 to 250 km from the trench were observed to briefly reverse their direction of motion. Total horizontal displacements at individual sites, estimated from regression, ranged from 2 to 4 mm in a time span of 6 to 15 days. Using a 3-D elastic model, Dragert et al. (2001) attributed this reversal to about 2 cm of aseismic silent slip over a 50-km-300km area on the subduction interface downdip from the seismogenic zone. The depth of the silent slip zone ranged from ~30 km to ~40 km. Similar transient slip events have been reported for other subduction zones (Lowery et. al., 2001; Ozawa et al., 2001; Heki et al., 1997). Rogers and Dragert (2003) observed repeated slow slip events with unique nonearthquake seismic signatures in the Cascadia subduction zone. Tremor-like seismic signals were found to correlate temporally and spatially with the slip events.

In this work, the area of the seaward motion is farther away from the trench (200 to 400 km) than that reported by Dragert et al. (2001) for Cascadia. If the motion was due to a silent slip on the plate interface of the Chile subduction zone, it had to be a coincidence of the following attributes. (1) The slip had to take place in the 50 to 150 km depth range. (2) The transient motion occurred during or around the time of the 1994 and 1996 GPS campaign surveys. (3) The transient motion took place only landward of the 1960 earthquake rupture zone. Nevertheless, the possibility of a transient slip cannot be completely ruled out. The motion direction of these sites in the next few years will support or invalidate this mechanism.

4.3.3. Mantle Stress Relaxation

Coseismic slip induces shear stress at the deeper part of the fault and in the upper mantle. As explained in section 3.3, the stress will relax over a time depending on viscosity. The relaxation will lead to delayed response to the earthquake in the inland area of the overriding continental plate. Very large earthquakes, such as the 1960 great Chile earthquake, may induce large stress in the mantle over a very broad region, and the relaxation of this stress may cause prolonged crustal deformation far away from the coseismic rupture zone that can be distinguished from afterslips. Only two subduction earthquakes (1960 Chile, 1964 Alaska) recorded in the past century have moment magnitude above 9 and rupture zones over 900 km long, and in both cases, seaward crustal motion has been observed landward of the rupture region several decades after the events (see section 4.2). In a 3-D viscoelastic finite element model of Cascadia great subduction earthquake cycles, Wang et al. (2001) found a seaward motion of inland sites 50 years after the 1700 great earthquake that was also estimated to be Mw ~9 (Satake et al., 2003).

Mantle relaxation is our preferred mechanism. We have published some preliminary results of a 3-D viscoelastic finite element model to explain the GPS observations (Khazaradze et al., 2002). This thesis presents a more detailed study to demonstrate the mechanism of mantle stress relaxation and to constrain the mantle viscosity at the Chile margin.

4.4. Finite Element Model Construction

4.4.1. Geometrical Parameters

Finite element models that include the heterogeneity of the real earth in great detail may produce a good fit to crustal deformation observations. However, the purpose of this work is to study the first-order pattern of the Earth's response to great subduction events, and the details of the earth heterogeneity are ignored. Simplifications allow us to focus on the essential aspects of the fundamental physical process. A 3-D model as schematically shown in Figure 4.9 is used in this study. The model consists of an elastic upper plate, and elastic slab and a viscoelastic upper mantle. The material is assumed to be uniform within each of these tectonic units. The x-axis is northward positive in the strike direction (N3.2°E). The y-axis is landward positive normal to the trench. The z-axis is downward positive.

In this work, the elastic over-riding plate includes the crust and the lithospheric mantle. Based on seismic evidence, the thickness of the continental crust ranges from about 10 to 50 km, and the thickness of the oceanic crust is less than 10 km (Tarling, 1981). The effective elastic thickness of old continental lithosphere is estimated to be 35-40 km (Burov and Diament, 1995). The elastic thickness may not be uniform. The elastic thickness of a stable craton is likely to be greater. In this work, the thickness of the elastic continental upper plate is assumed to be 40 km. However, a thickness of 30 km for the upper plate will also be tested. The thickness of the elastic oceanic plate (including the subducting slab) is assumed to be 30km.

The shape of the subducting slab is obtained through two steps. (1) A generalized 2-D slab shape based on previously published papers is compiled. Klotz et al. (2001)

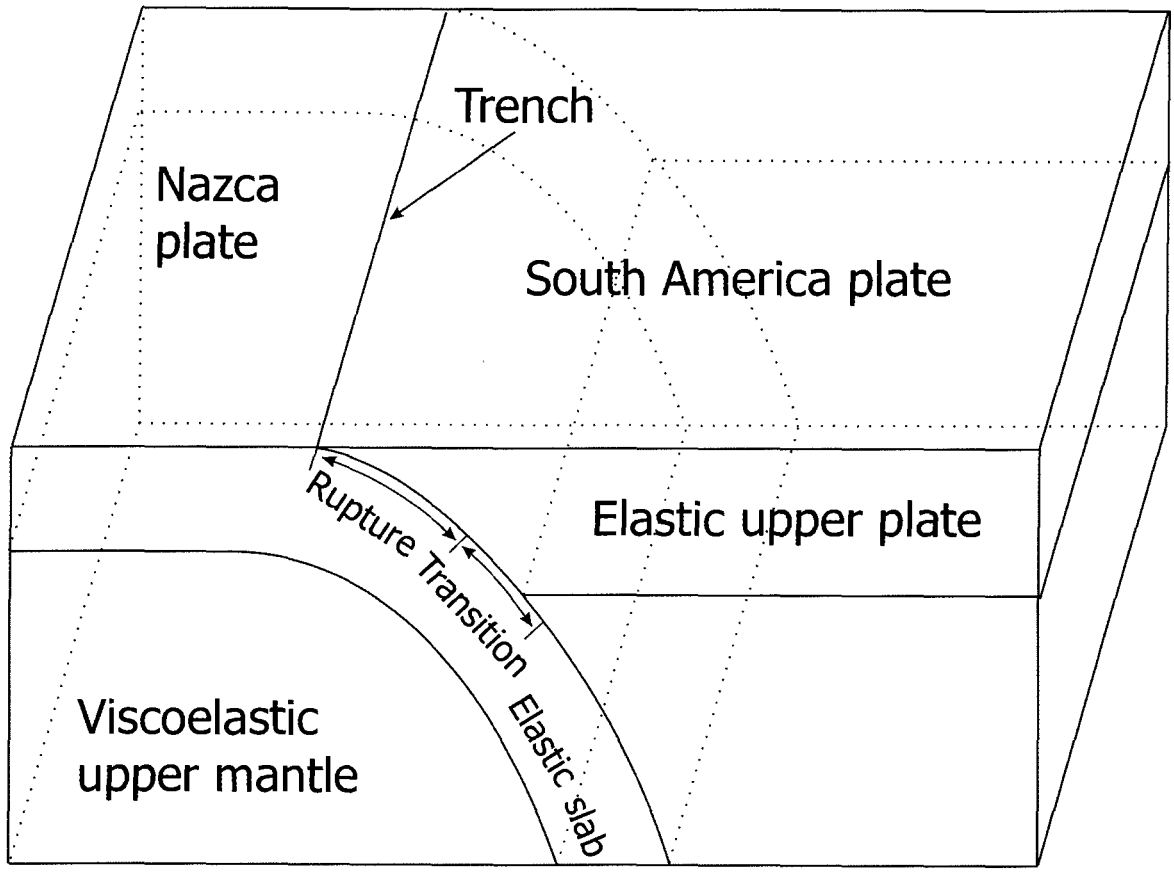

Figure 4.9. A conceptual representation of the 3-D viscoelastic model. The model consists of elastic continental and oceanic plates, an elastic subducting slab, and a viscoelastic upper mantle.

published contour lines of 50 km, 100 km, 150 km and 200 km from 20°S to 40°S at the Chile subduction zone. Dewey and Lamb (1992) plotted contour lines of 50 km, 100 km, 150 km, 200 km and 600 km from 0° to 40°S. Linde and Silver (1989) used a two-segment slab with a dip of ~15° from the surface to 35 km depth and ~30° further downdip. South of 40°S, there is no contour data available. A generalized shape of the subducting slab is obtained by averaging and smoothing the above data. (2) The generalized slab shape is fitted with a parabola function using the least squares method. The 2-D parabola slab shape is then used for all the trench-normal profiles of the 3-D model. That is, all the trench-normal cross-sections are identical. This is consistent with the fact that there is little variation of the slab geometry south of 35° along the Chilean margin.

The finite element mesh is shown in Figure 4.10. The bottom of the mesh is assumed to be 500 km deep, in the middle of the mantle transition zone. At all boundaries except the free surface, displacements perpendicular to the boundaries are fixed to be zero, and displacements parallel to the boundaries are not constrained. The mesh extends from 650 km seaward of the trench to 650 km landward of the trench and is 3000 km long in the along-strike dimension. Changing the trench-normal boundaries to 1500 km seaward of the trench and 1500 km away landward of the trench will produce similar overall pattern of the surface velocities (results will be shown in later sections). The model boundaries are deliberately set very far away from the region of interest in order to minimize the effects of boundary conditions. There are a total of 27,170 tri-linear eight-node elements, with grid spacing ranging from 0.4 km around the subduction fault to over 200 km at the model boundaries.

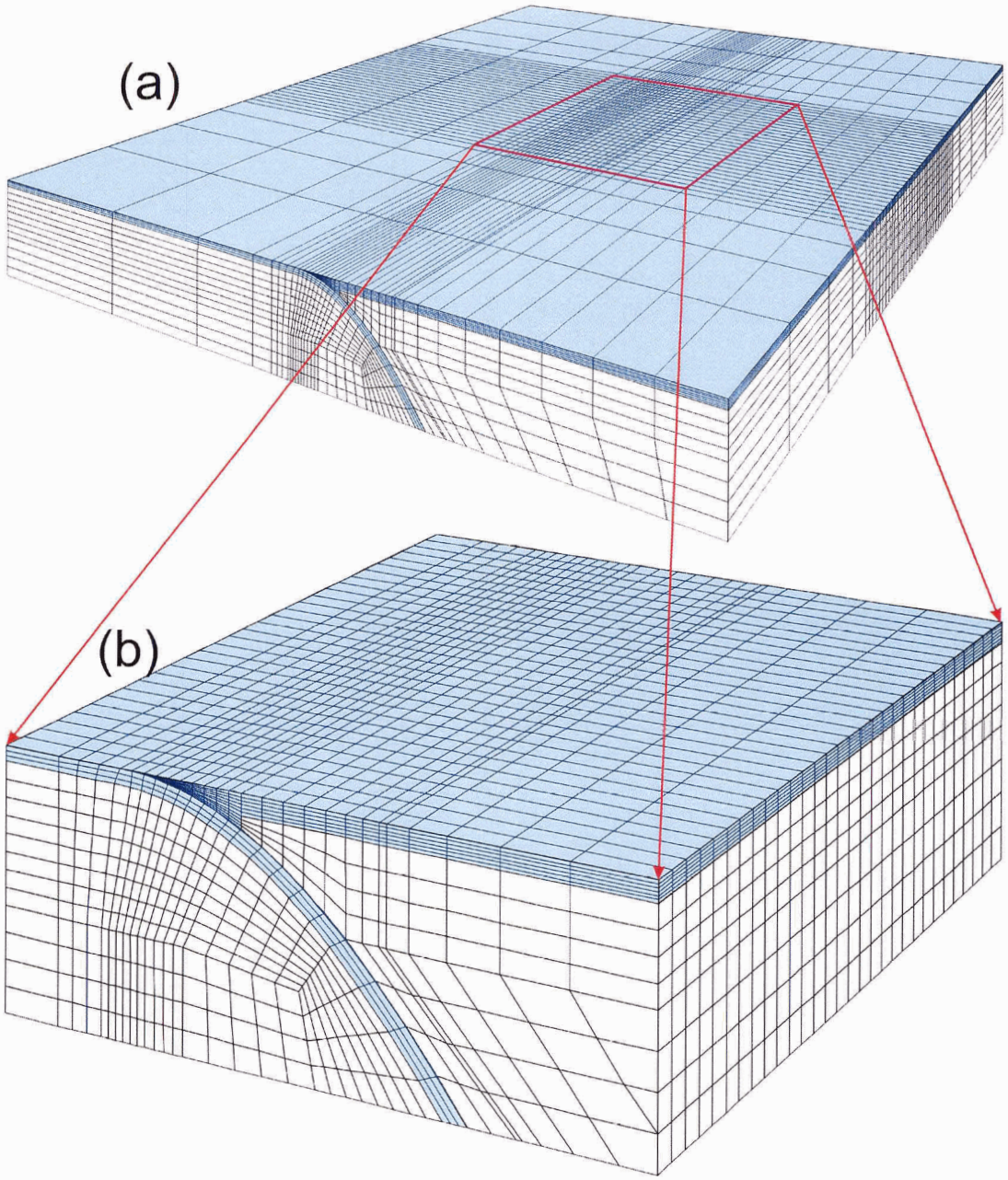

Figure 4.10. Three-dimensional finite element mesh: (a) Entire mesh. (b) Centre part of the mesh. Coloured and white elements represent elastic plates and viscoelastic upper mantle, respectively. The size of the mesh model frame is 3000 km along strike and 500 km vertically. The trench-normal dimension is 1300 – 3000 km in different model tests. The rupture zone of fault plane is 120 km wide in the downdip direction, and the transition zone is 80 km wide. The average dip of the seismogenic shallow party of the curved plate interface is 18°.

Using one processor of an IBM ATX supercomputer, one time step for a model with the mesh shown in Figure 4.10 takes about 5 minutes, and each solution takes 5 to 10 hours.

4.4.2. Physical Properties

The Young's modulus of the elastic plates and mantle are assumed to be 120 GPa and 160 GPa, respectively, and the Poisson's ratio is assumed to be 0.25 for the entire system (Wang et al., 2001). The rock density is assumed to be 3.3 g/cm^3 for the entire system (Wang et al., 2001). The gravity acceleration g is assumed to be 10 m/s^2.

4.4.3. Fault Plane and Slip Constraints

The slip on the fault is prescribed using the split-node method (Melosh and Raefsky, 1981). In this work, the earthquake is modelled as an instantaneous uniform forward slip over a rectangular rupture zone 900 km long along-strike and 120 km wide (dark area in Figure 4.11a). In plan view, the rupture zone is at the centre of the model domain. Based on previously published results (Plafker, 1972; Barrientos and Ward, 1990; Klotz et al., 2001), a 20 m uniform forward coseismic slip in the plate convergence direction at N80°E is applied over the rupture zone (left panel of Figure 4.12). The slip linearly decreases to zero over a transition zone surrounding the full-slip zone (grey area in Figure 4.11a). The transition zone is assumed to be 80 km wide in the downdip direction. Similar transitions of 50 km wide in the strike direction are added to the northern and southern edges of the fault to avoid abrupt termination of the coseismic rupture in these places.

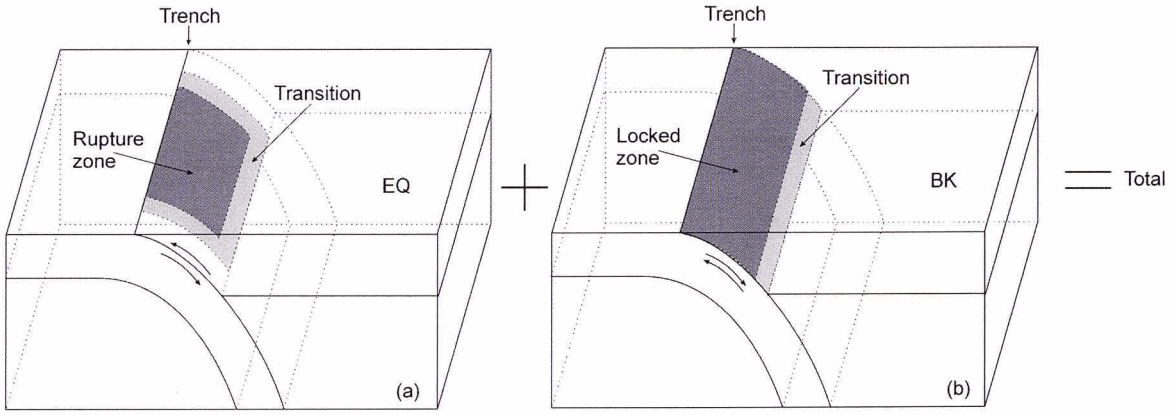

Figure 4.11. Fault plane and slip constraints in the model. (a) Dark and grey regions represent rupture (full-slip) and coseismic transition zones, respectively. (b) Dark and grey regions represent interseismic locked and transition zones, respectively.

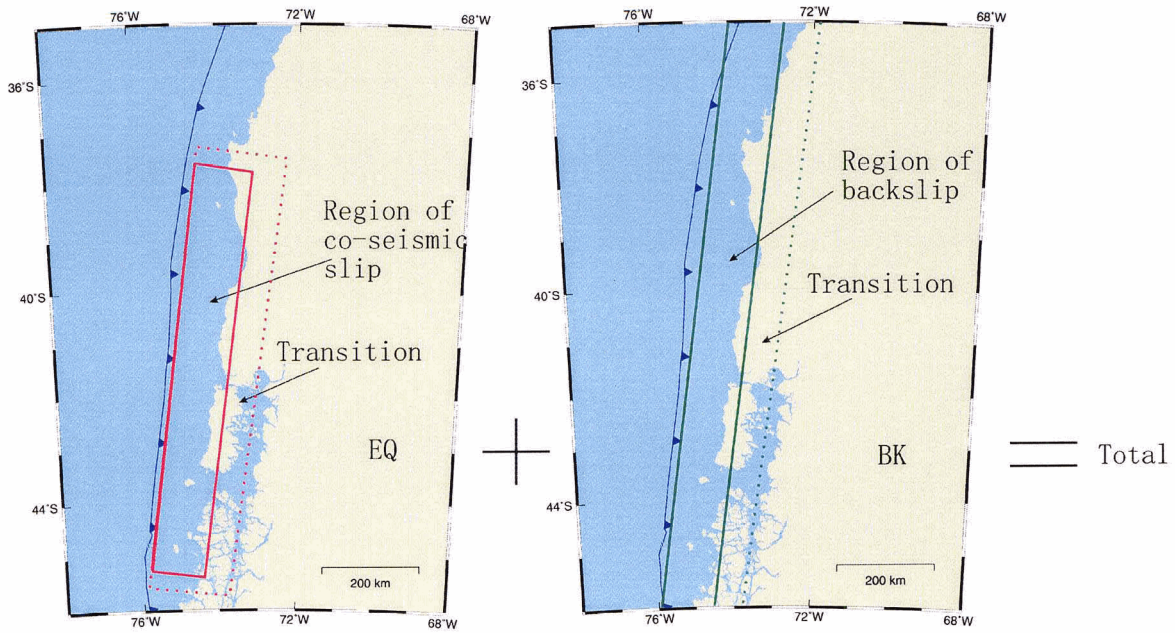

Figure 4.12. Plan view of the rupture zone (red solid lines), locked zone (green solid lines) and transition zones (dashed lines) used in the modelling. The combined effect of the earthquake and fault locking is obtained using a linear combination of the results of the two separate models.

After the earthquake, the rupture zone is assumed to be fully locked, and the coseismic transition zone becomes the interseismic transition zone. The 1960 earthquake only ruptured a segment of the Chilean margin (represented in my model by the left panel of Figure 4.12), but the Chilean subduction fault is believed to be locked along its entire length at present (Figure 4.3). Therefore, the locked and interseismic transition zones are extended from the rupture zone to the northern and southern mesh boundaries as shown by the dark and grey areas in the right panels of Figures 4.11 and Figure 4.12, respectively. The locking of the fault is modelled using the method of backslip (see section 3.2). In the locked zone, the backslip is at the plate subduction rate, representing a fully locked fault. Over the downdip transition zone, the backslip rate linearly decreases to zero. It will take 300 years to accumulate enough strain for the next 20-meter rupture event assuming a subduction rate of 66 mm/yr, or 250 years assuming a subduction rate of 80 mm/yr. A geodetically determined modern subduction rate of 66 mm/yr is assumed in this work for reasons discussed in section 3.1.1, but the NUVEL-1a rate of 80 mm/yr will also be tested. Assuming a viscosity of 3×10^{19} Pa s and a Young's modulus of 160 GPa, the mantle Maxwell relaxation time is ~15 years.

The last significant subduction earthquake in this area occurred in 1575 (Atwater et al., 2003), almost 400 years before the 1960 event. The time interval between the two events is much larger than the predicted cycle length of 250 – 300 years. Therefore, I assume the stress induced by the 1575 earthquake was pretty much relaxed in 1960 and use a zero pre-stress field for modelling.

Similar to section 3.4.2, the effects of the earthquake and of the subsequent locking of the fault are modelled separately (see section 3.2). The combined effect of the earthquake

and fault locking is obtained using a linear combination of the results of the two models (Figure 4.12).

4.5. Model Results

The model with parameters described in the preceding section, that is, elastic oceanic and continental plates of thickness 30 km and 40 km, respectively, material properties given in section 4.4.2, fault geometry shown in Figure 4.12, a ruptured locked zone of 120 km downdip width, and a transition zone of 80 km downdip width, is called the reference model. The upper mantle viscosity of the reference model is tested to be 3×10^{19} Pa s. The results of the reference model are discussed in this section. Various changes will be made to the reference model for better data fit and parameter tests.

4.5.1. Deformation due to the Earthquake Alone

The response to the earthquake is modelled by prescribing an instantaneous coseismic slip on the fault without subsequent fault locking. That is, the relative displacements of the nodes on the fault are fixed at 20 m with no subsequent backslip, although the displacements of these nodes as well as nodes in the rest of the model domain relative to model boundaries vary with time due to stress relaxation in the upper mantle and the interaction between the viscoelastic upper mantle and the elastic plates.

The earthquake instantaneously stretches the forearc and induces a shear stress in the model domain. If the upper mantle were purely elastic (viscosity $\eta = \infty$), the induced shear stress provides a resistance to the coseismic stretch and the stress would never relax, as discussed in section 3.3. Therefore, deformation in response to the earthquake would

always be constrained to a very small area in the vicinity of the thrust fault. However, also as discussed in section 3.3, if the upper mantle were a pure fluid with no shear strength (viscosity $\eta = 0$), no stress would be induced in the upper mantle, and the crustal deformation would be instantaneously transferred to any place in the elastic plate within the model boundary. The upper mantle viscosity of 3×10^{19} Pa s is a case in between.

The instantaneous stretch of the forearc results in seaward velocities in areas landward of the trench (Figure 4.13). The shear stress induced in the upper mantle then begins to relax. This leads to a decrease in seaward velocities in these areas. The surface velocities landward of the rupture zone are slightly oblique because of the oblique plate convergence, but the velocity component parallel to strike diminishes quickly with time. Velocities in this area are therefore normal to the trench at later stages of the earthquake cycle (Figure 4.13c, 4.13d). At t = 0, and immediately after, deformation is mainly constrained in an area less than 400 km from the trench due to the resistance provided by the induced shear stress in the upper mantle (Figure 4.14a). Subsequent relaxation of this stress allows a broader landward area to deform (Figures 4.14b, 4.14c, 4.14d). The displacements in the landward areas increase with time (Figure 4.14) to catch up with the forward coseismic slip.

The effects discussed above can be illustrated by surface velocities along the line of symmetry of the rupture zone (Figure 4.15). Trench-normal horizontal velocity Vy^{EQ} about 200 km from the trench is in the seaward direction and decreases from ~ 15 mm/yr at t = 35 years to ~5 mm/yr at t = 200 years. Surface vertical velocity Vz^{EQ} in this area varies from ~3 mm/yr uplift rate at t = 35 years to ~5 mm/yr subsidence at t = 200 yr. The

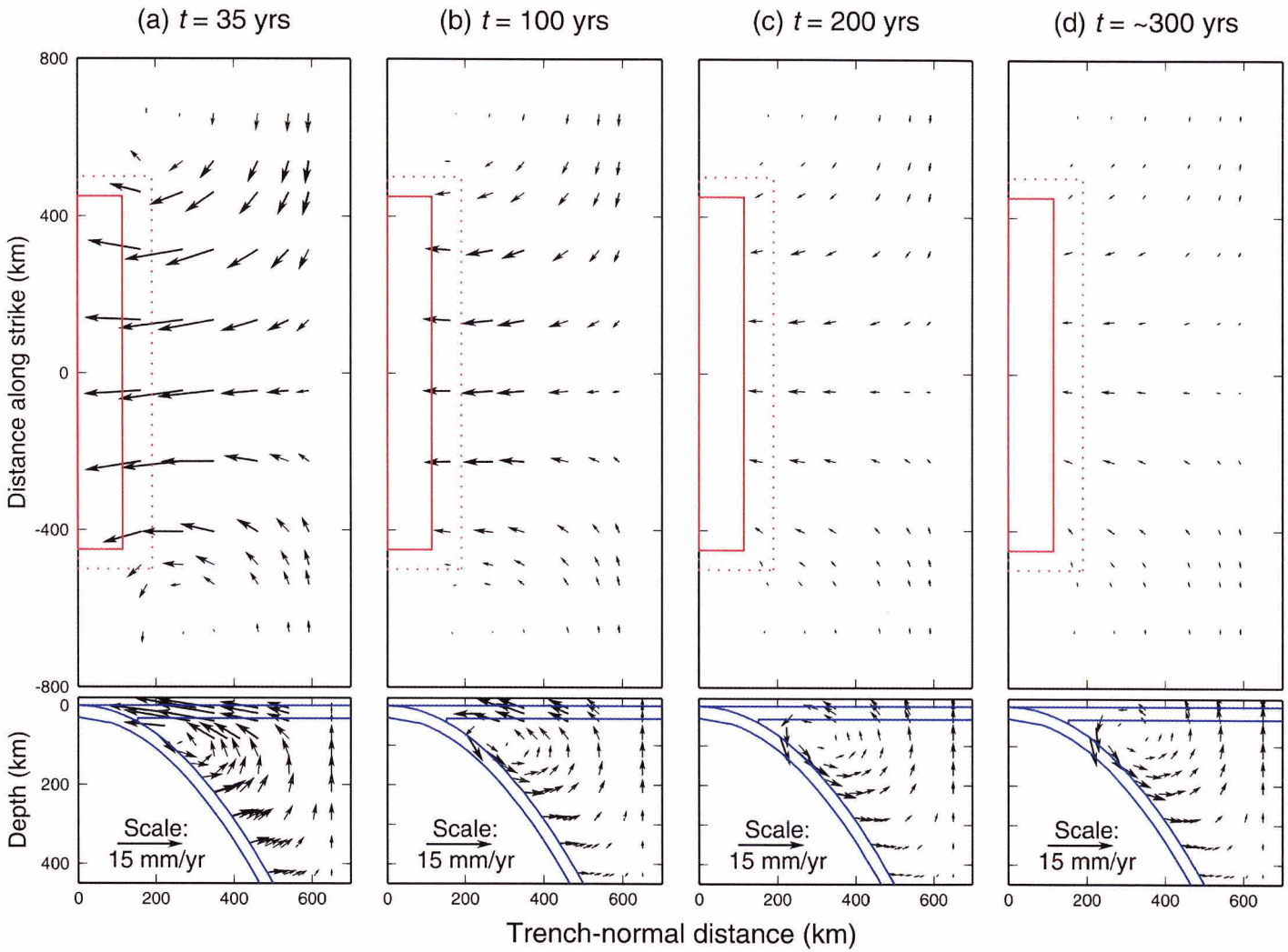

Figure 4.13. Velocities in response to the earthquake alone with no subsequent fault locking. Upper panel shows the surface velocities in plan view. Lower panel is a cross-section along the line of symmetry of the rupture zone. Solid and dotted red lines outline the rupture and transition zones, respectively. Blue solid lines outline the continental plate and subducting slab.

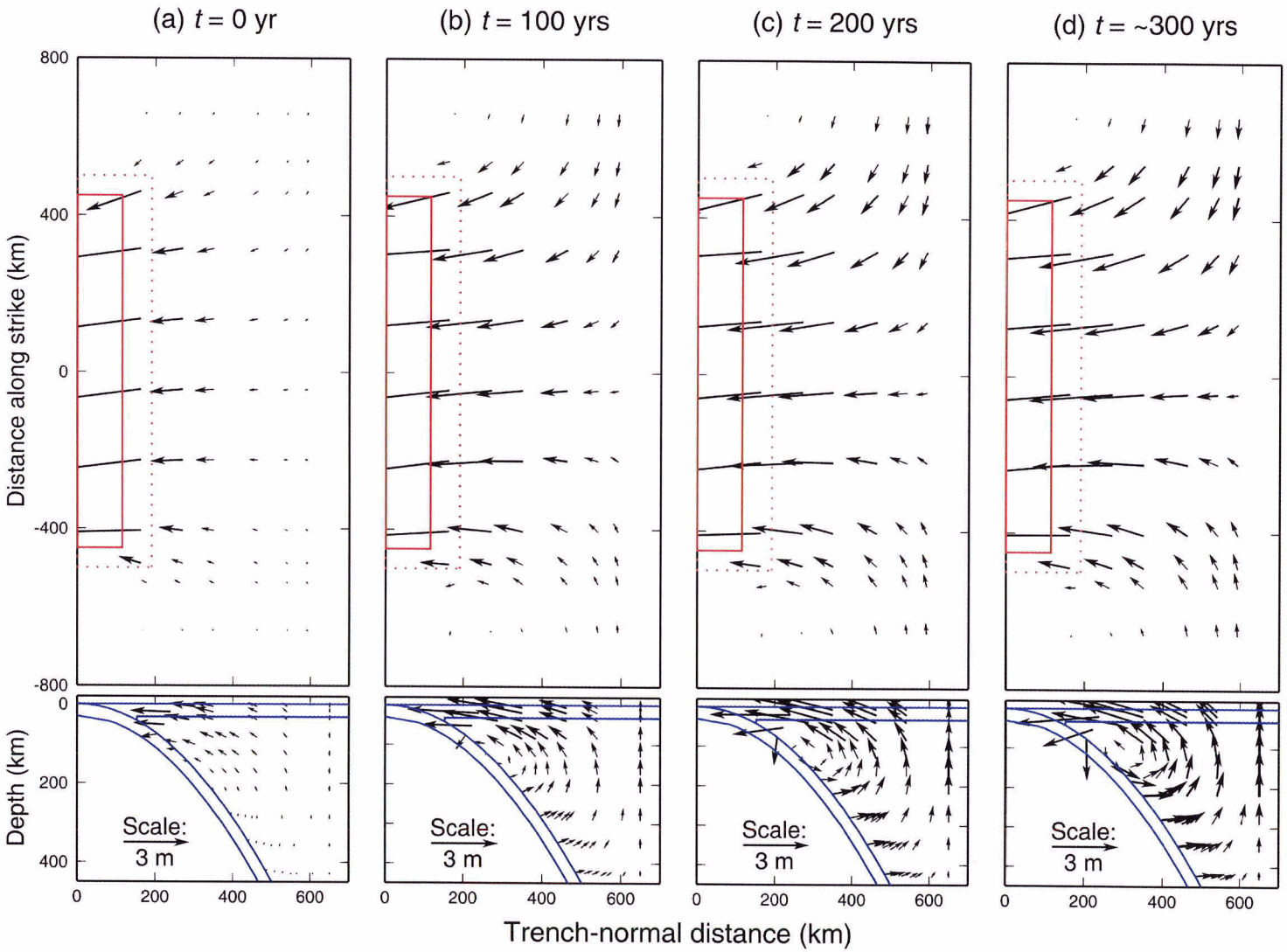

Figure 4.14. Displacements in response to the earthquake alone with no subsequent fault locking from the same model as in Figure 4.13. Upper panel is the plan view. Lower panel is in a cross-section along the trench-normal line of symmetry of the rupture zone.

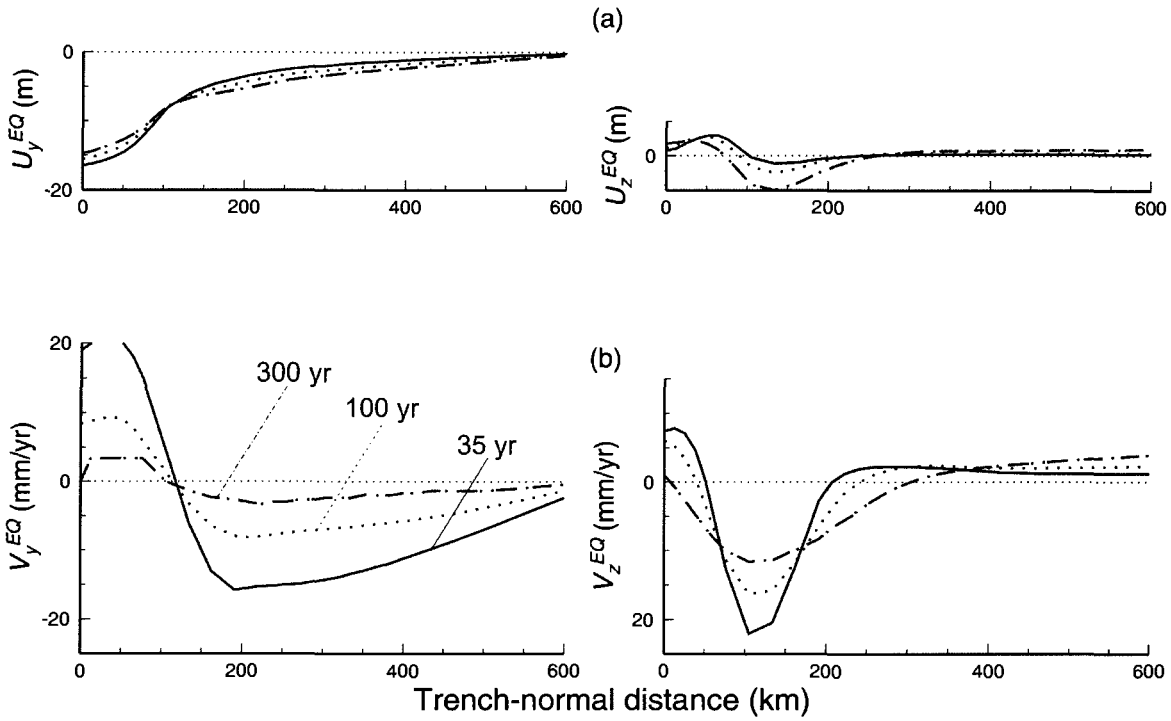

Figure 4.15. Surface displacements (a) and velocities (b) along the trench-normal line of symmetry of the rupture zone in response only to the earthquake (i.e., no subsequent fault locking) from the same model as in Figures 3.13 and 3.14. Solid, dotted, and dot-dashed lines represent velocities 35, 100, and 300 years after the earthquake, respectively.

time-dependent surface velocities reflect the interaction of the viscoelastic upper mantle and the elastic over-riding plate. The over-riding elastic plate appears to behave "viscously" after the event due to its coupling with the viscoelastic upper mantle.

4.5.2. Deformation due to Fault Locking Alone

The response to on-going subduction with a locked plate interface is modelled by imposing a backslip rate of 66 mm/yr without a preceding earthquake. The fault is suddenly locked at time $t = 0$. The relative displacement of the split nodes over the fault increases at the subduction rate from zero at $t = 0$ to 20 m at $t = 300$ years.

The motion of the subducting plate with the fault locked induces a much smaller shear stress in the model domain than that induced by the earthquake. At the very beginning of fault locking, the system behaves elastically, and crustal deformation is limited within an area near the locked zone (e.g., Figure 4.16a). This is because of the induced elastic stress in the upper mantle, similar to that induced by the coseismic slip but much smaller and in the opposite sense. Such elastic deformation can be modelled using the elastic dislocation model. At later times, stress in the mantle induced by fault locking and plate subduction at previous times begins to relax. "Newly" induced stress by the on-going subduction plate (backslip) is continuously added to the existing stress. The interseismic stress loading is oppositely directed to the coseismic loading. As well, it is gradual, and allows relaxation to take place at the same time. Because of the relaxation of the existing stress in the upper mantle, the crustal deformation takes place over a region that becomes wider with time (Figure 4.16b, 4.16c, 4.16d). The displacements in the landward areas increase with time (Figure 4.17) due to fault locking. For the elastic

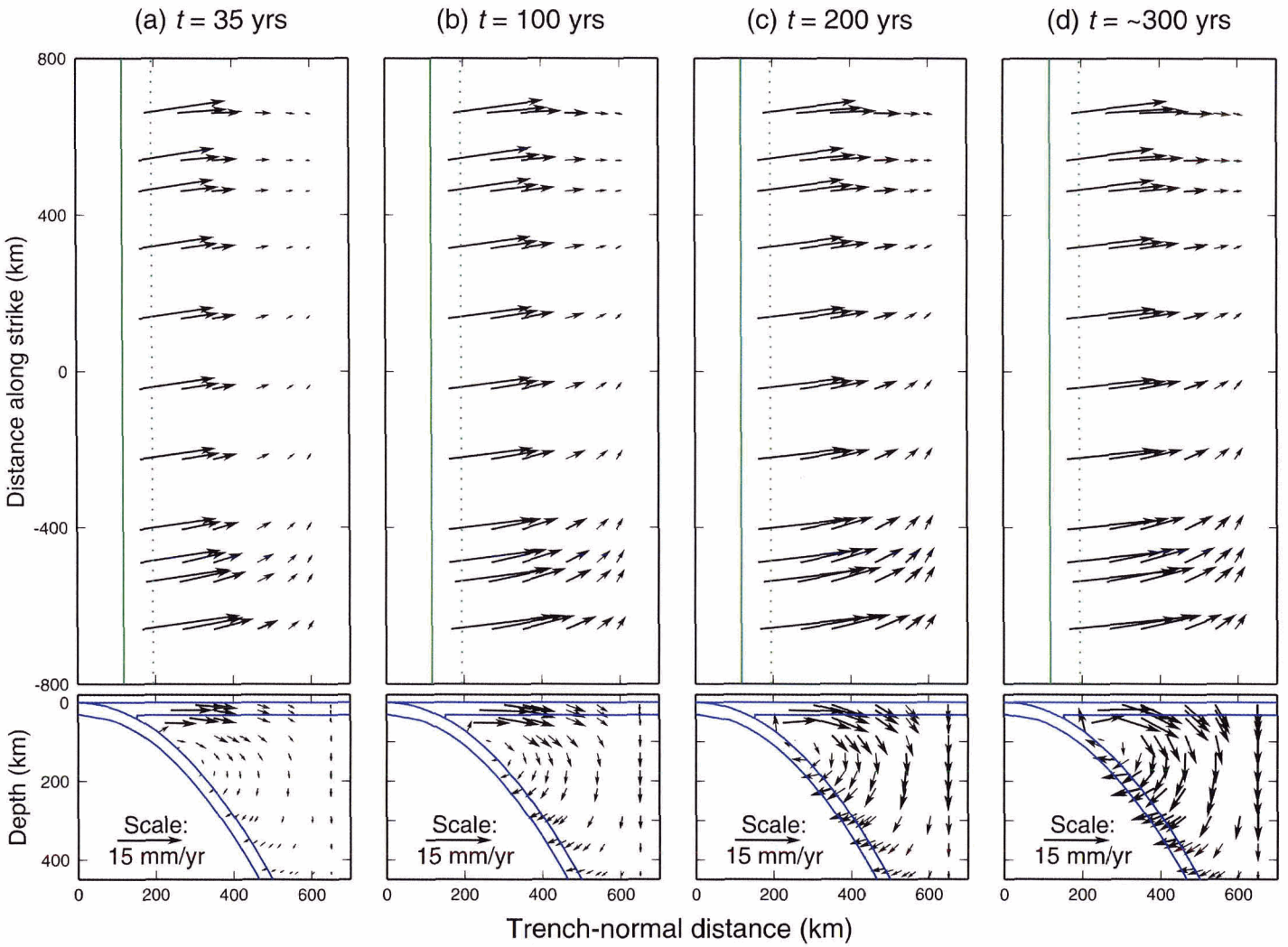

Figure 4.16. Velocities in response to fault locking alone with no preceding earthquake. Upper panel is the plan view. Lower panel is a cross-section along the trench-normal line of symmetry of the rupture zone. Solid and dotted green lines in the upper panel outline the locked and transition zones, respectively.

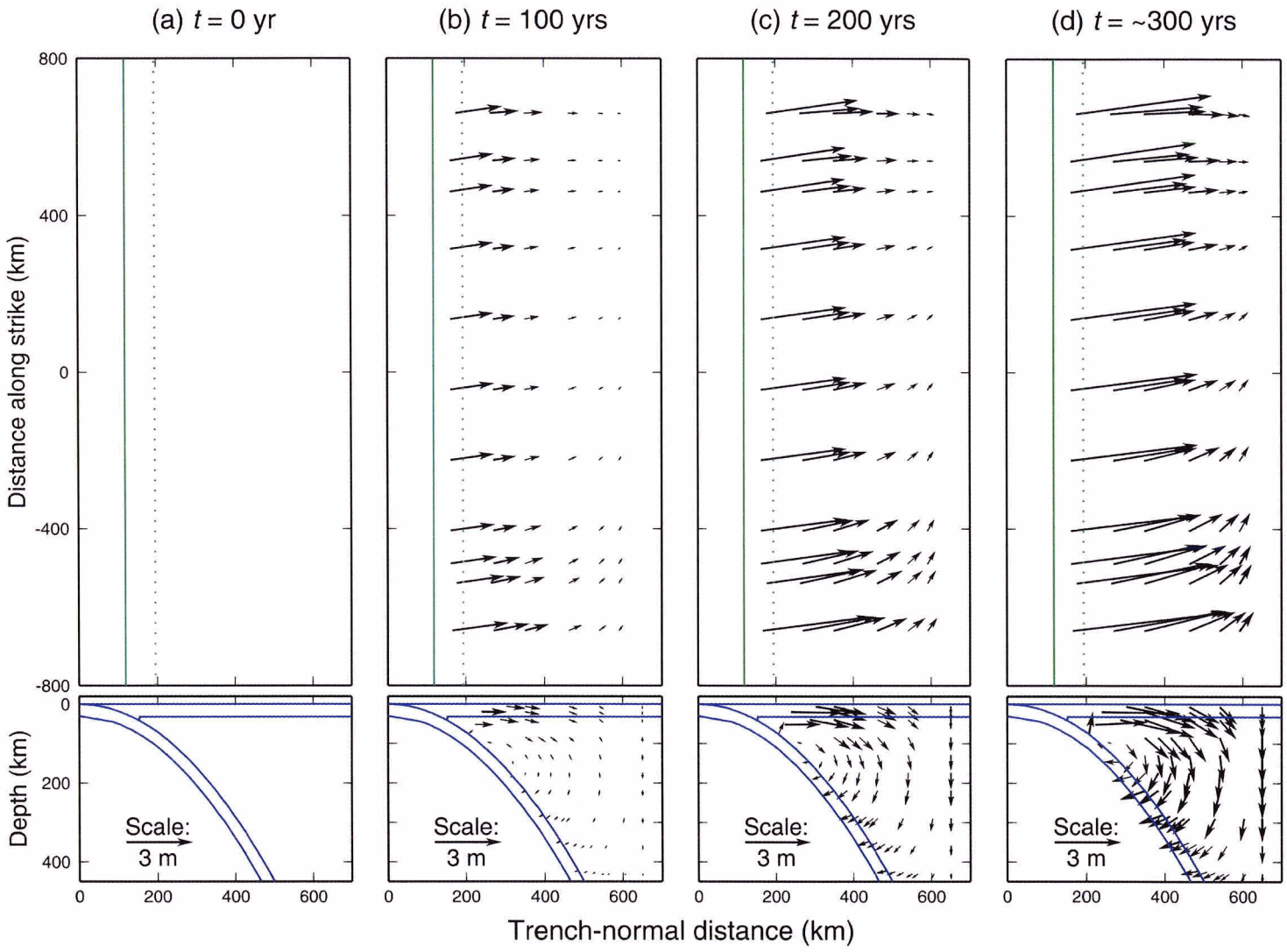

Figure 4.17. Displacements in response to fault locking with no preceding earthquake from the same model as in Figure 4.16. Upper panel is the plan view. Lower panel is a cross-section along the trench-normal line of symmetry of the rupture zone.

dislocation model (Savage, 1983), the region of the crustal deformation does not vary with time.

Along the line of symmetry of the model, the surface horizontal velocity Vy^{BK} about 100 km from the trench is in the landward direction and increases with time (Figure 4.18a). The surface vertical velocity Vz^{EQ} about 200 km from the trench indicates subsidence and increases with time (Figure 4.18b). This represents strain accumulation in the upper plate.

4.5.3. Deformation due to the Earthquake as Well as Fault Locking

The response to an earthquake followed by fault locking is obtained using a linear combination of the results of the two separate models discussed above. The coseismic slip induces a shear stress in the upper mantle and downdip extension of the fault, resulting in seaward velocities in the continental crust (Figure 4.19a). The subsequent fault locking induces a much smaller shear stress in the opposite sense. At this beginning stage, the combined effects are completely dominated by the effect of the stress induced by the earthquake. The crustal deformation is limited to a small area near the thrust fault (Figure 4.20a) due to resistance by the elastic shear stress in the upper mantle. At a later time, the crustal deformation is controlled by three factors: the earthquake, fault locking at previous times, and fault locking at the given time. The relaxation of the shear stress induced by the earthquake causes seaward velocities in the inland area to slow down (Figure 4.19). The relaxation of the shear stress induced by fault locking at previous times causes landward velocities in this area to increase. The shear stress induced by fault

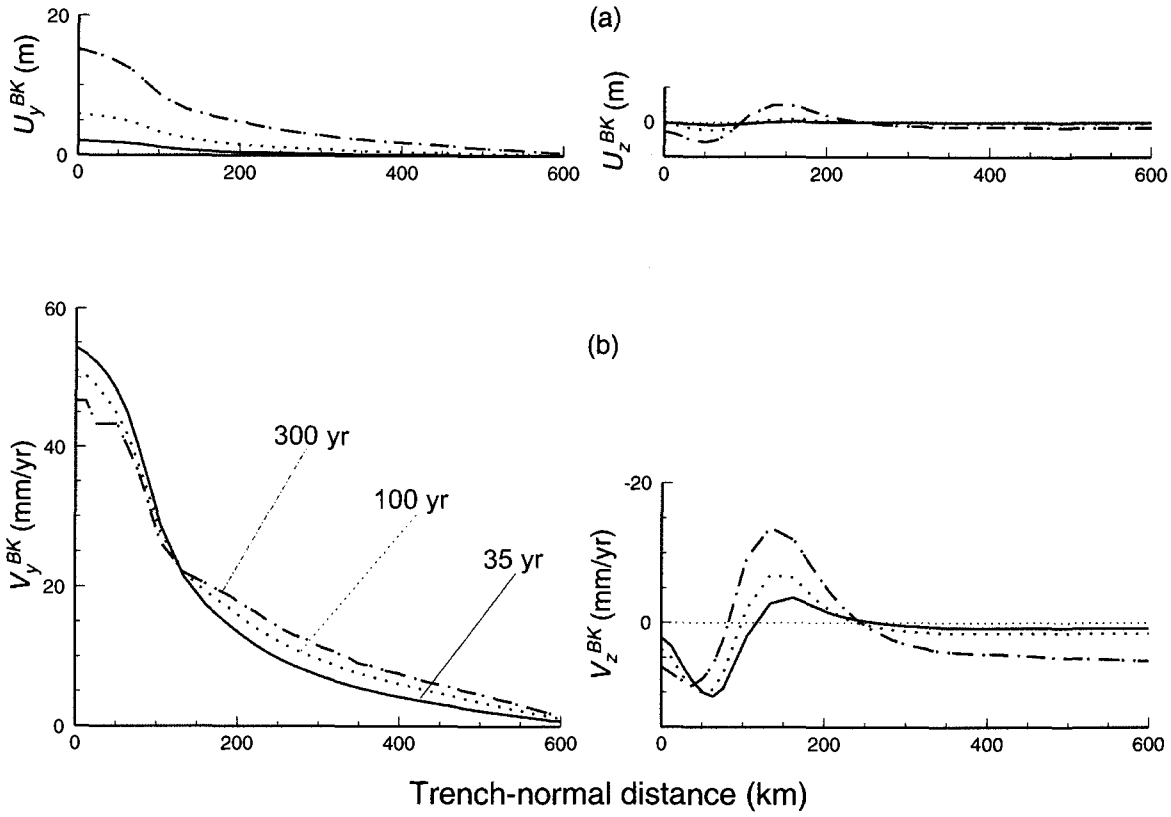

Figure 4.18. Surface displacements (a) and velocities (b) along the trench-normal line of symmetry of the rupture zone purely in response to fault locking from the same model as in Figures 4.16 and 4.17. Solid, dotted, and dot-dashed lines represent velocities 35, 100, and 300 years after the earthquake, respectively.

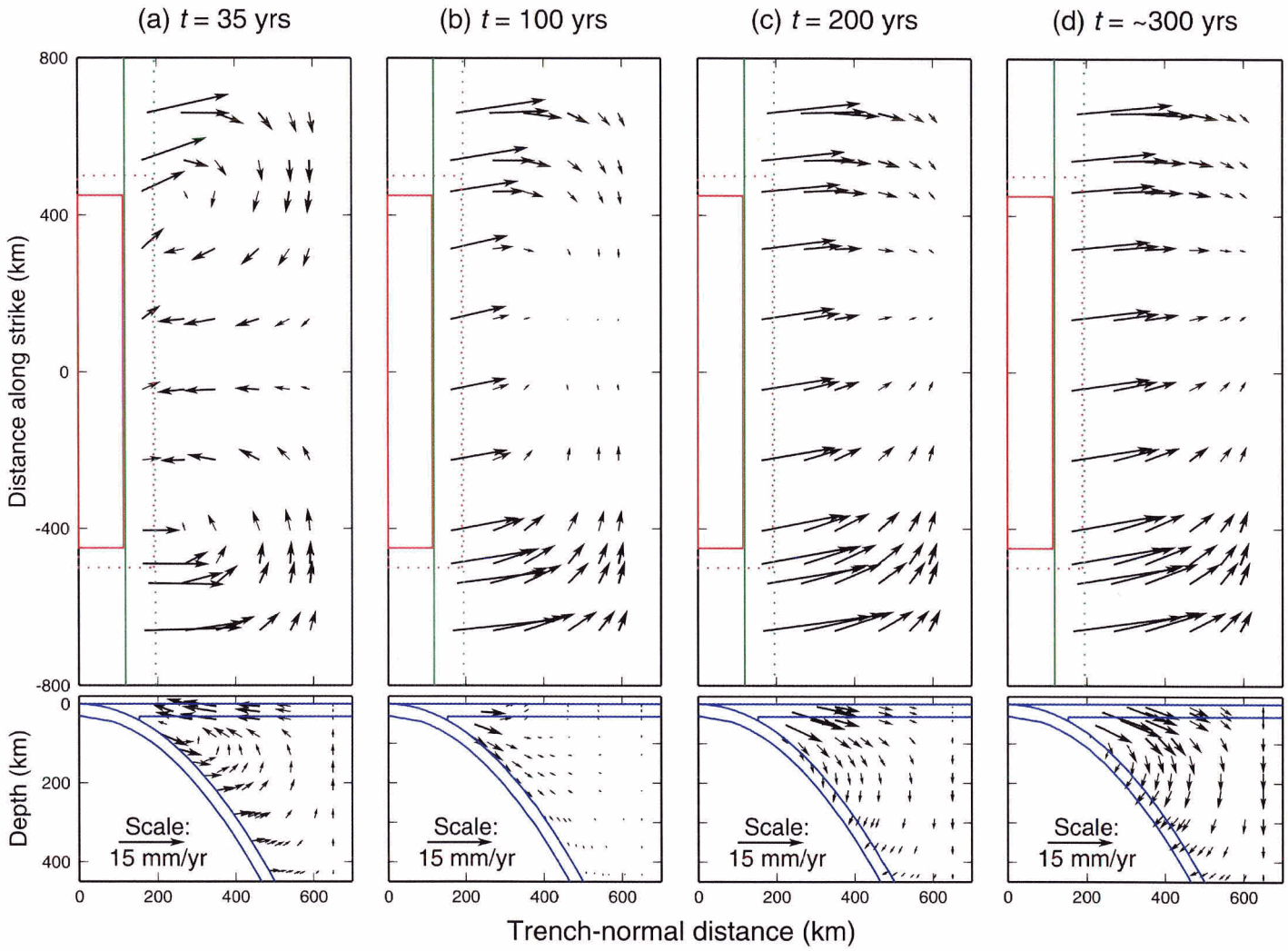

Figure 4.19. Velocities in response to the earthquake followed by fault locking (i.e., combination of Figures 4.13 and 4.16). Upper panel is the plan view. Lower panel is a cross-section along the trench-normal line of symmetry of the rupture zone. Solid and dotted red lines outline the rupture and transition zones, respectively. Solid and dotted green lines outline the locked and transition zones, respectively.

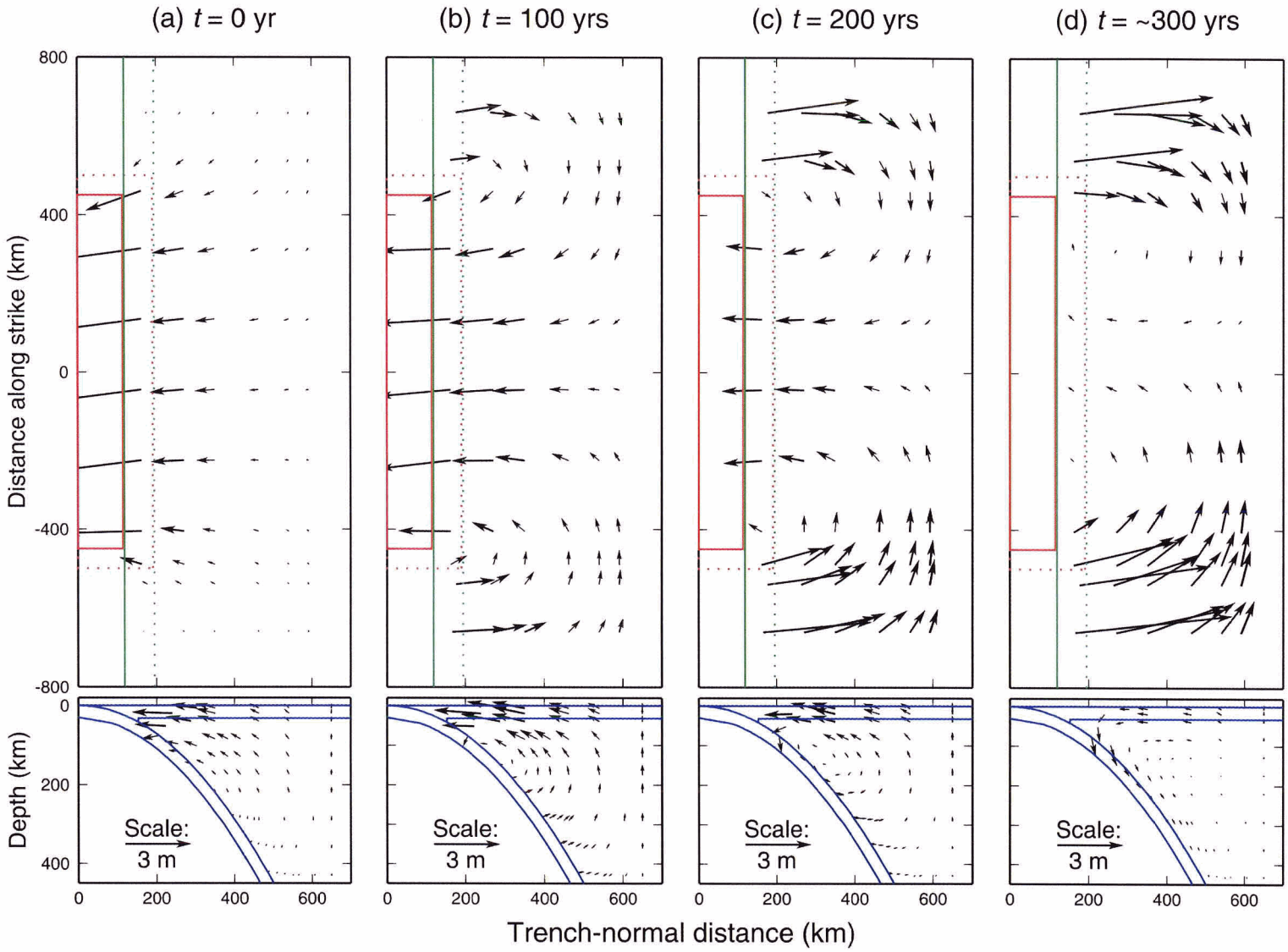

Figure 4.20. Similar to Figure 4.19, but shown is the displacement instead of velocity of the same model.

locking at the given time results in elastic crustal deformation limited within a small area near the locked zone.

The combined effect depends on the balance of these three contributions. At early stages in the earthquake cycle (e.g., 35 years and 100 years after the earthquake in Figure 4.20), the effect of the earthquake dominates in areas landward of the rupture zone. North and south of the rupture zone, the effects of fault locking always dominate. This results in increasing landward velocities and displacements in these areas. At later stages of the earthquake cycle, earthquake induced shear stress in the upper mantle is mostly relaxed, and hence the effect of fault locking dominates. This leads to an increase in landward velocities (Figure 4.19) and a decrease in seaward displacements (Figure 4.20) in the area landward of the rupture zone.

Surface velocities along the line of symmetry of the rupture zone (Figure 4.21) further illustrate the effects discussed above. At 35 years after the event, the surface horizontal velocity Vy^{Total} at a distance greater than about 200 km from the trench is in the seaward direction and decreases with time. This indicates that the effect of the earthquake dominates. Later, the direction of Vy^{Total} in this area changes direction, and becomes increasingly landward. The peak value of the subsidence in the inland area about 100 km from the trench decreases with time. The direction of surface vertical velocity Vz^{Total} at about 200 km from the trench is reversed 100 years after the event (Figure 4.21b). Model postseismic ground uplift in this area changes to interseismic subsidence. This indicates the domination of the effect of fault locking. Moving the trench-normal boundaries closer to the trench (e.g., 650 km, the blue line in Figure 4.21) does not change the overall pattern of the seaward motion 200 – 400 km from the trench.

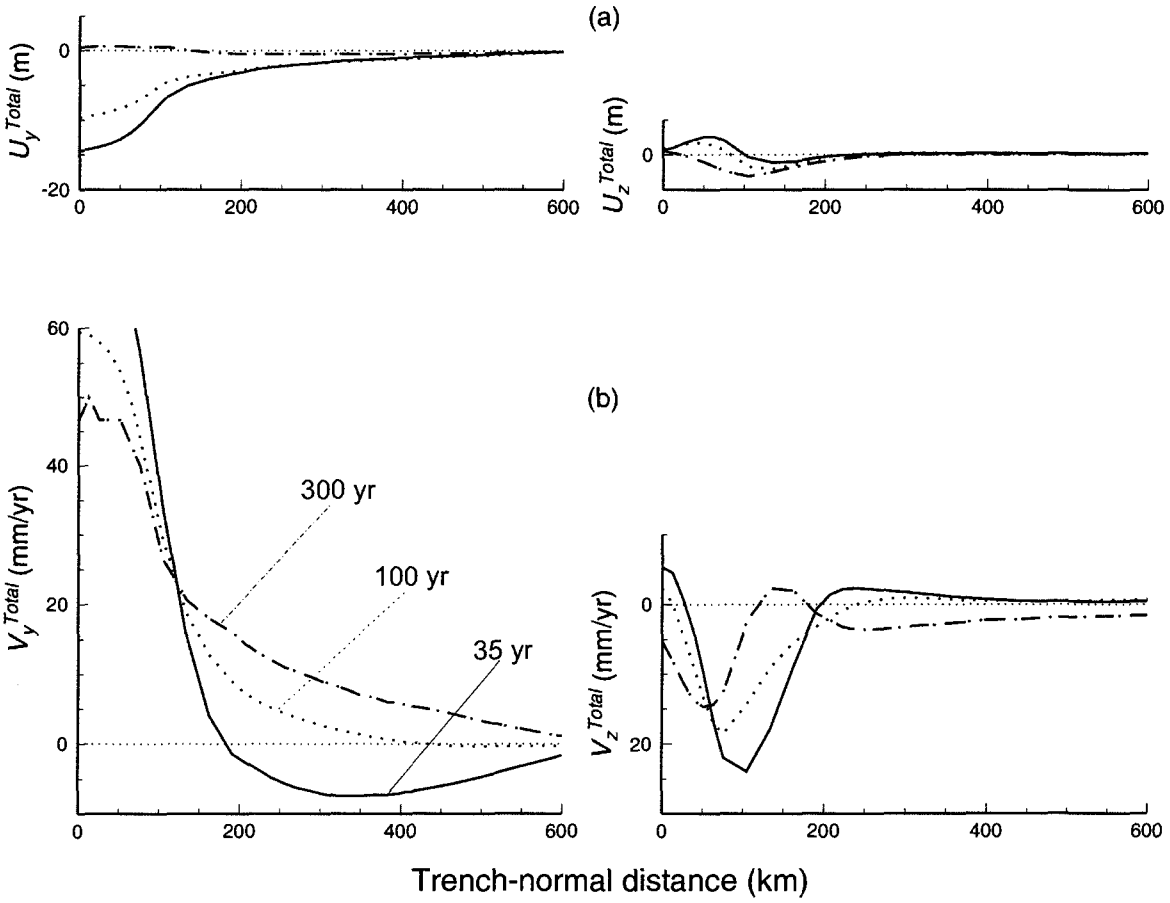

Figure 4.21. Surface displacements (a) and velocities (b) in response to the earthquake followed by fault locking along the trench-normal line of symmetry of the rupture zone. Solid, dotted, and dot-dashed lines represent velocities 35, 100, and 300 years after the earthquake, respectively.

4.5.4. Comparison With GPS Observations

In order to compare the model results with GPS campaign data, the GPS data on the surface of the spherical earth are mapped into the Cartesian reference frame of the model as discussed in section 4.3.1. The origin of the Cartesian reference is assumed to be at latitude 41.5°S and longitude 75.6°W.

Figure 4.22 shows the plan view of model predicted surface velocities and GPS observations 35 years after the event using a uniform upper mantle viscosity 3×10^{19} Pa s. The model reproduces the seaward motion of inland area quite well, but model predicted velocities north of the Chile 1960 earthquake rupture zone (from 35°S to 38°S) are smaller than the GPS observations. This indicates that the locked zone in the northern area may be larger. To reflect this difference, the geometry of the generic model in section 4.4 is modified to include broader locked and transition zones north of the Chile 1960 rupture zone (Figure 4.23). From $x = 450$ km to $x = 500$ km, the width of the locked zone linearly increases from 120 km to 160 km. Other model parameters remain unchanged.

A wider locked zone north of the rupture zone leads to a better fit to the GPS observations in this area (Figure 4.24). Given the simplicity of the model and uncertainties in the GPS data, the model reproduces the first-order pattern of the observed velocities reasonably well. The model further predicts that, 80 years after the earthquake, the seaward motion of the inland area will essentially disappear with seaward velocities less than 2 mm/yr (Figure 4.25). That is, after 2040, these GPS sites are not expected to detect significant seaward motion.

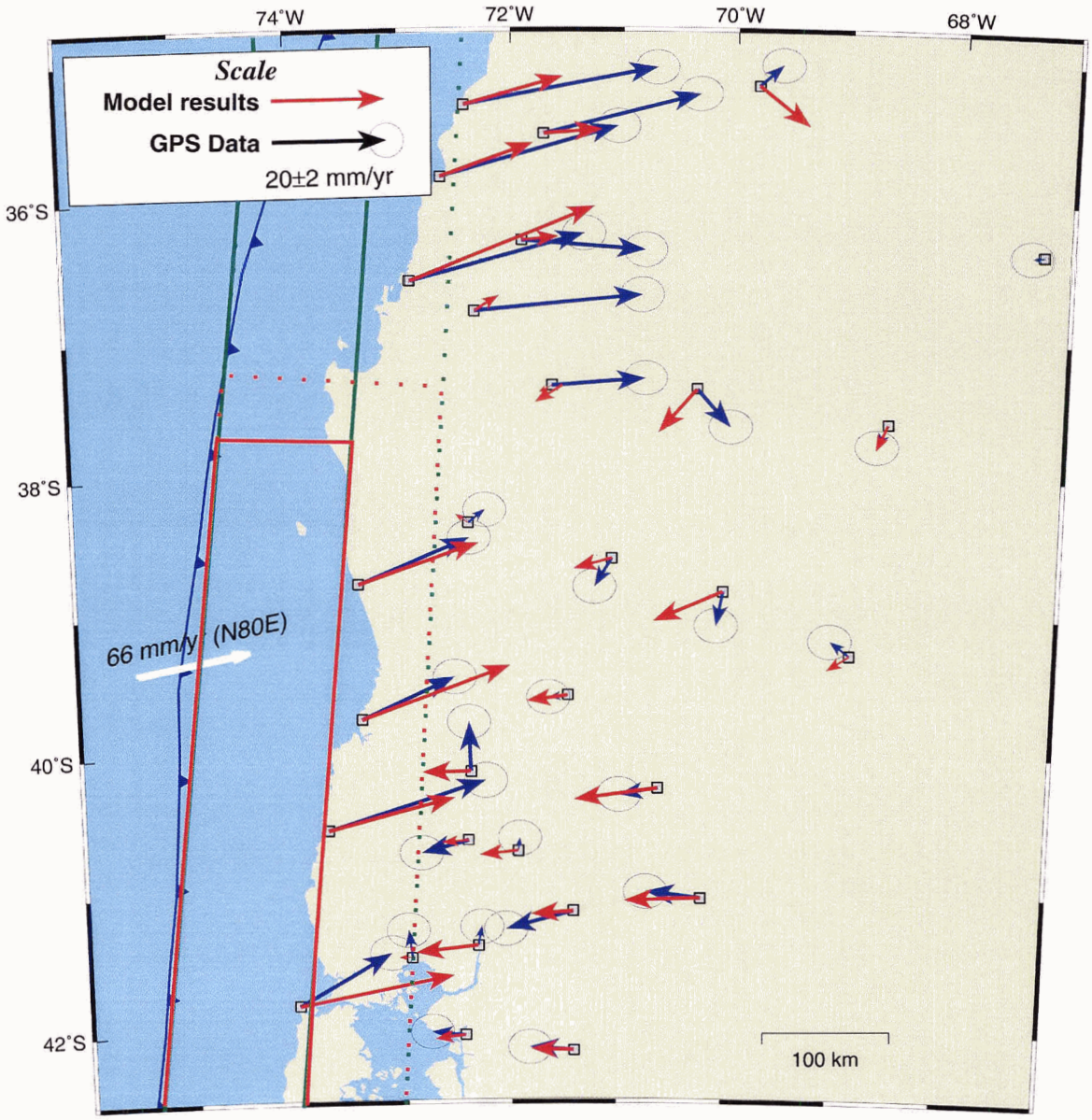

Figure 4.22. Comparison of velocities calculated using the reference model and GPS observations 35 years after the earthquake. Solid and dotted red lines outline the model rupture and transition zones of the 1960 Chile earthquake, respectively. Solid and dotted green lines outline the locked and transition zones, respectively.

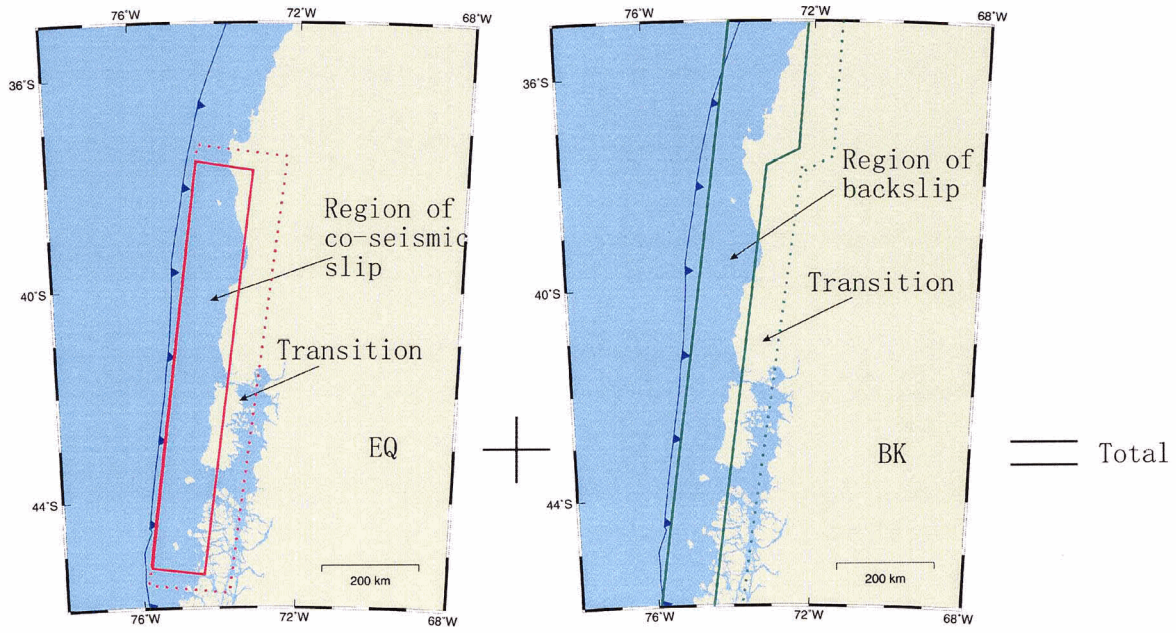

Figure 4.23. The interseismic locked zone (solid and dotted green lines) north of the 1960 Chile rupture zone is broadened to better fit the GPS observations in this area. The coseismic rupture and transition zones (solid and dotted red lines, respectively) remain unchanged. The width of the locked zone is linearly increased by 40 km over an along-strike distance of 50 km.

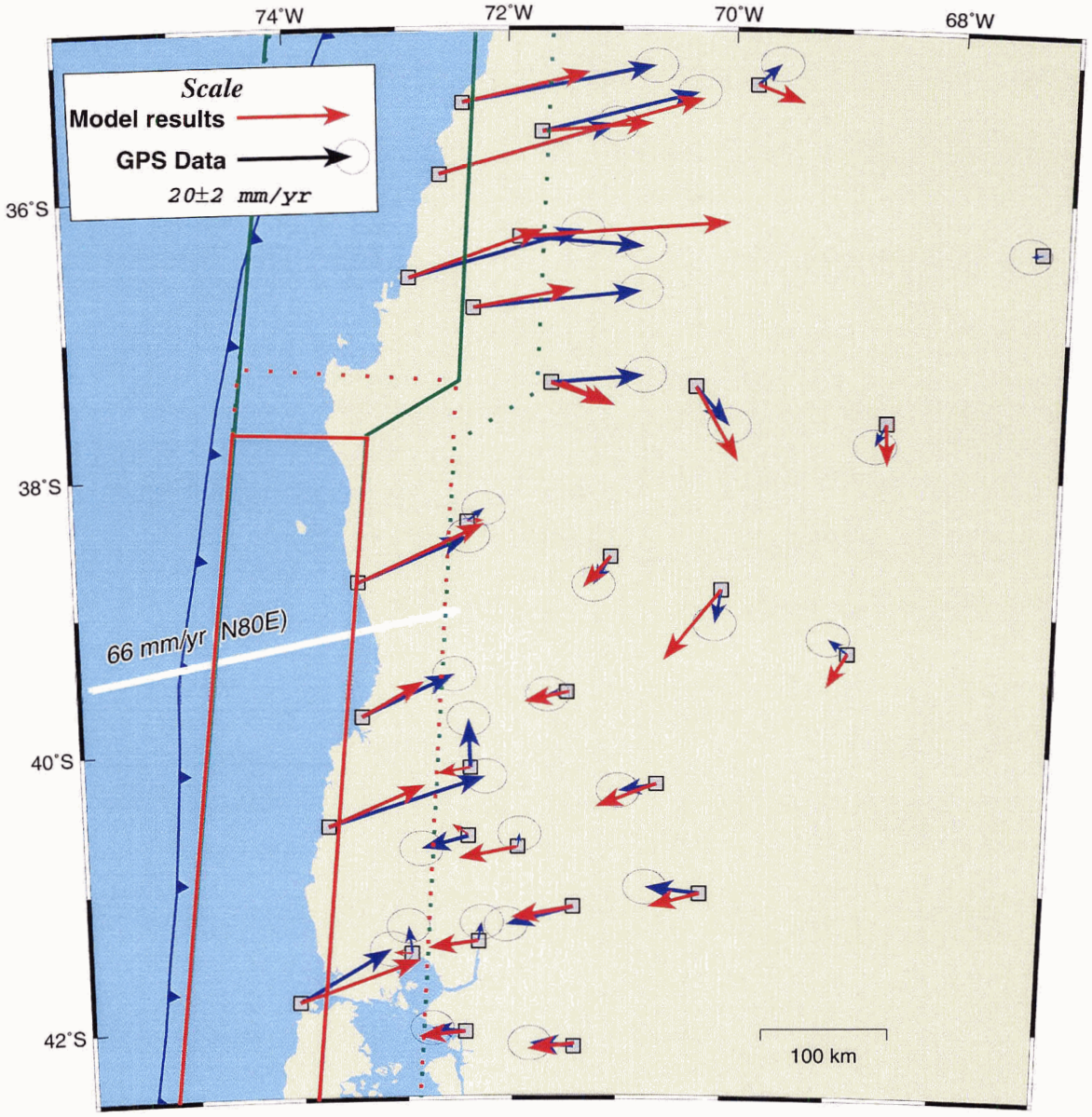

Figure 4.24. Comparison of GPS observations with model predicted velocities 35 years after the earthquake using a broader locked zone north of the 1960 Chile earthquake rupture zone (right panel of Figure 4.23). Solid and dotted red lines outline the rupture and transition zones of the 1960 Chile earthquake, respectively. Solid and dotted green lines outline the locked and transition zones, respectively.

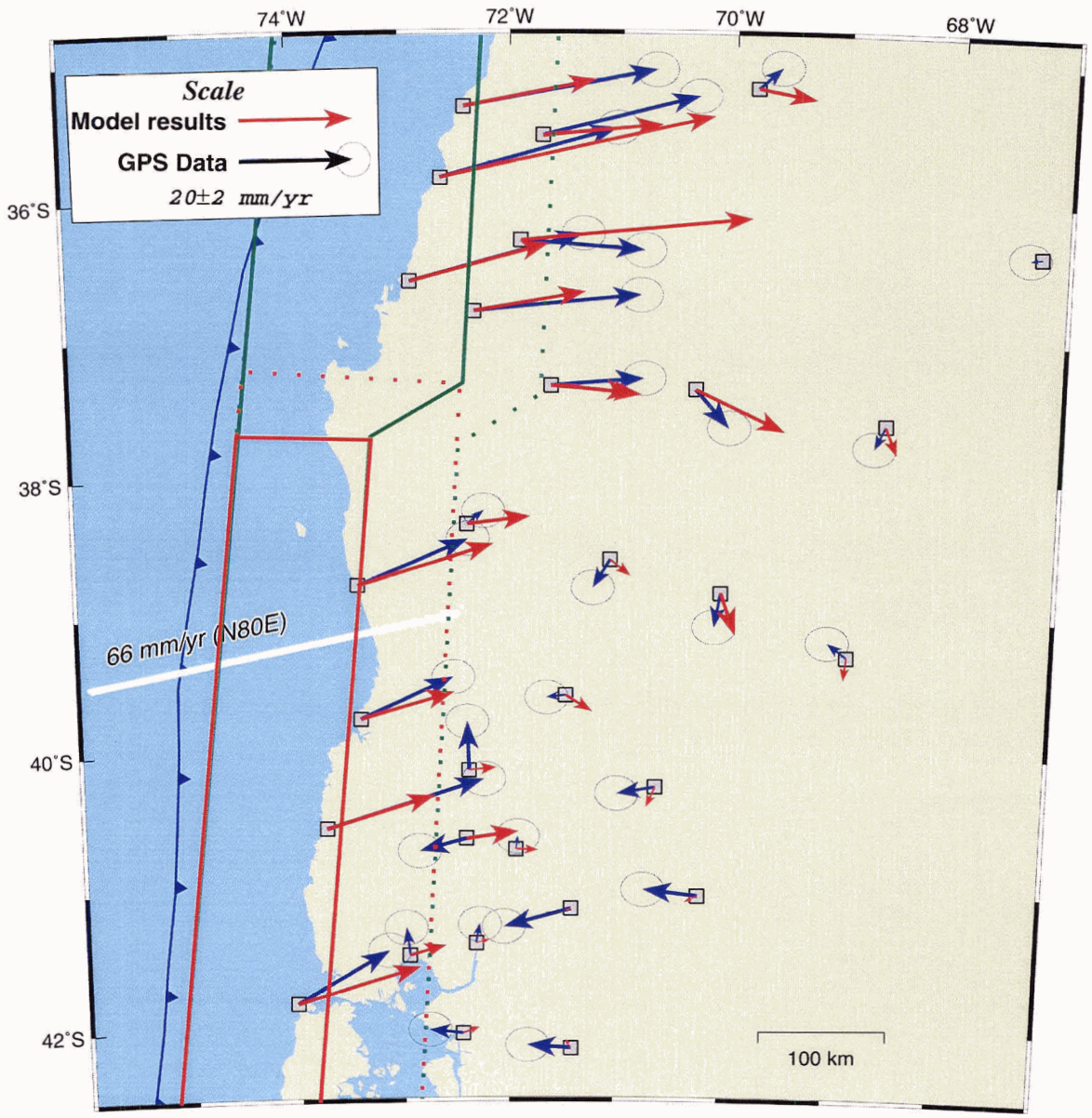

Figure 4.25. Velocities obtained by the same model as in Figure 4.24 but 80 years after the earthquake and GPS observations 35 years after the earthquake.

Either increasing or decreasing the upper mantle viscosity leads to a poorer fit to GPS observations 35 years after the event. The effect of the upper mantle viscosity will be studied in the following section.

4.5.5. Comparison With Other Deformation Observations

Plafker and Savage (1970) published 155 coseismic coastal deformation data. They observed a maximum coseismic subsidence of 2.7 m near Valdivia and a maximum coseismic uplift 5.7 m on three offshore islands: Isla. Mocha, Isla. Guafo, and Isla. Guamblin (Figure 4.1). My model predicts about 4 m coseismic uplift at these three islands and about 1 m coseismic subsidence near Valdivia (Figure 4.26). The model predicts maximum uplift and subsidence approximately in the same areas as that of the geological observations. The larger observed values may indicate that the coseismic slip in this area is locally larger (e.g., 30 m). A model with a larger coseismic slip in the areas of the coastal change observations may numerically better fit coseismic observations, but the heterogeneity of the slip distribution is neglected in this work.

Based on tide level data after eu static sea level change corrections, Nelson and Manley (1992) reported that Isla. Mocha (SW) had a decrease of 1.4 m and 1.76 m in tide level during 1960-1965 and 1965-1989, respectively (Figure 4.27). Model predicted displacement during 1960-1965 indicates ~1.2 m uplift at Isla. Mocha, consistent with the tide gauge observation of 1.4 m uplift in this area. However, the model predicts ~0.5 m subsidence at Isla. Mocha during 1965-1989. The poor fit during 1965-1989 may indicate other complications (e.g., aseismic afterslip, interseismic silent slip) in this region during 1965-1989. It is impossible to explain such a large temporal change in uplift pattern over

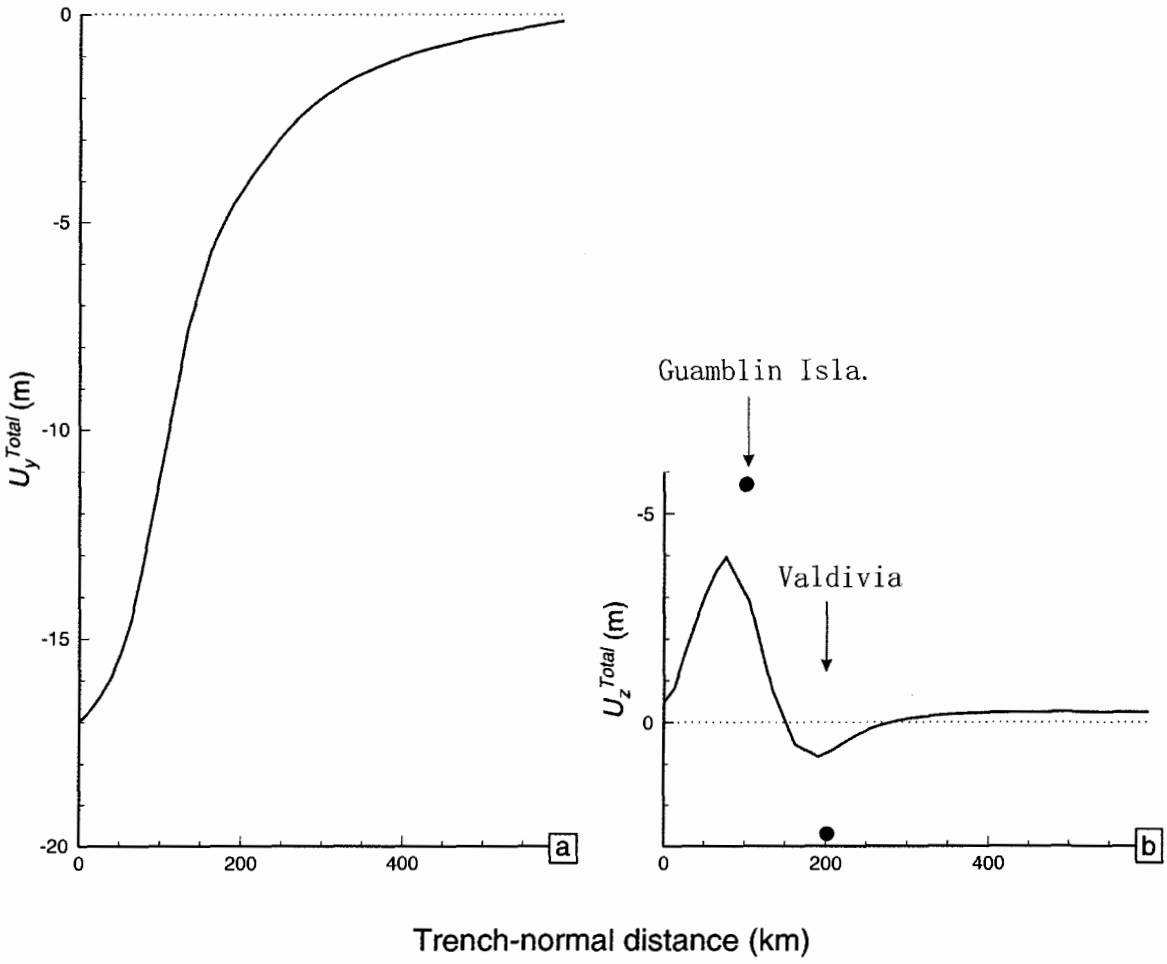

Figure 4.26. Model predicted coseismic surface vertical displacements. Black dot is coastal elevation change reported by Plafker and Savage (1970).

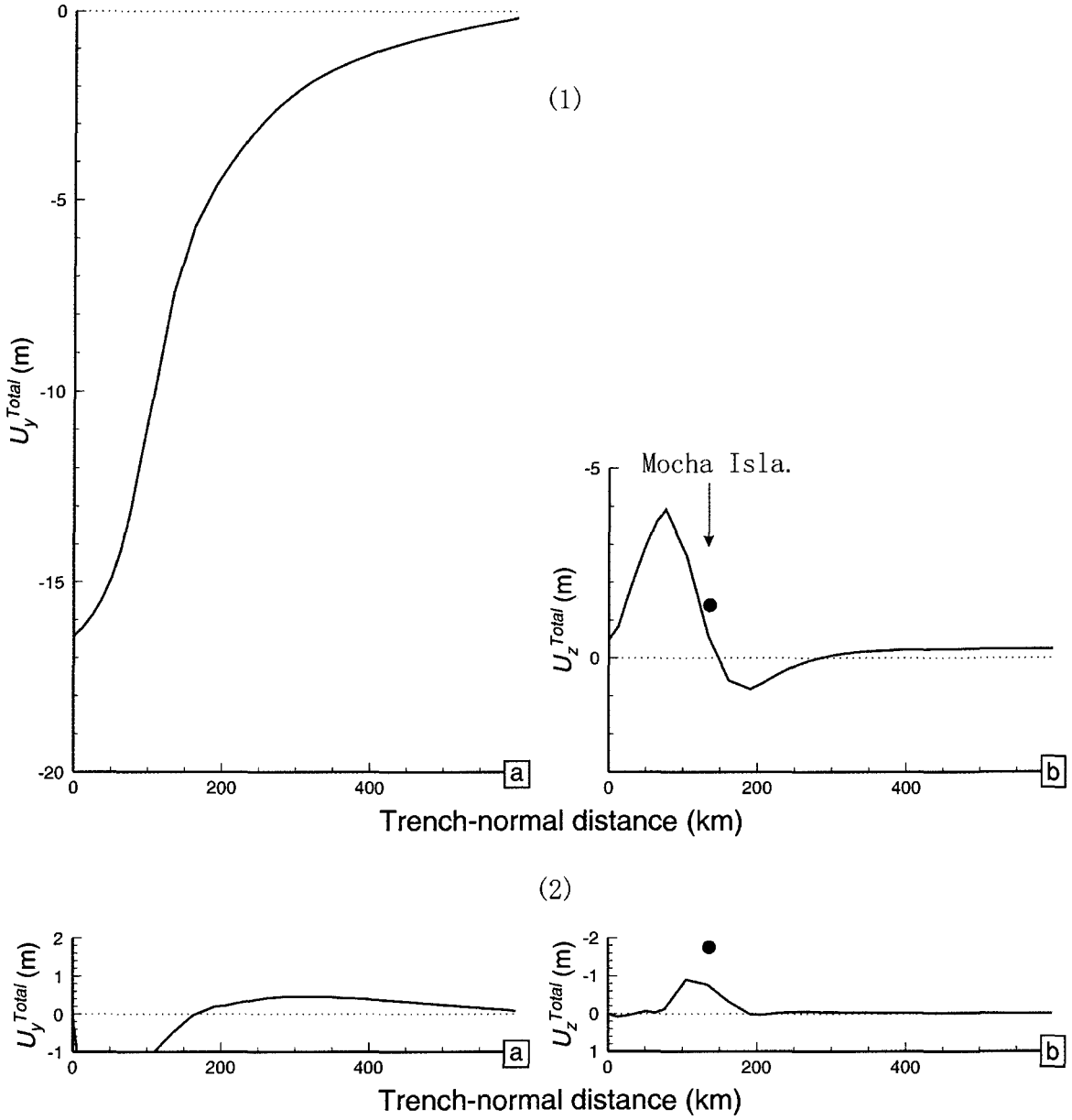

Figure 4.27. (1) Model predicted surface vertical displacements during 1960-1965. Black dot is sea level change during 1960-1965 observed by Nelson and Manley (1992). (2) Model predicted surface vertical displacements during 1965-1989. Black dot is uplift inferred from sea level change during 1965-1989 (Nelson and Manley, 1992).

such a short time interval without invoking site-specific fault slip events. Our simplified model focuses on the first-order pattern of medium response to an earthquake and is not designed to address the detailed heterogeneity at the Chile subduction zone.

Based on tide gauge records, Barrientos et al. (1992) reported postseismic uplift up to 0.75 m at Puerto Montt from 1968 to 1989. Using an elastic half-space dislocation model, Barrientos et al. (1992) proposed an afterslip of 4 m over an 84 km wide, 50 km deep and 30° dip fault to explain this postseismic uplift. The viscoelastic model predicts less than 0.1 m uplift in this area (Figure 4.28). The distances between the tide gauge sites are less than 50 km, and the subsidence among these sites from 1968 to 1989 varies from about 0.2 m to about 0.8 m (Barrientos et al., 1992). These tide gauge observations may reflect heterogeneous coupling of the subducting interface in this area.

4.6. Viscosity of the Upper Mantle

This section will study the effects of the upper mantle viscosity by varying the upper mantle viscosity of the reference model in section 4.4 by $\pm 2 \times 10^{19}$ Pa s. A schematic model has been used in section 3.3 in Chapter 3 (Figure 3.4) to illustrate the effect of upper mantle viscosity on stress relaxation of a subduction system after an earthquake. There we showed that the system response to a displacement perturbation (e.g., with known slip) is directly portrayed by the time evolution of the displacement field. If there is no subsequent loading such as backslip, the smaller the upper mantle viscosity, the more quickly the displacement reaches a new steady state. If we just consider displacement, time scales with the viscosity and hence the Maxwell time. This is true also for stress and strain. However, for time derivatives of these quantities such as velocities,

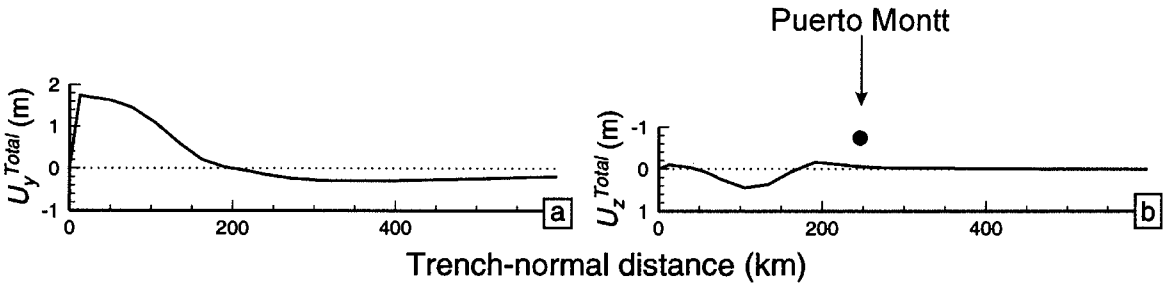

Figure 4.28. Model predicted surface vertical displacements during 1968-1989. Black dot is uplift inferred from sea level change during 1968-1989 (Barrientos et al., 1992).

the time scaling is not as simple. For example, Figures 3.5c and 3.5d indicate that the system with a smaller viscosity has a faster deformation rate (velocity) after the earthquake (e.g., from 0 to t_1, deformation with a smaller viscosity is larger). Therefore, it takes a longer, not shorter, time for the system with a smaller viscosity to decrease to a given velocity value. Because we examine velocities instead of displacements, this difference should be kept in mind.

Model results of upper mantle viscosities 1×10^{19} Pa s, 3×10^{19} Pa s, and 5×10^{19} Pa s are shown in Figure 4.29 with green, red and blue lines, respectively at time 35 years (solid) and 200 years (dotted). Surface velocities V^{EQ} in response to the earthquake with an upper mantle viscosity of 1×10^{19} Pa s are larger than those with a viscosity of 5×10^{19} Pa s. Stress relaxation in a medium of smaller viscosity is faster than that in a medium of larger viscosity (see section 3.3 in Chapter 3), and therefore has a large deformation rate (velocity).

The bottom panel of Figure 4.29a suggests that an upper mantle viscosity of 1×10^{19} Pa s may fit the present GPS velocity observations at a later model time. Although stress relaxation is faster in this model, it takes longer for the velocities in the inland area to decrease to values comparable to GPS observations. On the other hand, a viscosity of 5×10^{19} Pa s may fit the GPS observations at an earlier model time. For the model of $\eta = 1 \times 10^{19}$ Pa s, horizontal velocities 40 years after the event are found to best fit the GPS observations (Figure 4.30). For the model with the upper mantle viscosity 5×10^{19} Pa s, horizontal velocities 14 years after the event are found to best reproduce the overall pattern of the GPS observations. This agrees with the above discussion. At a given time and given the geometry, plate motion, and faulting parameters, only one upper mantle

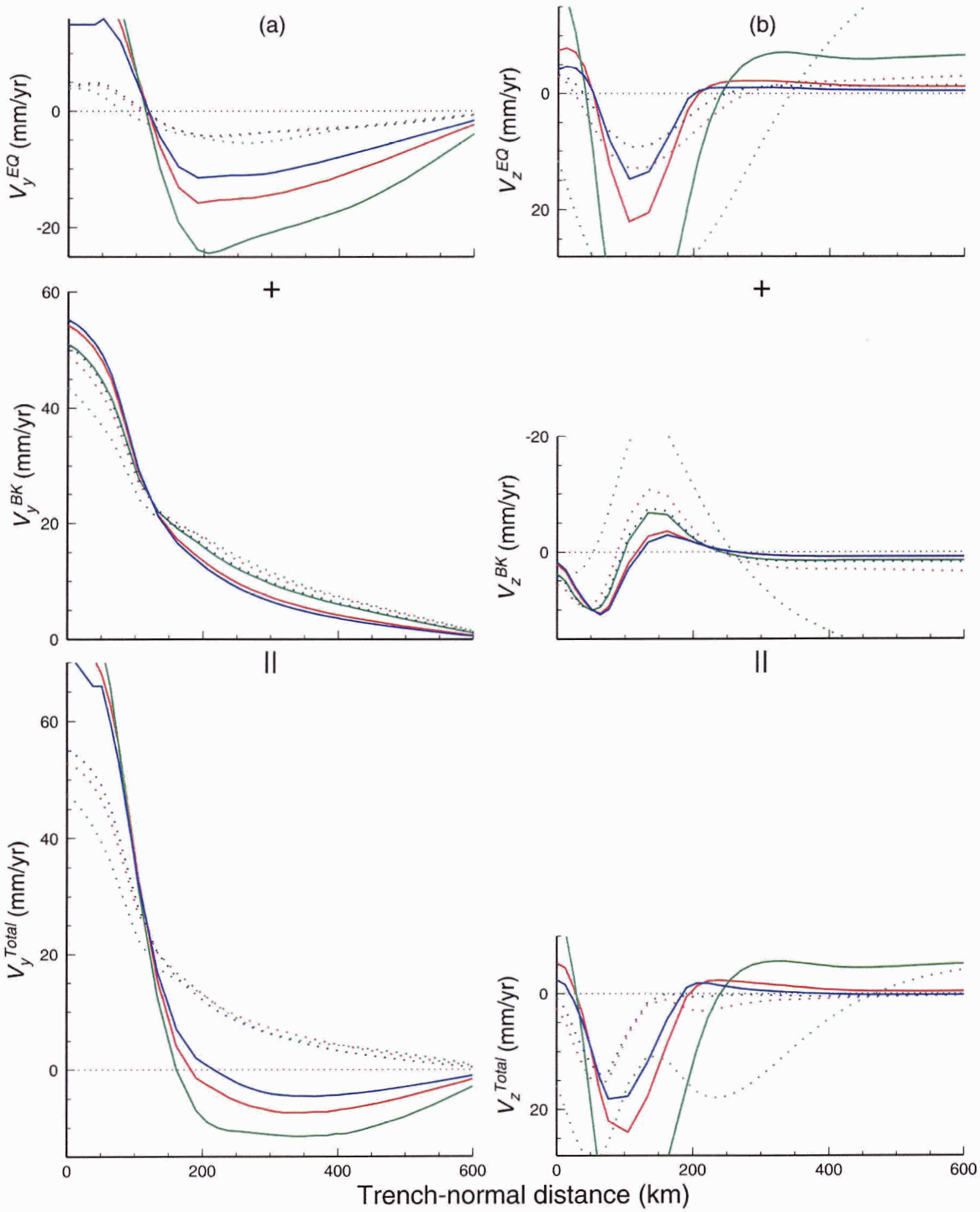

Figure 4.29. Surface velocities of models with upper mantle viscosities 1×10^{19} Pa s, 3×10^{19} Pa s, and 5×10^{19} Pa s (green, red and blue lines, respectively). Solid and dotted lines represent velocities 35 years and 200 years after the event, respectively.

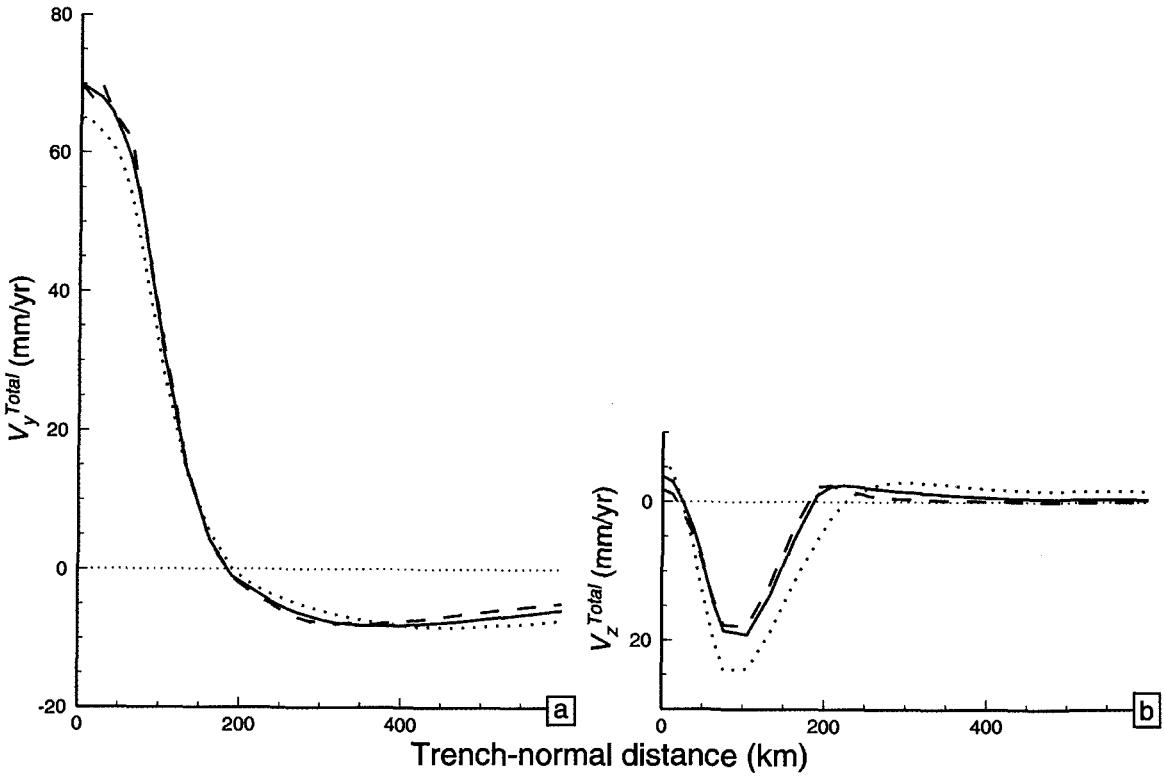

Figure 4.30. Similar velocity profiles can be produced by models with different upper mantle viscosities at different times. The solid line represents the reference model in section 4.4 with ($\eta = 3 \times 10^{19}$ Pa s) the best fits the GPS observations at 35 years after the earthquake. Dotted line represents a model with $\eta = 1 \times 10^{19}$ Pa s but 40 years after the event. Dashed line represents a model with $\eta = 5 \times 10^{19}$ Pa s but 14 years after the event.

viscosity can fit the GPS observations. In this work, the reference model with the upper mantle viscosity 3×10^{19} Pa s best reproduces the first-order pattern of the GPS observations 35 years after the event. Therefore, the model helps constrain the upper mantle viscosities at active subduction zones to be the order of 3×10^{19} Pa s for the given geometry. This viscosity value is consistent with values inferred from previously published studies of crustal deformation at active subduction zones (Table 1.1).

In this section, the elastic thickness of the continental plate and the subduction rate are varied to study the uncertainties of the upper mantle viscosity.

4.6.1. Thickness of the Continental Plate

The reference model in section 4.4 is used in this test except that the thickness of the continental plate is assumed to be 30 km instead of 40 km. Model results are shown in Figure 4.31. Decreasing the thickness by 10 km results in faster horizontal velocities in response to the earthquake alone (Vy^{EQ} in Figure 4.31), similar to using a smaller upper mantle viscosity. However, the velocities purely in response to fault locking and plate subduction do not vary much (V^{BK} in the middle panel of Figure 4.31). As explained earlier, coseismic slip induces a much larger shear stress in the upper mantle and along the downdip extension of the plate interface than that induced by fault locking. Decreasing the elastic plate thickness results in faster relaxation of this stress, and hence the effect on crustal deformation in response to the earthquake alone is more obvious.

A thinner elastic upper plate makes stress relaxation easier and faster, as if a smaller mantle viscosity were used. Velocities V^{Total} at the bottom panel of Figure 4.31 indicate that to fit the GPS observations 35 years after the event with a thinner continental plate,

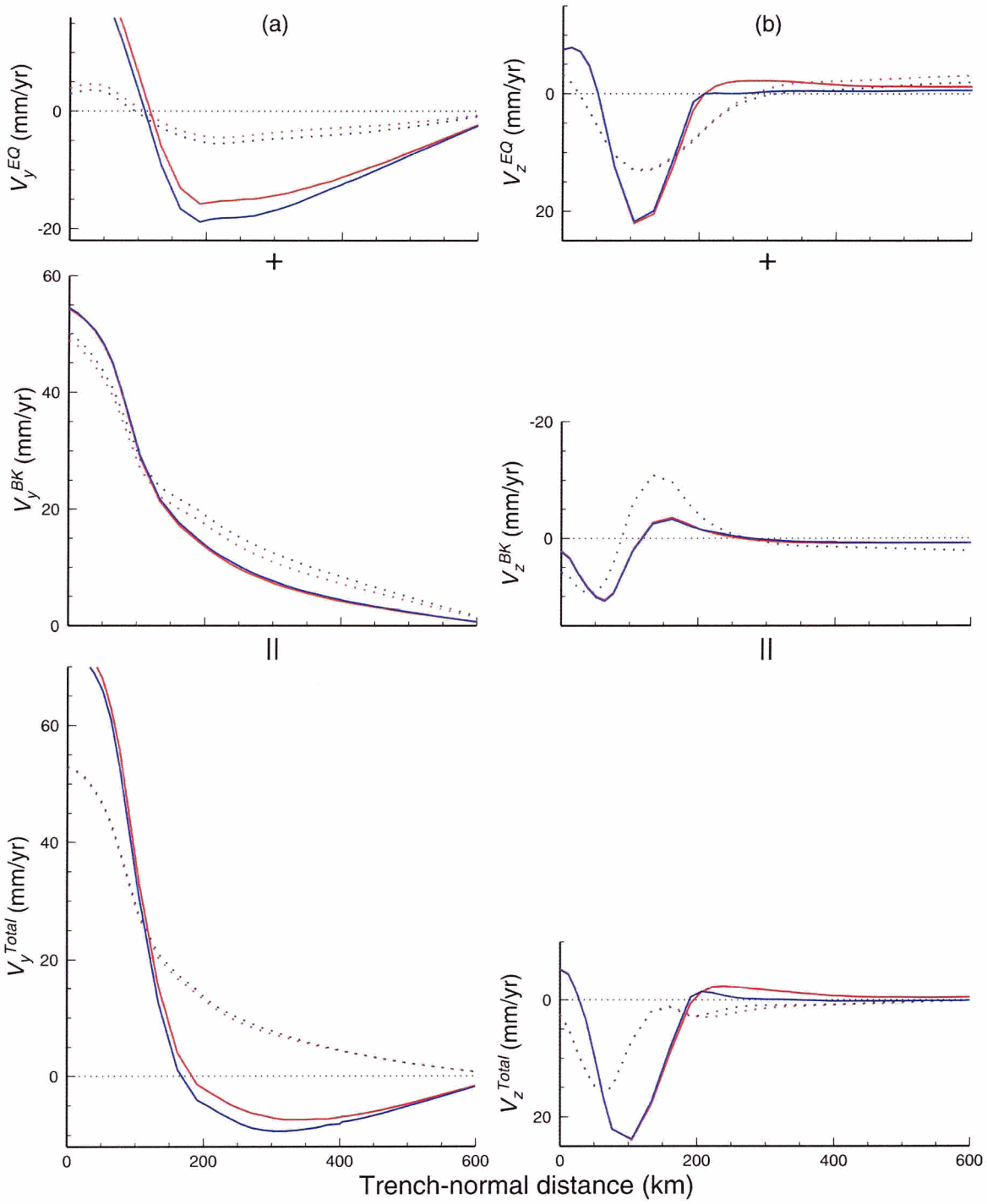

Figure 4.31. Surface velocities of models with continental plate thickness 30 km (blue) and 40 km (red). Solid and dashed lines represent velocities 35 and 200 years after the earthquake, respectively.

the upper mantle viscosity has to be larger. For a 30 km thick continental plate, an upper mantle viscosity 4×10^{19} Pa s is found to best fit the overall pattern of the seaward motion in the inland area, as shown in Figure 4.32. Surface velocities for this model are almost the same as in the model with a 40 km thick continental plate and a 3×10^{19} Pa s viscosity. This reflects the trade-off between the effect of stress relaxation and the effect of the interaction between the elastic continental plate and the viscoelastic upper mantle.

4.6.2. Subduction Rate

If the subduction rate is assumed to be 80 mm/yr according to global plate motion model NUVEL-1a (Demets et al. 1994), landward velocities due to backslip will be larger than those with a subduction rate of 66 mm/yr. The parameters of the reference model in section 4.4 except a subduction rate of 80 mm/yr are assumed in this test. This only affects the velocities in response to fault locking (V^{BK}); velocities in response to the earthquake (V^{EQ}) are the same as in the reference model (upper panel of Figure 4.33).

If the subduction rate is 80 mm/yr, horizontal velocities Vy^{BK} in response to fault locking, about 100 km from the trench, are up to ~5 mm/yr larger than these of the reference model with a subduction rate of 66 mm/yr (middle panel of Figure 4.33a).

It can be readily inferred from the bottom panel of Figure 4.33 that with a slower subduction rate, a smaller upper mantle viscosity would be required to fit the GPS observations. Figure 4.34 indicates that for the subduction rate of 80 mm/yr, model results with an upper mantle viscosity of 2×10^{19}Pa s matches the GPS observations. With a subduction rate of only 66 mm/yr, our reference model overestimates the mantle viscosity.

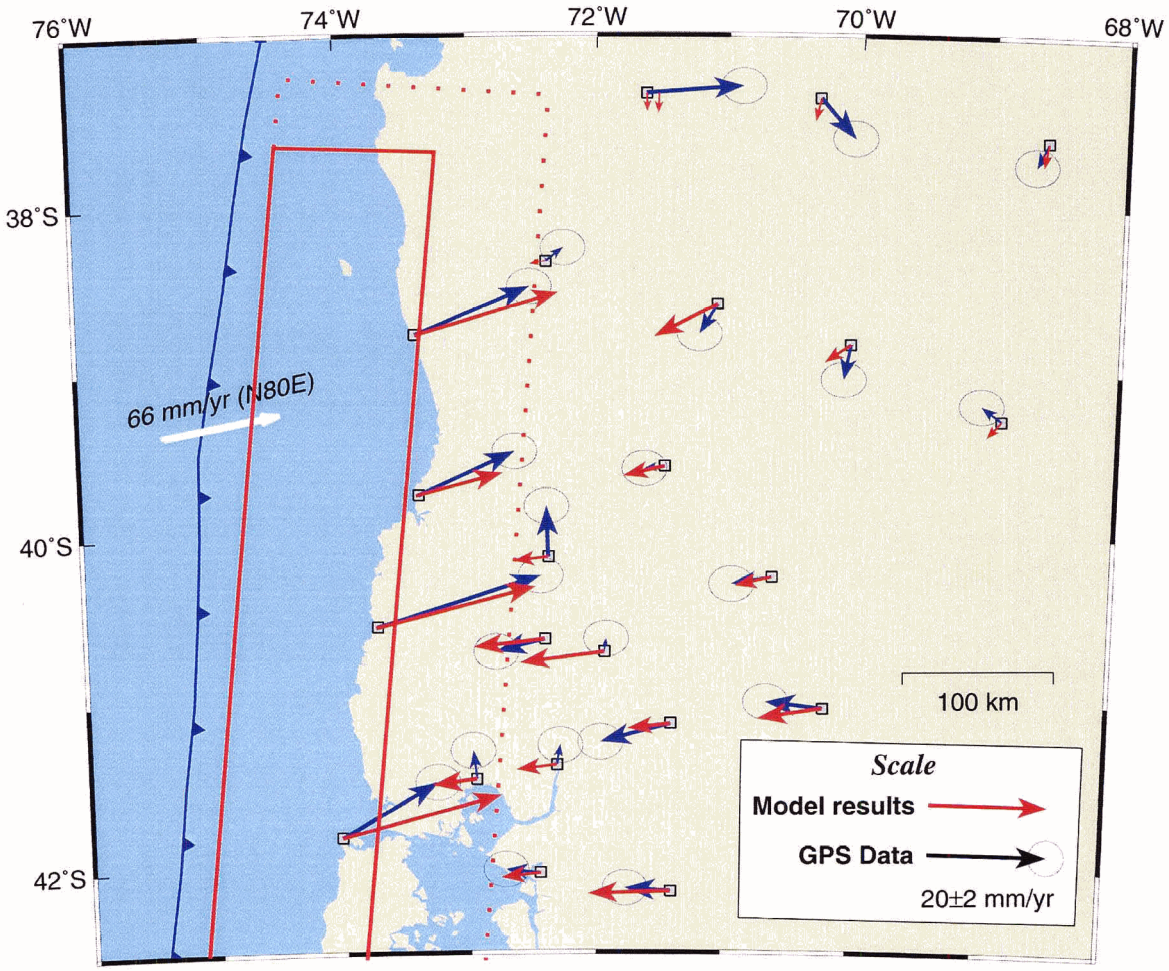

Figure 4.32. Model predicted velocities 35 years after the earthquake using a continental plate thickness 30 km and mantle viscosity 4×10^{19} Pa s compared with GPS observations. Solid and dotted red lines outline the rupture and transition zones of the 1960 Chile earthquake, respectively.

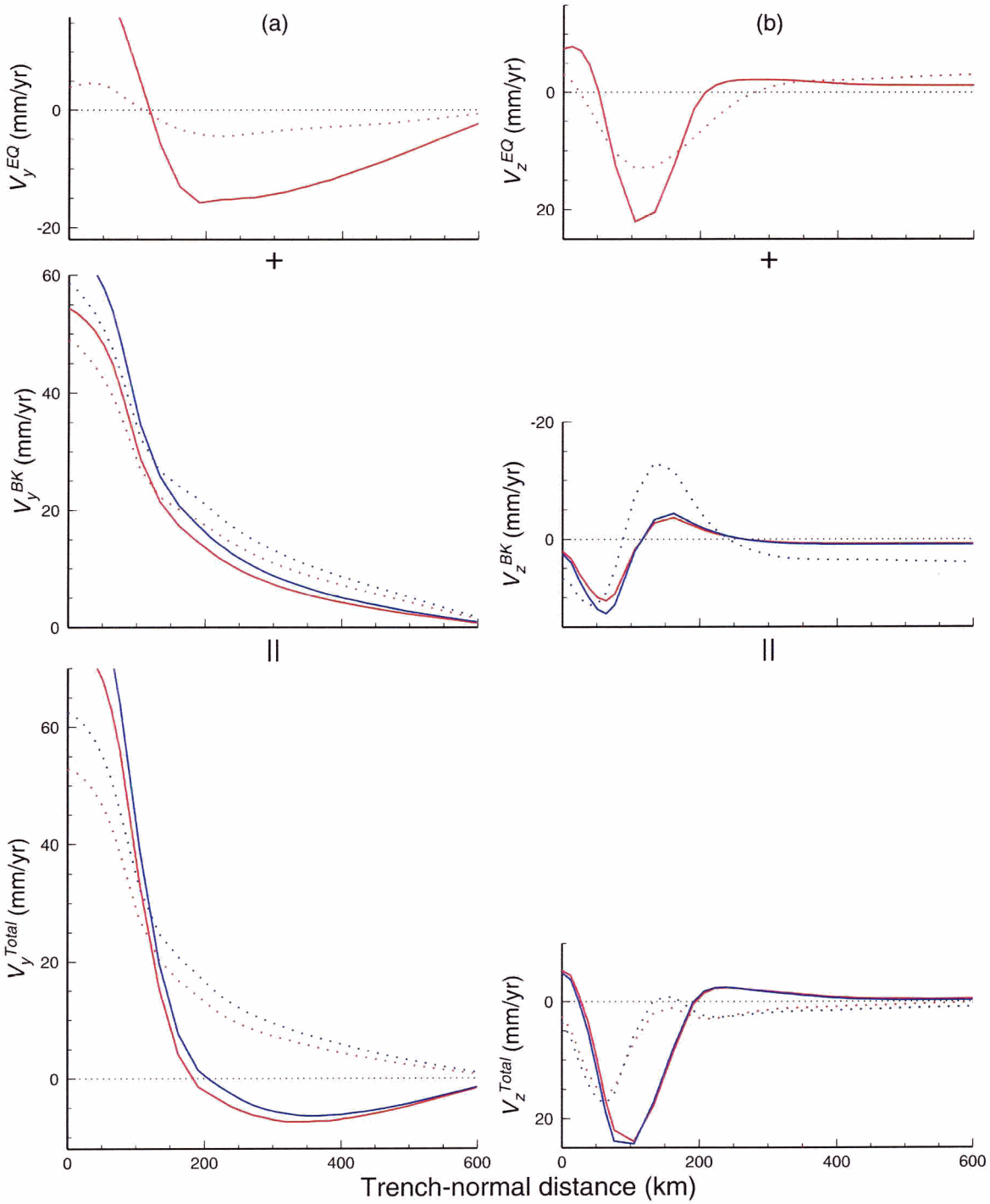

Figure 4.33. Surface velocities of models with subduction rates of 66 mm/yr (red) and 80 mm/yr (blue). Solid and dotted lines represent velocities 35 and 200 years after the earthquake, respectively. Response to the earthquake alone (top panels) is the same in both cases.

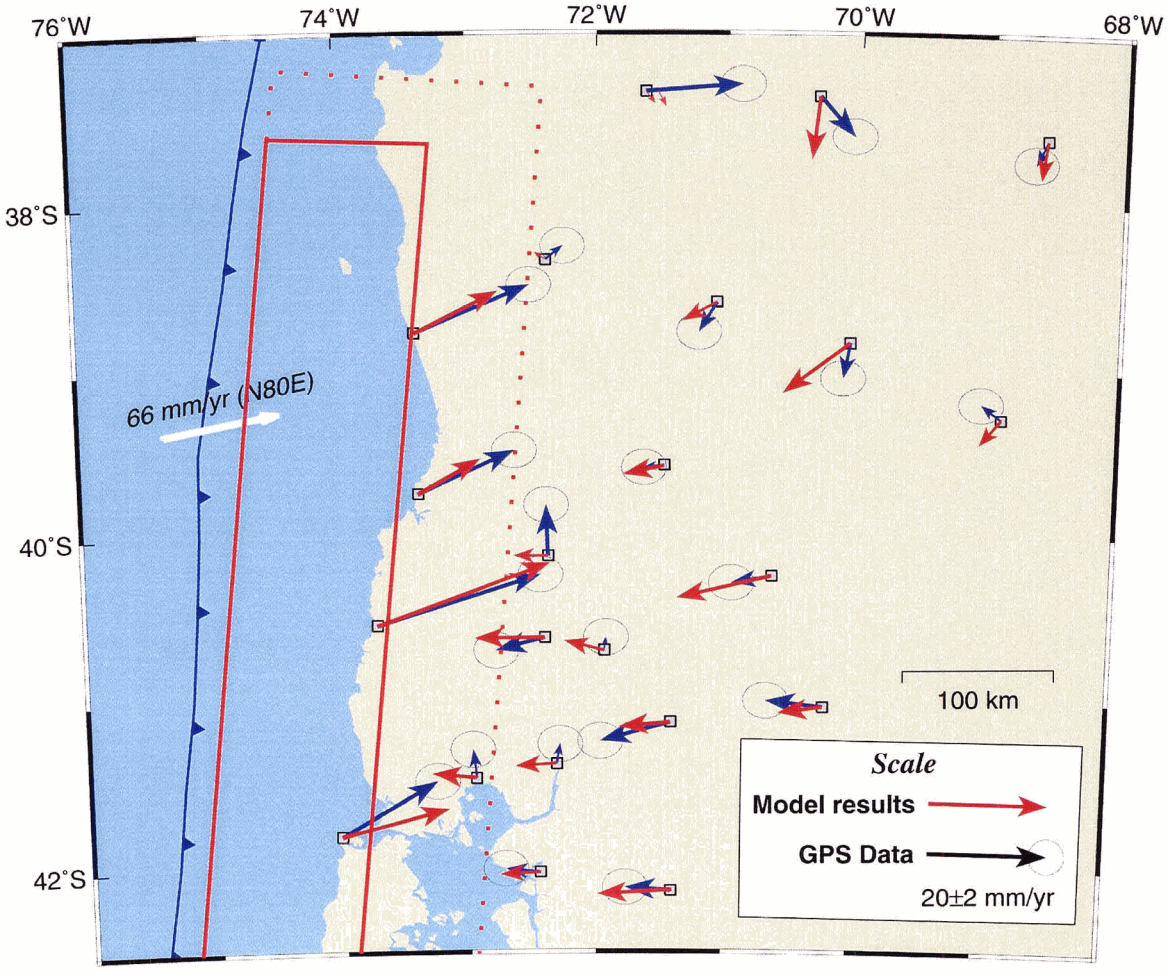

Figure 4.34. Model predicted velocities 35 years after the earthquake using a subduction rate of 80 mm/yr and mantle viscosity 2×10^{19} Pa s compared with GPS observations.

4.6.3. Distance of Trench-parallel Boundaries

If the two trench-parallel model boundaries are increased from 650 km to 1500 km from the trench, a higher upper mantle viscosity (4×10^{19} Pa s) will be needed to fit the seaward motion of GPS observations at 35 years, but the horizontal velocities in the inland areas are over predicted (results not shown).

4.7. Effects of Geometrical Parameters

The present section will discuss the sensitivity of the models to geometrical parameters (along-strike rupture length, widths of the locked and transition zones). In this chapter, I focus on model predicted velocities along the trench-normal line of symmetry of the rupture zone at the surface. In section 4.5, it has been shown that results of the reference model match the overall pattern of the GPS observations quite well. Therefore, the reference model is used as a reference for the testing cases in this section. The following models are simple variations of the reference model presented in section 4.4. All parameter values in section 4.4 are used for the tests, except the parameter to be tested.

4.7.1. Rupture Length Along Strike

If a subduction earthquake ruptures a long segment of the plate boundary (e.g., 900 km), such as in the cases of the 1960 Chile and 1964 Alaska earthquakes, response to the coseismic slip occurs in a broad area landward of the trench decades after the event. However, if an earthquake ruptures a segment with a short along-strike length (e.g., 200

km), the coseismic slip may only affect a small area near the rupture zone. The earthquake effect (represented by V^{EQ} in this work) will dissipate quickly, and the effect of fault locking will become dominant in a short time after the event. Three models with along-strike rupture lengths 200, 500 and 900 km are tested to illustrate such effect. Surface velocities of these models are shown in Figure 4.35. For the model with a 200 km rupture length, surface velocities (Vy^{EQ} 35 years after the event) in response to the earthquake alone in areas about 200 km from the trench are significantly smaller than those with a 900 km rupture length. Surface velocities V^{EQ} of the model with a 500 km rupture length are only slightly less than the 900 km case. Surface velocities V^{BK} (including Vy^{BK} and Vz^{BK}) in response to fault locking alone are identical for the three cases, except negligibly small numerical difference due to different mesh sizes.

An earthquake with an along-strike rupture length 200 km leads to a delayed response to the coseismic slip in a small area from the trench, and the delayed response disappears in a short time after the event (as shown in Figure 4.36). Earthquake with the along-strike rupture length 900 km leads to a delayed response to the coseismic slip (seaward motion) in a broad area landward of the trench decades after the event as shown in Figure 4.19. Figure 4.36 indicates that the seaward motion of inland areas about 200 km from the trench is unique for great subduction zone earthquakes that ruptured very long fault segments (e.g., > 500 km).

4.7.2. Locked Zone Width

This section will study the effects of the locked zone width. Three models with widths of locked zone 120 km and 80 km (red and blue lines in Figure 4.37, respectively)

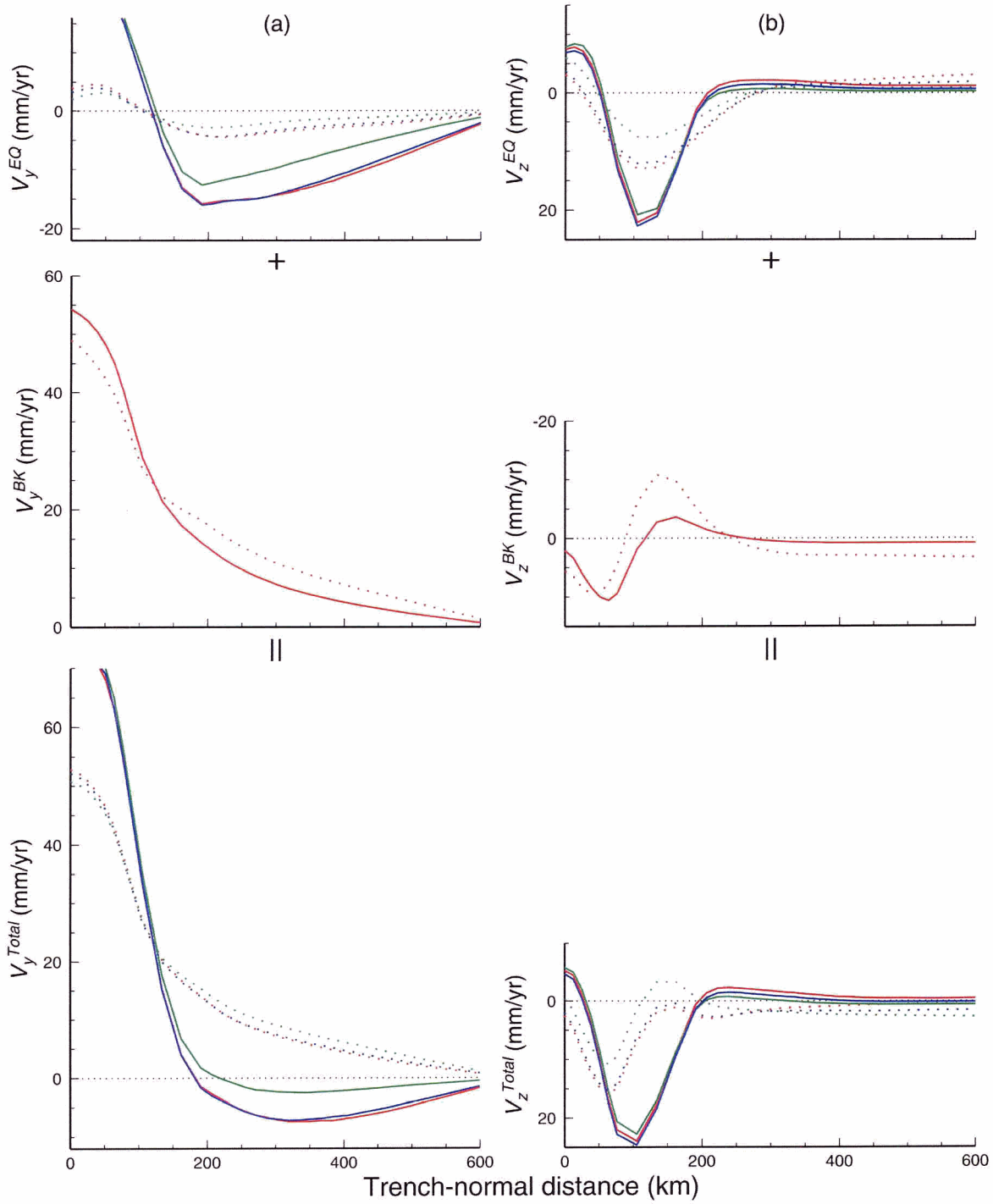

Figure 4.35. Surface velocities of models with along-strike rupture lengths 200 (green), 500 (blue), and 900 km (red). Solid and dotted lines represent velocities 35 years and 200 years after the event, respectively. Response to fault locking alone (middle panels) is the same in all three cases.

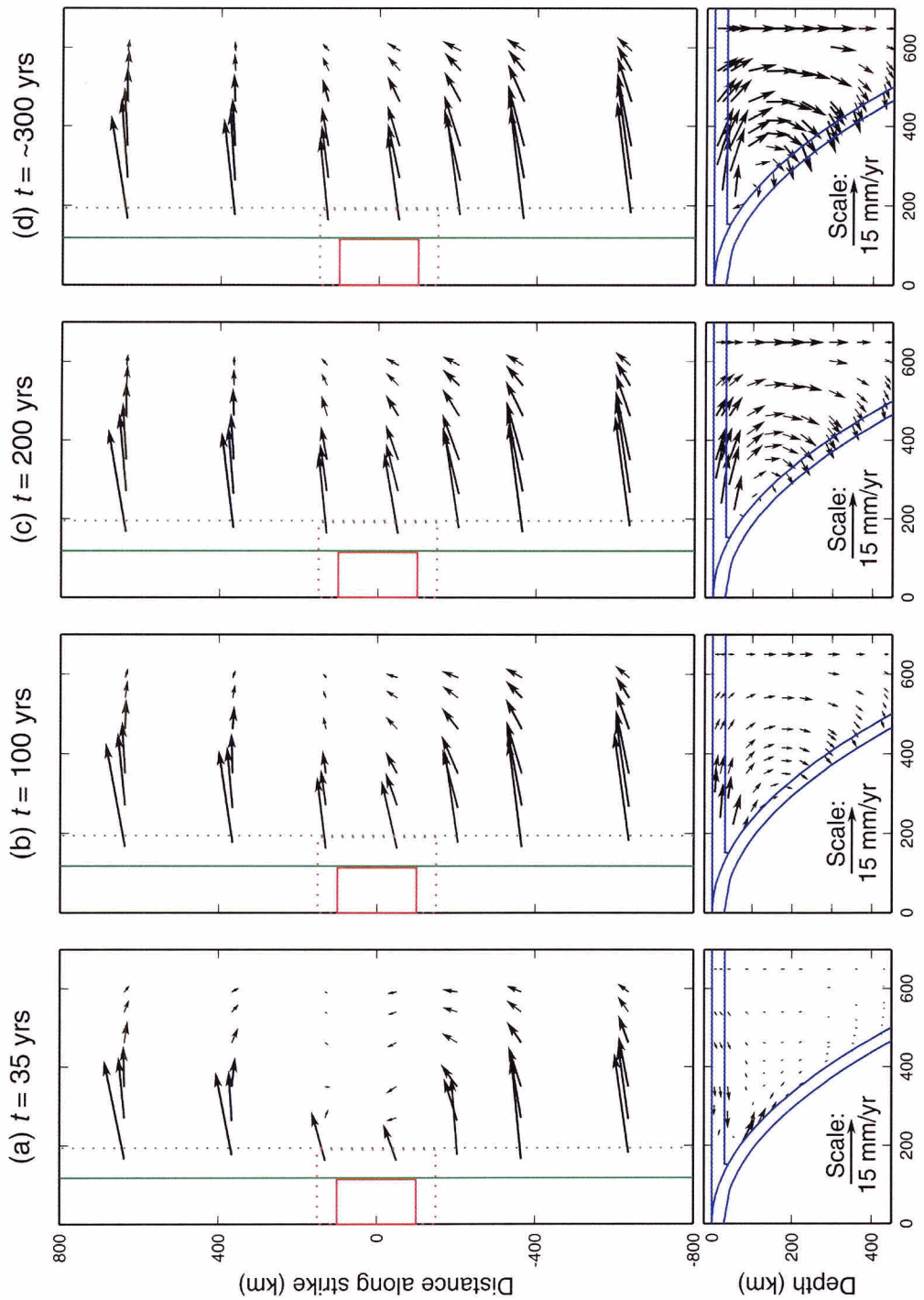

Figure 4.36. Surface velocities of the model with along-strike rupture length 200 km. Upper panel is the plan view. Lower panel is a cross-section along the trench-normal line of symmetry of the rupture zone. Solid and dotted red lines outline the rupture and transition zones, respectively.

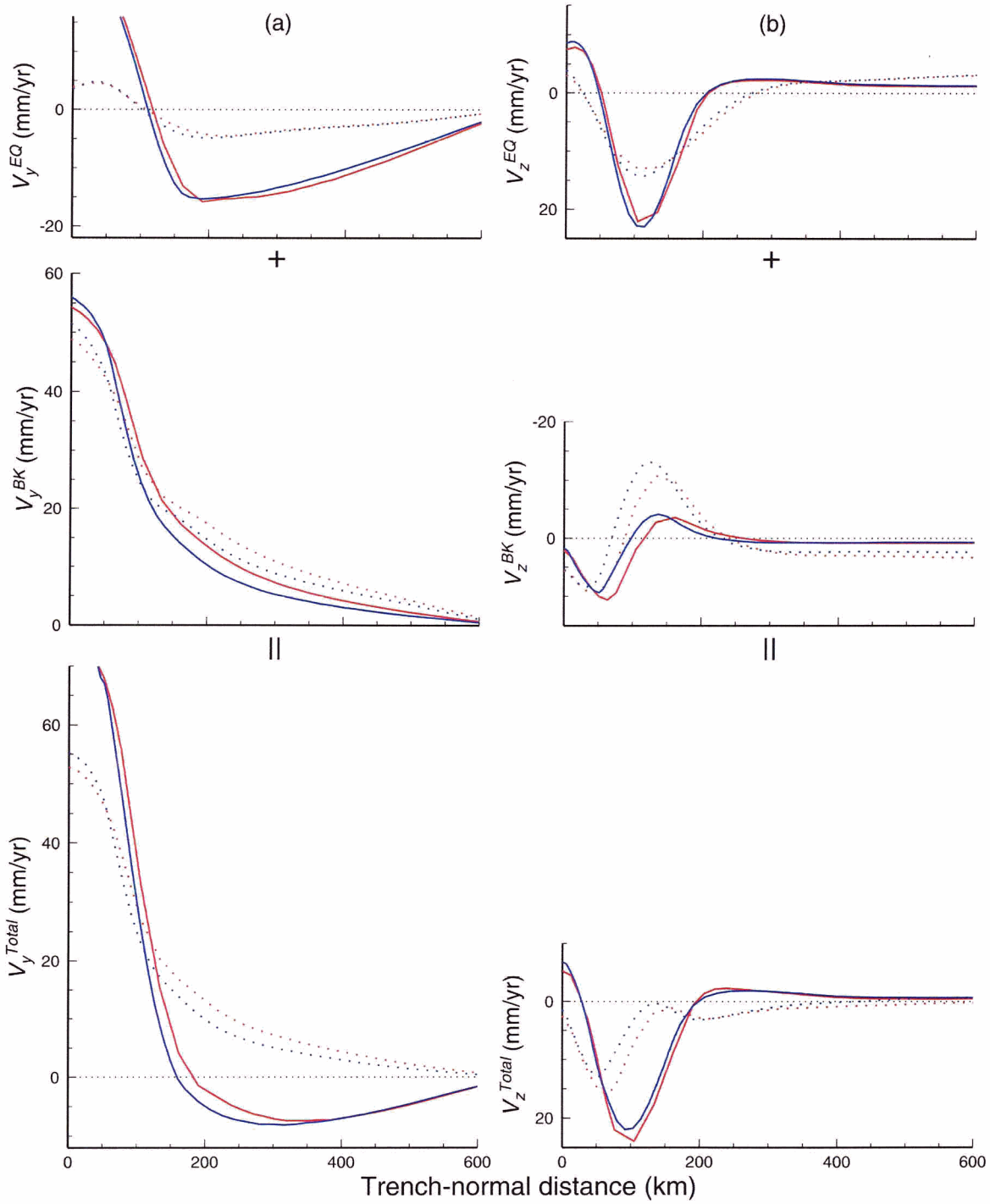

Figure 4.37. Surface velocities of models with locked zone widths 80 km (blue) and 120 km (red). Solid and dotted lines represent velocities 35 years and 200 years after the event, respectively.

are modelled. All the three models have an 80 km downdip transition zone.

For a large locked zone width, peaks of Vy (including Vy^{EQ}, Vy^{BK} and Vy^{Total}) and Vz (including Vz^{EQ}, Vz^{BK} and Vz^{Total}) are further away from the trench. Therefore, a broad locked zone leads to a broad area landward from the trench controlled by the slip distributions on the fault.

Areas about 200 km from the trench are moving seaward 35 years after the event (solid lines at the bottom panel of Figure 4.37a), but the directions in these areas reverse 200 years after the event (solid lines at the bottom panel of Figure 4.37a). In the post-seismic period (e.g., 35 yr) the effects of the earthquake (the top panel of Figure 4.37) dominate, but in the interseismic period (e.g., 200 yr) the effects of the plate subducting motion dominates (the middle panel of Figure 4.37).

4.7.3. Transition Zone Width

Models with three different transition widths of 40 km and 80 km are used to study the effects of the transition zone width as shown by green, blue and red lines in Figure 4.38, respectively. The width of the locked zone is 120 km for all the three models.

For a large locked zone width, peaks of horizontal velocities Vy and vertical velocities Vz are further away from the trench. For large transition zone widths (e.g., 80 km), Values of Vy^{EQ} and Vy^{BK} about 200 km from the trench are larger than these with short transition zone widths (e.g., 40 km). Therefore, a broad transition zone leads to a broad area landward of the trench controlled by the slip distributions on the fault. The velocity pattern of V^{Total} in response to the earthquake and fault locking 35 years after the event is similar to this of V^{EQ} in response to the earthquake, but 200 years after

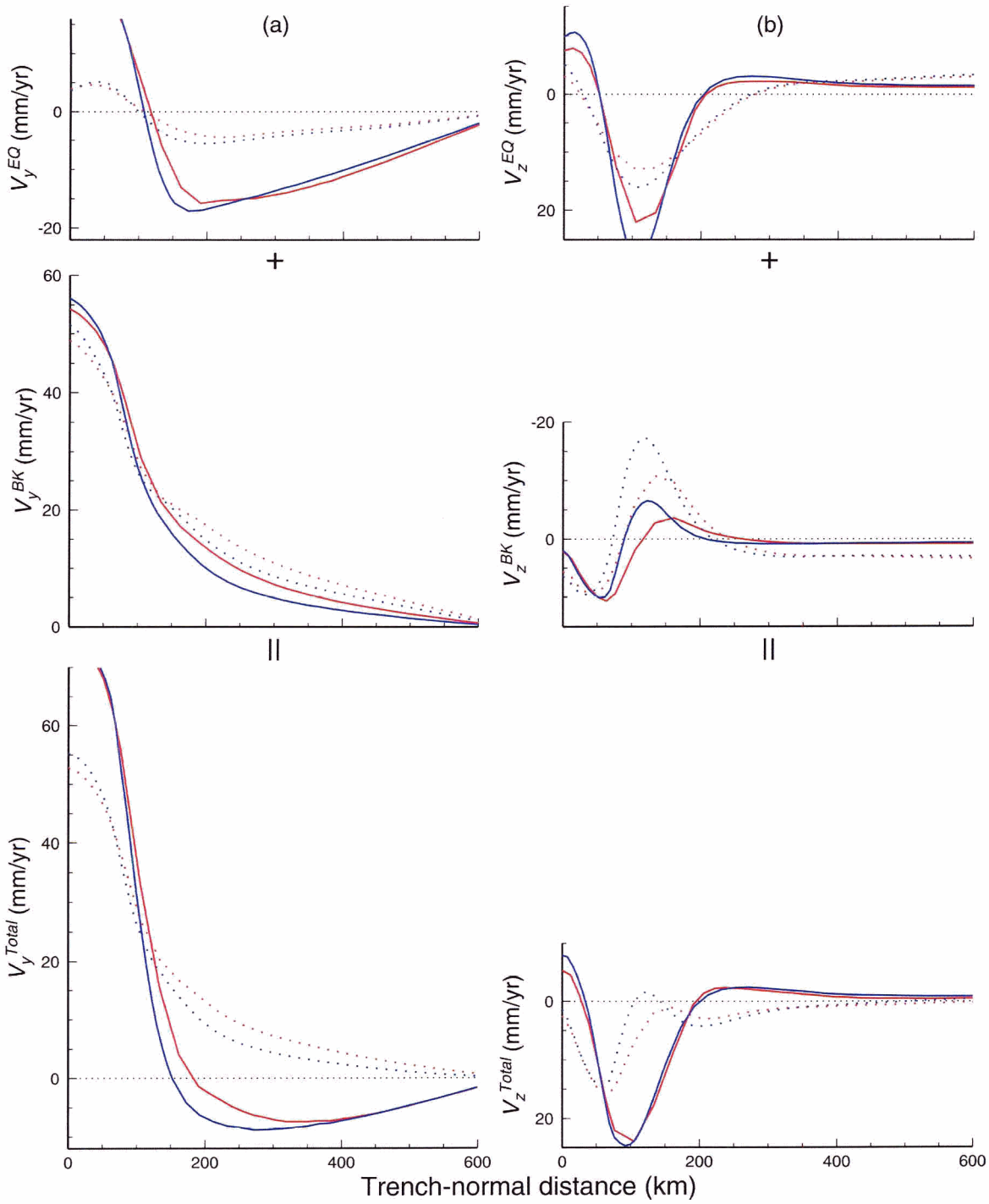

Figure 4.38. Surface velocities of models with transition zone widths of 40 km (red) and 80 km (blue). Solid and dashed lines represent velocities 35 years and 200 years after the event, respectively.

the event, similar to this of V^{BK} in response to fault locking. This indicates that in the postseismic period (e.g., 35 yr) the effects of the earthquake (the top panel of Figure 4.38) dominate, but in the interseismic period (e.g., 200 yr) the effects of fault locking dominates (the middle panel of Figure 4.38).

Chapter 5. Conclusions

In this thesis, the viscoelastic finite element method is used to study the first-order pattern of crustal deformation associated with great subduction zone earthquakes. A Newtonian Maxwell material is used to represent the upper mantle. After reviewing rock rheology and finite element formulation, the following modelling work is conducted: First, the computer program is benchmarked by comparison with analytical solutions of a 2-D viscoelastic problem and a 3-D purely elastic dislocation problem. The model results match the analytical solutions very well. Second, an idealized 2-D model is used to understand the postseismic and interseismic deformation in response to an earthquake alone, to fault locking alone, and to an earthquake followed by fault locking. Third, a 3-D model is developed for the Chile subduction zone to study postseismic deformation by comparing model results with GPS observations. Based on the simple 2-D viscoelastic tests and the 3-D application to the Chile subduction zone, the following conclusions can be drawn.

Stress in a purely elastic system never relaxes unless boundary condition changes. In a viscoelastic medium, a load leads to time dependant deformation, and stress in the medium relaxes with time. If the viscoelastic medium is uniform, the time dependence simply scales with the Maxwell time defined as the ratio of viscosity to rigidity. If the medium is not uniform, the deformation depends on the elastic and viscoelastic components of the system. The 3-D model in this thesis includes elastic plates and a viscoelastic upper mantle. An earthquake over the subduction fault results in elastic deformation. Subsequently, the shear stress induced by the earthquake relaxes in the upper mantle. The stress in the elastic plates relaxes as a result of the interaction with the

upper mantle. The stress in the elastic plates adjusts itself to be compatible with the stress in its neighbour, the upper mantle. Therefore, the stress in the elastic plates also relaxes with time.

In an earthquake cycle of a subduction zone, coseismic slip along the subduction fault results in elastic deformation in the medium. Viscoelastic deformation in the upper mantle subsequently takes place. At a given time after the earthquake, there are three contributions to the deformation of the medium. First, the stress induced by the earthquake relaxes in the upper mantle. Second, on-going plate convergence with the fault locked leads to elastic deformation at the given time. Third, the stress induced by fault locking at previous times relaxes in the upper mantle. The total deformation in the medium depends on the balance of these three contributions.

In this thesis, the effects of earthquake and fault locking are modelled separately. Medium response to the earthquake alone results in a landward surface horizontal velocity in areas above the subduction fault and a seaward velocity in areas farther away. The landward horizontal velocity in the vicinity of the fault results from a "drift" of the trench in response to earthquake-induced stresses, a likely realistic behaviour ignored in most other models. Surface vertical deformation includes subsidence above the downdip edge of the fault and uplift in other continental areas. Medium response to fault locking alone results in surface horizontal velocities in the landward direction. In contrast to deformation response to the earthquake alone, surface vertical velocity in response to fault locking alone includes uplift above the downdip edge of the fault and subsidence in other continental areas. Medium response to the earthquake followed by fault locking depends on the balance of the two separate effects. At early stages, the surface horizontal

velocity in the inland area is in the seaward direction for the area to catch up with the earthquake slip. This indicates that the effect of the earthquake dominates. At later stages, the surface horizontal velocity in this area changes to the landward direction. This indicates that the effect of the fault locking dominates.

GPS campaign data at the Chile subduction zone in 1994 – 1996 have revealed that the coastal sites are moving landward, as expected near the locked fault, but the inland sites are moving in the opposite direction. The coherent seaward motion of a contiguous set of the GPS sites only occurs landward of the rupture region of the great 1960 Mw 9.5 earthquake. This is interpreted to be a delayed response to the great 1960 earthquake. 3-D linearly Maxwell viscoelastic model is developed to study the mechanism of the seaward motion of the inland sites. A reference model with reasonable model parameters well fits the first-order patter of the seaward motion of the GPS data 35 years after the earthquake. The model predicts that the seaward motion practically disappears (< 2 mm/yr) 80 years after the earthquake. The seaward motion of inland area is unique for great long along-strike rupture length earthquakes (e.g., > 500 km).

The model also provides constraints for the upper mantle viscosity at the Chile subduction zone. Assuming elastic thickness 30 km and 40 km for the oceanic and continental plates respectively in the reference model, respectively, an upper mantle viscosity of 3×10^{19} Pa s is found to best match the first-order pattern of the GPS observations. Changing the thickness of the continental plate to 30 km results in an upper mantle viscosity of 5×10^{19} Pa s. If we assume a subduction rate of 80 mm/yr (66 mm/yr in the reference model), a smaller upper mantle viscosity is required to fit the GPS observations. If we assume the trench-normal boundaries to be 1500 km landward and

seaward from the trench (650 km in the reference model), an upper mantle viscosity of 4 $\times 10^{19}$ Pa s is found to best fit the data, but velocities in distant inland areas are over predicted. This indicates that the upper mantle viscosity in the Chile subduction zone is of the order of 3×10^{19} Pa s. This is consistent with findings in other subduction margins (Table 1.1) and in contrast with values ($10^{20} - 10^{21}$ Pa s) assumed in global post glacial rebound models that are more relevant to regions of continental interiors.

Bibliography

Angermann, D., J. Klotz, and C. Reigber, Space-geodetic estimation of the Nazca-South America Euler vector, *Earth and Planetary Science Letters, 171*, 329-334, 1999.

Atwater, B.F., M. Cisternas, I. Salgado, G. Machuca, M. Lagos, A. Eipert, and M. Shishikura, Incubation of Chile's 1960 earthquake, AGU 2003 fall meeting, 2003.

Barrientos, S.E., G. Plafker, and E. Lorca, Postsesimic coastal uplift in Southern Chile, *Geophysical Research Letters, 19*, 701-704, 1992.

Barrientos, S.E., and S.N. Ward, The 1960 Chile earthquake; inversion for slip distribution from surface deformation, *Geophysical Journal International, 103*, 589-598, 1990.

Bevis, M., E.C. Kendrick, R. Smalley, T. Herring, J. Godoy, and F. Galban, Crustal motion north and south of the Arica deflection; comparing recent geodetic results from the Central Andes, *Geochemistry, Geophysics, and Geosystems, 1*, 1-12, 1999.

Blanpied, M.L., D.A. Lockner, and J.D. Byerlee, Fault stability inferred from granite sliding experiments at hydrothermal conditions, *Geophysical Research Letters, 18*, 609-612, 1991.

Burov, E.B., and M. Diament, The effective elastic thickness (Te) of continental lithosphere: what does it really mean? *Journal of Geophysical Research, 100*, 3,905-3,927, 1995.

Byrne, D.E., D.M. Davis, and L.R. Sykes, Loci and maximum size of thrust earthquakes and the mechanics of shallow region of subduction zones, *Tectonics, 7*, 833-857, 1988.

Chen, W. and P. Molnar, Focal depths of intracontinental and intraplate earthquakes and their implications for the thermal and mechanical properties of the lithosphere, *Journal of Geophysical Research, 88*, 4,183-4,214, 1983.

Cifuentes, I.L., The 1960 Chilean Earthquakes, *Journal of Geophysical Research, 94*, 665-680, 1989.

Cifuentes, I.L., and P.G. Silver, Low-frequency source characteristics of the great 1960 Chilean earthquake, *Journal of Geophysical Research, 94*, 643-663, 1989.

Cohen, S.C., Postseismic deformation due to subcrustal viscoelastic relaxation following dip-slip earthquakes, *Journal of Geophysical Research, 89*, 4,538-4,544, 1984.

Davis, S., and J. Karzuloíc, Landslides at Lago Riñihue, *Bulletin of the Seismological Society of America, 53*, 1,403-1,414, 1963.

Delouis, B., H. Philip, L. Dorbath, and A. Cisternas, Recent crustal deformation in the Antofagasta region (northern Chile) and the subduction process, *Geophysical Journal International, 132*, 302-338, 1998.

Demets, C., R.G. Gordon, D.F. Argus, and S. Stein, Current plate motions, *Geophysical Journal International, 101*, 425-478, 1990.

Demets, C., R.G. Gordon, D.F. Argus, and S. Stein, Effect of recent revisions to the geomagnetic reversal time scale on estimates of current plate motions, *Geophysical Research Letters, 21*, 2,191-2,194, 1994.

Dewey, J.F., and S.H. Lamb, Active tectonics of the Andes, *Tectonophysics, 205*, 79-95, 1992.

Dieterich, J.H., Time-dependent friction and the mechanics of stick-slip, *Pure and Applied Geophysics, 116*, 790-806, 1978.

Dieterich, J.H., A constitutive law for rate of earthquake production and its application to earthquake clustering, *Journal of Geophysical Research, 99*, 2,601-2,618, 1994.

Doser, D., A.M. Veilleux, and M. Velasquez, Seismicity of the Prince William Sound region for over thirty years following the 1964 great Alaskan earthquake, *Pure and Applied Geophysics, 154*, 593-632, 1999.

Dragert, H., K. Wang, and T.S. James, A silent slip event on the deeper Cascadia subduction interface, *Science, 292*, 1,525-1,528, 2001.

Duda, S.J., Strain release in the circum-Pacific belt, Chile: 1960, *Journal of Geophysical Research, 68*, 5,531-5,544, 1963.

Duke, M., and D. Leeds, Response of soils, foundations, and earth structures to the Chilean earthquakes of 1960, *Bulletin of the Seismological Society of America*, 53, 309-357, 1963.

Freymueller, J.T., S.C. Cohen, and H.J. Fletcher, Spatial variations in present-day deformation, Kenai Peninsula, Alaska, and their implications, *Journal of Geophysical Research, 105*, 8,079-8,101, 2000.

Heki, K., S. Miyazaki, and H. Tsuji, Silent fault slip following an interpolate thrust earthquake at the Japan Trench, *Nature, 386*, 595-598, 1997.

Heki, K., and Y. Tamura, Short tem afterslip in the 1994 Sanriku-Haruka-Oki earthquake, *Geophysical Research Letters, 24*, 3,285-3,288, 1997.

Hofmann-Wellenhof, B., H. Lichtenegger, and J. Collins, Global Positioning System : theory and practice, fourth edition, *edited by* B. Hofmann-Wellenhof, H. Lichtenegger, and J. Collins, Springer-Verlag, Vienna New York, 1997.

Housner, G.W., An engineering report on the Chilean earthquakes of May, 1960, *Bulletin of the Seismological Society of America, 53*, 219-223, 1963.

Hughes, T.J.R., Generalisation of selective integration procedures to anisotropic and nonlinear media, *International Journal for Numerical methods in Engineering, 15*, 1,413-1,418, 1980.

Hughes, T.J.R., The finite element method - linear static and dynamic finite element analysis, *Prentice-Hall International Inc.*, Englewood Cliffs, New Jersey, 1987.

Hyndman, R.D., M. Yamano, and D.A. Oleskevich, The seismogenic zone of subduction thrust faults, *Island Arc, 6*, 244-260, 1997.

Hyndman, R.D. and K. Wang, Thermal constraints on the zone of major thrust earthquake failure, The Cascadia subduction zone, *Journal of Geophysical Research, 98*, 2,039-2,060, 1993.

Hyndman, R.D. and K. Wang, Current deformation and thermal constraints on the zone of potential great earthquakes on the Cascadia subduction thrust, *Journal of Geophysical Research, 100*, 22,133-22,154, 1995.

James, T.S., J.J. Clague, K. Wang, and I. Hutchinson, Postglacial rebound at the northern Cascadia subduction zone, *Quaternary Science Reviews, 19*, 1,527-1,541, 2000.

Jordan, T.E., J.H. Reynolds, and J.P. Erikson, Variability in age of initial shortening and uplift in the Central Andes, *in* Tectonic Uplift and Climate Change, *edited by* W. F. Ruddiman, *Plenum Press*, New York, pp. 41-61, 1997.

Kanamori, H., The energy release in great earthquake, *Journal of Geophysical Research, 82*, 2,981-2,987, 1977.

Kanamori, Hiroo, and J.J. Cipar, Focal process of the great Chilean earthquake May 22, 1960, *Physics of the Earth and Planetary Interiors, 9*, 128-136, 1974.

Kelleher, J.A., Rupture zones of large South American earthquakes and some predictions, *Journal of Geophysical Research, 77*, 2,087-2,103, 1972.

Kendrick, E. C., M. Bevis, R.J. Smalley, O. Cifuentes, and F. Galban, Current rates of convergence across the Central Andes; estimates from continuous GPS observations, *Geophysical Research Letters, 26*, 541-544, 1999.

Khazaradze, G., K. Wang, J. Klotz, Y. Hu, and J. He, Prolonged post-seismic deformation of the 1960 great Chile earthquake and implications for mantle rheology, *Geophysical Research Letters*, *29*, 7-1-7-4, 2002.

Klotz, J., D. Angermann, G.W. Michel, R. Porth, C. Reigber, J. Reinking, J. Viramonte, R. Perdomo, V.H. Rios, S. Barrientos, R. Barriga, and O. Cifuentes, GPS-derived deformation of the Central Andes including the 1995 Antofagasta M_w = 8.0 earthquake, *Pure and Applied Geophysics*, *154*, 3,709-3,730, 1999.

Klotz, J., G. Khazaradze, D. Angermann, C. Reigber, R. Perdomo, and O. Cifudentes, Earthquake cycle dominates contemporary crustal deformation in Central and Southern Andes, *Earth and Planetary Science Letters*, *193*, 437-446, 2001.

Liang, G.P., Finite element program generator and finite element language, *in* Reliability and robustness of engineering software II, *Edited by* C.A. Brebbia et al., Computational Mechanics Publications, London, 1991.

Linde, A.T., and P.G. Silver, Elevation changes and the great 1960 Chilean earthquake: Support for aseismic slip, *Geophysical Research Letters*, *16*, 1,305-1,308, 1989.

Lomnitz, C., Major earthquakes and tsunamis in Chile during the period 1535 to 1955, *Geologische Rundschau*, *59*, 938-960, 1970.

Lowry, A.R., K.M. Larson, V. Kostoglodov, and R. Bilham, Transient fault slip in Guerrero, southern Mexico, *Geophysical Research Letters*, *28*, 3,753-3,756, 2001.

Matsu'ura, M., and T. Iwasaki, Study on coseismic and post-seismic crustal movements associated with the 1923 Kanto earthquake, *Tectonophysics*, *97*, 201-215, 1983.

Melosh, H.J., Rheology of the earth: theory and observation, *in* Physics of the earth's interior, Proceedings of the 1979 Enrico Fermi summer school, Varenna, Italy, *Edited by* A. M. Dziewonski and E. Boschi, *Noord-Hooland*, Amsterdam, pp. 318-336, 1980.

Melosh, H.J., and A. Raefsky, A simple and efficient method for introducing faults into finite element computations, *Bulletin of the Seismological Society of America*, *71*, 1,391-1,400, 1981.

Miyashita, K., A model of plate convergence in southwest Japan, inferred from levelling data associated with the 1946 Nankaido earthquake, *Journal of Physics of the Earth*, 35, 449-467, 1987.

Nelson, A.R., and W.F. Manley, Holocene coseismic and aseismic uplift of Isla Mocha, South-central Chile, *Quarternary International*, *15/16*, 61-76, 1992.

Nishenko, S.P., Seismic potential for large and great interpolate earthquakes along the Chilean and Southern Peruvian margins of South America, *Journal of Geophysical Research, 90*, 3,589-3,615, 1985.

Norabuena, E., L. Leffler-Griffin, A. Mao, T. Dixon, S. Stain, S.I. Sacks, L. Ocola, and M. Ellis, Space geodetic observations of Nazca-South America convergence across the central Andes, *Science, 279*, 358-362, 1998.

Okada, Y., Surface deformation due to shear and tensile faults in a half-space, *Bulletin of the Seismological Society of America, 75*, 1,135-1,154, 1985.

Okada, Y., Internal deformation due to shear and tensile faults in a half-space, *Bulletin of the Seismological Society of America, 82*, 1,018-1,040, 1992.

Ozawa, S., M. Murakami, and T. Tada, Time-dependent inversion study of the slow thrust event in the Nankai Trough subduction zone, southwestern Japan, *Journal of Geophysical Research, 106*, 787-802, 2001.

Peltier, W.R., The impulse response of a Maxwell Earth, *Reviews of Geophysics and Space Physics, 12*, 649-668, 1974.

Piersanti, A., Postseismic deformation in Chile: Constraints on the asthenospheric viscosity, *Geophysical Research Letters, 26*, 3,157-3,160, 1999.

Plafker, G., Alaskan Earthquake of 1964 and Chilean Earthquake of 1960; implications for Arc Tectonics, *Journal of Geophysical Research, 77*, 901-925, 1972.

Plafker, G., and J.C. Savage, Mechanism of the Chilean earthquakers of May 21 and 22, 1960, *The Geological Society of America Bulletin, 81*, 1,001-1,030, 1970.

Pollitz, F.F., R. Burgmann, and P. Segall, Joint estimation of afterslip rate and postseismic relaxation following the 1989 Loma Prieta earthquake, *Journal of Geophysical Research, 103*, 26,975-26,992, 1998.

Pollitz, F.F., and I.S. Sacks, Modeling of postseismic relaxation following the great 1857 earthquake, southern California, *Bulletin of the Seismological Society of America, 82*, 454-480, 1992.

Ranalli, G., *Rheology of the Earth*, second edition, *Chapman & Hall*, London, 1995.

Rogers, G., and H. Dragert, Episodic tremor and slip on the Cascadia subduction zone: The chatter of silent slip, *Science, 300*, 1,942-1,943, 2003.

Ruina, A., Slip instability and state variable friction law, *Journal of Geophysical Research, 88*, 10,359-10,370, 1983.

Rydelek, P.A., and I.S. Sacks, Asthenospheric viscosity and stress diffusion: a mechanism to explain correlated earthquakes and surface deformation in NE Japan, *Geophysical Journal International, 100*, 39-58, 1990.

Saffer, D.M., K.M. Frye, C. Marone, and K. Mair, Laboratory results indicating complex and potentially unstable friction behavior of smectite clay, *Geophysical Research Letters, 28*, 2,297-2,300, 2001.

Satake, K., K. Wang, and B.F. Atwater, Fault slip and seismic moment of the 1700 Cascadia earthquake inferred from Japanese tsunami descriptions, *Journal of Geophysical Research, 108*, 2,535, 2003.

Savage, J. C., A dislocation model of strain accumulation and release at a subduction zone, *Journal of Geophysical Research, 88*, 4,984-4,996, 1983.

Savage, J.C., J.L. Svarc, and W.H. Prescott, Deformation across the Alaska-Aleutian subduction zone near Kodiak, *Geophysical Research Letters, 26*, 2,117-2,120, 1999.

Shimamoto, T., T. Seno, and S. Uyeda, A simple rheological framework for comparative subductology, *in* Relating Geophysical Structures and Processes: The Jeffreys Volume, Geophysical Monograph, *76, edited by* K. Aki and R Dmowska, pp. 39-52, AGU, Washington, D.C., 1993.

Sievers, H.A., G. Villegas, and G. Barros, The seismic sea wave of 22 May 1960 along the Chilean coast, *Bulletin of the Seismological Society of America, 53*, 1,125-1,190, 1963.

Suito, H., and K. Hirahara, Simulation of postseismic deformations caused by the 1896 Riku-u earthquake, northeast Japan: re-evaluation of the viscosity of the upper mantle, *Geophysical Research Letters, 26*, 2,561-2,564, 1999.

Tarling, D.H., The crust of the Earth, *in* The Cambridge encyclopedia of earth science, *Edit by* D.G. Smith, *Prentice-Hall Canada Inc., and Cambridge University Press*, pp.166, 172, 1981.

Thatcher, W., T. Matsuda, and J.B. Rundle, Lithospheric loading by the 1896 Riku-u earthquake, northern Japan: implications for plate flexure and asthenospheric rheology, *Journal of Geophysical Research, 85*, 6,429-6,435, 1980.

Thatcher, W., and J.B. Rundle, A viscoelastic coupling model for the cyclic deformation due to periodically repeated earthquakes at subduction zones, *Journal of Geophysical Research, 89*, 7,631-7,640, 1984.

Tichelaar, B.W., and L.J. Ruff, Depth of seismic coupling along subduction zones, Journal of Geophysical Research, 98, 2,017-2,037, 1993.

Tse, S. T. and J. R. Rice, Crustal earthquake instability in relation to the depth variation of friction slip properties, *Journal of Geophysical Research, 91*, 9,452-9,472, 1986.

Ueda, H., M. Ohtake, and H. Sato, Postseismic crustal deformation following the 1993 Hokkaido Naseioki earthquake, northern Japan: Evdience for a low-viscosity zone in the uppermost mantle, *Journal of Geophysical Research, 108*, 2,151, 2003.

Wahr, J., and M. Wyss, Interpretation of postseismic deformation with a viscoelastic relaxation model, *Journal of Geophysical Research, 85*, 6,471-6,477, 1980.

Walcott, R.I., Flexural Rigidity, Thickness, and Viscosity of the Lithosphere, *Journal of Geophysical Research, 75*, 3,941-3,954, 1970.

Wang, K., H. Dragert, and H.J. Melosh, Finite element study of uplift and strain across Vancouver Island, *Canadian Journal of Earth Sciences, 31*, 1,510-1,522, 1994.

Wang, K., J. He, H. Dragert, and T.S. James, Three-dimensional visco-elastic interseismic deformation model for the Cascadia subduction zone, *Earth Planet Space, 53*, 295-306, 2001.

Wu, P., Deformation of an incompressible viscoelastic flat earth with power law creep: a finite element approach, *Geophysical Journal International, 108*, 35-51, 1992.

Yin, Y., *Finite element method and its application to geoscience, Seismology Publishing House*, China, pp.24-31, 1987, in Chinese.

Zheng, G., R. Dmowska, and J.R. Rice, Modeling earthquake cycles in the Shumagin subduction segment, Alaska, with seismic and geodetic constraints, *Journal of Geophysical Research, 101*, 8,383-8,392, 1996.

Zweck, C., J.T. Freymueller, and S.C. Cohen, Three-dimentional elastic dislocation modeling of the postseismic response to the 1964 Alaska earthquake, *Journal of Geophysical Research, 107*, 1-11, 2002.

Zweck, C., J.T. Freymueller, and S.C. Cohen, The 1964 Great Alaska Earthquake; Present day and cumulative postseismic deformation in the western Kenai Peninsula, *Physics of the Earth and Planetary Interiors, 132*, 5-20, 2002.